4. Discussion

The results presented in the previous chapter of this thesis are now detailed to offer a broad view of the main proposals drawn from the findings encountered during the study of the postulated materials. The nature of the research done herein is to explore the modification of material properties by means of intended changes in their chemical composition, in the search for novel solutions in the field of PV technologies, i.e., new absorber materials for cheaper and/or more efficient solar cells. This search is performed either in already used families of materials with proved potential for that task or other systems where promising characteristics or properties have been detected but a profound study has not been carried out yet. The degree of knowledge already gained about the corresponding material lead the efforts here to varied analyses targeting different gaps of knowledge in the literature about them. Through different kinds of compositional engineering, exploring different solutions with varied dopants and concentrations of the different elements that make up the material, new solutions with improved PV features are offered. While the general case presented here is trying to elucidate how efficient a solar device based on the studied material as absorber would be, looking at its bandgap and absorption mainly, also the stability of the materials under study has been thoroughly addressed, with special attention in the case of perovskites, being one of their main challenges towards commercialization.

Following the order in which the publications are presented in the previous chapter, firstly, the proposal of two new absorber materials which are considered to own optimal properties for being used in a IBSC configuration is argued. On one side, the indium phosphide, with a long background of use in photovoltaics as III-V semiconductor with a wide bandgap adequate for use in tandem configurations.[68] On the other hand, a novel material in the field like the tin and germanium nitride with spinel structure, which due to its wide bandgap and good electron mobility shows great potential for this application.[69] Both materials, after doped with the proper transition metal, Cr and Co respectively, show the desirable in-gap states to allow a two-photon excitation process of electrons to boost the efficiency of the solar power conversion process beyond the SQL.

Next, the promoted contributions to the state of the art of perovskite solar cells are discussed, with special focus on their stability issues, like in the third publication of the compendium,[220] and the replacement of lead as a highly toxic element.[220,221] On the base of halide perovskites as the record efficiency holders, a combination of halogens, as well as different inorganic monovalent cations,[221] have been explored to face the instability problems. The optimal concentration of these elements, all together with the substitution rate of Pb with Sn, dealing with the toxicity problem, has been investigated looking at the impact of these substitutions on the different properties of the perovskites.

In the last publication, ML techniques are used to study again spinel nitrides, although this time without doping. The variation of the relative stability and bandgap of these materials upon the concentration and specific arrangement of their cations is inspected in depth, trying to take the greatest advantage as possible of the great tunability of these spinels and maximize their capability of sunlight absorption.[189] This last work is used as a proof of concept of the implementation of ML to drastically reduce the computational cost of a vast study with several thousand systems to explore and, at the same time, expands the potential of spinel nitrides use as solar cell absorbers, previously justified in the second publication here discussed, offering interesting alternatives of host materials for the IBSCs or within a multilayer device as TSCs.

For the sake of intelligibility and simplicity, the series of articles published by the author will be respectively referred as art., followed by the number in which they have been ordered in this compendium.

4.1. Analysis of the results

4.1.1. Intermediate band materials

In this first block of results two new intermediate band materials are proposed, after the calculations performed showed very adequate electronic configurations when doping with the appropriate transition metal. The realization of an IBSC from these materials would lead to devices with a theoretical maximum efficiency close to 60% from a single absorber layer, improving the existing records for such devices by more than a 20%, under maximum solar concentration conditions.

When trying to prove the possibility of formation of an intermediate band in a host material through the transition metal doping process,[53,89,91,154,267] the effect of doping with different transition metals on the electronic configuration of the host is assessed, comparing the modified absorption features of the doped material with those of the undoped host. For that purpose, the host material is characterized in a thorough search process looking for the more accurate computational methods (from DFT functionals to beyond DFT approximations) to describe the structure of the system, its electronic configuration and based on it its absorption spectra. Once the most suitable methods have been selected a similar characterization is carried out for several systems including doping with different transition metals and in some cases at different concentration rates. In this step it is important to converge the acting forces in the crystal lattice, to rigorously evaluate the structural distortion caused by the atom substitution, usually with a different size than the original and therefore need to be adapted within the lattice structure of the crystal. Apart from the structural fit of the dopant atoms, the energetics of the substitution process is also examined by looking at the formation enthalpies of the doped compounds. The electronic configuration is calculated with precision to obtain an equally precise absorption spectrum which can be used to estimate the efficiency of the material, or at least a maximum efficiency limit. Due to the impossibility of directly quantify the non-radiative

recombination process on the resulting materials with the tools and resources available here, as one of the main problems of IBSC operation, the existence of the main factor for its appearance, the strongly localized charge density around impurity traps,[268] is also surveyed by means of a partial charge density analysis, checking out the spatial spreading of the electronic states corresponding with the introduced intermediated band.

In art.º 1,[68] a traditionally used semiconductor in the photovoltaics industry like indium phosphide[269–271] is studied as a possible host material to conform the absorber layer of an IBSC after doping it with the appropriate transition metal. InP is one of the materials with the highest efficiency limit together with GaAs,[272] although the lower cost of the latter, despite the high toxicity of As,[273] along with the modest gains in comparison with silicon solar cells have significantly detained its growth. Fact that could be reverted with the boost of efficiency gained in a IBSC configuration. Despite the small bandgap of InP (1.35 eV) not being optimal for an IBSC, all the already acquired expertise regarding this material and the manufacturing of solar cells based on it would be of great advantage in the process towards a rapid commercialization. Additionally, if the introduction of the desired in-gap states could be achieved efficiencies close to 60% could still be reached, not far from the maximum 63% PCE for bandgaps of 2 eV.[50,62] To this end, a series of four early 3-d block transition metals have been inserted in the InP lattice at concentration rates close to 3% (1/32) of cationic sites occupation. Ti, V, Cr and Mn have been so used for the doping and identically studied, except for the partial charge density analysis, just performed for the Cr-doping case, the only case showing signs of the proper electronic configuration to form an intermediate band.

In art.º 2,[69] in contrast to the previous one, a completely new material for the field is explored. Binary nitride compounds with cations from the group IV of the periodic table (the carbon group, as it is known in semiconductor physics), with Si_3N_4 as the most prominent material, are ceramics of quite common use in the industry due to their mechanical properties and great stability, with a remarkable resistance to surface oxidation and to thermal variations.[274–276] The insulator nature of these materials, with extremely wide bandgaps, impede its use for optoelectronic applications like solar cells. Nevertheless, their respective spinel phases present reduced bandgaps in comparison and can be synthetized through high pressure methods despite not being the most favorable ones.[277] In particular, the spinel γ-phase of Sn and Germanium compounds, with bandgaps of 1.6 and 3.5 eV respectively,[278] present also great electron mobilities. This fact opens up the possibility of fine-tuning the bandgaps through the combination of both cations at different concentration rates, for a wide total range between the ones corresponding to the pure compounds, very propitious for IBSCs. The sum of all the commented properties, together with the fact that all the elements that made up these materials present abundant resources in the earth's crust,[16] gives a huge potential to these compounds to be used as solar absorbers. Aiming at an IBSC configuration, a more systematic exploration of transition metals for the doping has been performed in this work, covering all the elements of the 3d block (from Sc to Zn) and two of the most abundant elements of the 4d block, Nb and Mo. Two different concentration rates, around 4 and 8 % (1/24 and 2/24) over the total cationic sites, have been considered as well for all the dopants. In this case three different

dopants (Cr, Co and Cu) yield promising results with electronic configurations showing adequate in-gap states.

Regarding the computational methodology followed, in the case of InP, the PBEsol functional was used for structural relaxation of the unit cells. To precisely describe the electronic configuration of the material the PBE+U method was selected, because of its moderate computational cost and the easiness to obtain the dielectric constant from which the absorption spectrum was derived with this method. Accurate bandgaps, contrasted with experimental results as well as G_0W_0 calculations used as supporting reference, were obtained by fitting a U value of 15 eV for the d-electrons of In. The need for additional U values for the d electrons of the tested dopants was discarded after qualitatively comparing the resulting electronic configurations of the doped materials with those obtained with the GW method, with enough background of use to describe doped systems like this one.[53,90,267] In the case of spinel nitrides, on the contrary, the PBE functional was used to optimize the structures, while the GW_0 approach was used to obtain accurate electronic configurations. Interestingly, with the comparison between these two systems, different cases related to the previously commented bandgap overestimations usually committed with the different flavors of the GW approximation are perfectly exemplified. While in the case of InP precise bandgap results are obtained with the G_0W_0 scheme, leading to notably overestimated values within the self-consistent scheme, for the spinels the GW_0 approach is needed to reach accurate values of bandgap. In both cases, the decision on which methodology to use is made upon the comparison with experimental results for the undoped compounds after testing several methods, looking also at their computational cost as secondary reason for selection in case of comparable results.

Moving to the results, the structural effects of the doping has been assessed for the two systems. In both, the lattice parameters of the unit cells are hardly affected by the introduction of the dopant atom/s, with trifling variations below 0.01 Å in the case of InP (Table 1 in art.º 1) and of 0.11 Å at maximum, below 1% variation, in the case of spinels (Figure 2 in art.º 2). The bonding distance for the different cations is also studied, seeing really small distortions for the different dopants and in comparison with the substituted element, again maximum changes observed for spinels with a maximum deviation below 4% (same sources as for lattice constants). To evaluate these figures properly it must be taken into account that the concentration rate of dopant is slightly higher for the spinels case, being also the radius of the dopant atoms more diverse because of the number of options considered in the latter case. For both systems, it can be concluded that the still small concentration of dopant does not seem to affect much the integrity and regularity of the crystal lattices, fact that is reinforced by the maintained values of bandgap in all the cases where the introduced states corresponding to the doping atoms do not overlap those shaping the original bandgap.

With respect to the formation enthalpies of the doped compounds, negative values refer to a priori thermodynamically stable compounds, at least considering the substitutional process studied for the doping. From Figure 3 in art.º 1, it is observed that the process of doping InP with Cr is clearly energetically favored, with the lowest formation enthalpy among the studied dopants with -0.345 eV per atom in the unit cell. For the case of spinels, given $Sn_{1.5}Ge_{1.5}N_4$ is not a well-stablished compound like InP, the formation of the host compound has

also been assessed thermodynamically. For that purpose its enthalpy of formation has been calculated, also considering its main competitor phase, the phenacite.[279] The enthalpies shown in Figure 3 from artº 2 point towards phenacite as the most stable phase, at least at the 0 K conditions for which the DFT calculations can be made. Despite this result, the energetic barrier that locates the spinel phase in the metastability region is below 35 meV per atom, being the formation energy versus its precursor elements significantly negative. Given nitride compounds are the class of chemical compounds with a larger fraction of synthesizable compounds with positive formation enthalpies,[123] with cases above 150 meV per atom,[280,281] and considering as reference that γ-Sn_3N_4 has already been synthesized[278] with notably higher formation enthalpies than our host compound with mixture of cations, the positive enthalpies obtained should be viewed as a likely surmountable difficulty in the synthesis process. The doping compounds give also moderately positive values for the three commented cases where convenient in-gap states are found, below 35 meV per atom for the cases of Cr and Co and close to 50 meV for the case of Cu, again with positive values of formation energy compared to its forming elements.

Looking at the band diagrams of the doped compounds presented in Figures 5 of art.º 1 and 7 of art.º 2 respectively, different types of in-gap states introduced by dopant atoms can be identified. There are some cases where the in-gap states overlap with those comprising the VB or the CB, leading only to a reduction of the bandgap with no effective in-gap states. This is the case of Ti-doped InP or the spinel nitride doped with Sc, Ti, Mn, Ni or Nb (see Figures S3, S4, S7, S10 and S13 of the supplementary material of art.º 2). Within this casuistry could be included the Mn-doped InP compound depending on which results are considered. As seen in Figure 5 of art.º 1, PBE+U results show two well-separated bands at -0.8 (superior limit of CB) and 0 eV (theoretical IB), however in the G_0W_0 results (see Figure S3 in the supplementary material of art.º 1) these bands appear completely overlapped. In some other cases, even though the introduced states are well-differentiated from the VB and CB, they do not meet the requirement of being partially filled to allow both electronic transition from the VB and to the CB. This situation occurs for the case of V-doped InP and V, Fe and Zn-doped $Sn_{1.5}Ge_{1.5}N_4$ (Figures S5, S8 and S12 of art.º 2 supplementary material). Finally, for the cases of Cr-doped InP and Cr, Co and Cu doped nitride spinel, in-gap states are observed crossing the Fermi energy level (located at 0 eV) and so indicating partial filling. Therefore, they meet all the requirements to be considered as forming an IB. The distance between the different bands will determine the likeliness of the different excitonic transitions and therefore the real improvement in the absorption features of the material, with the Co-doped spinel outstanding because of the widely separated IB.

As previously mentioned, an analysis of the partial density of the IB states is performed for the selected compounds, i.e., those cases where the IB appears. This is done to check if the states comprising that IB are discrete levels, which would be detrimental because of the increase of the non-radiative recombination,[268] or instead they present some interaction with the surrounding atoms forming a non-localized defect state. In all the cases but the Cr-doped spinel nitride it is observed that the electronic density corresponding to the IB states spatially spreads towards the neighbor atoms, meaning that their wavefunctions are highly delocalized and so they could perform as IB. On the contrary for the Cr-doped spinel compound it can be seen how

the density is completely localized around the dopant atom and so is much more likely for an excited electron in it to recombine faster.

To compute the absorption spectra of these four chosen compounds (plus the three other doped compounds in art.º 1 for which the absorption spectra was calculated too) a different procedure has been followed in each work, although in both cases obtained from the frequency-dependent dielectric function. In the case of the InP compounds the dielectric function was calculated as a sum over empty states (imaginary part) and through the Kramers-Kronig transformation (real part).[282] Additionally, making use of the calculation from individual transitions one by one, the absorption spectra has been decomposed upon the type of transition contributing to the whole spectra, distinguishing between VB-IB, IB-CB, VB-CB and inner transitions within the IB. For the work with the spinel nitrides, the Bethe-Saltpeter equation (BSE) was used instead,[101,283] starting from the ground-state obtained with the GW approximation. This methodology has the advantage of including the excitonic effects for a more accurate description, however its computational cost is much larger than the previous method, for the calculation itself and for the previous steps, requiring of a method such as GW as starting point. Despite the lower accuracy of the first method, for the purpose of comparison between the doped and the undoped compounds is perfectly suitable. Looking at Figures 8 and 9 of art.º 1 and 2 respectively it is clearly observable that in all the cited cases the absorption spectra increase compared to that of the undoped host material, specially at lower energy values because of the IB related transitions. While in the case of InP the increase of absorption across the range of energies studies was clear, for the doped spinels two of the doped compounds show lower absorption close to the original peak at 2.1 eV. For that reason it was decided to quantify the area under the curve of the spectra and compare it with that of the host compound, resulting in increases of roughly a 33% for the cases of Cr and Cu, and of a bit more than 200% for the case of Co, as shown in Figure 10 of art.º 2. Finally, the gap between bands has been used to estimate a maximum photovoltaic efficiency of the different compounds according to the detailed-balance methodology,[284] shown also in Figure 10 of art.º 2.

4.1.2. Perovskites

The focus and goals at the time of studying PSCs has been notably different from the approach used for IBSCs. Perovskites have been widely researched for the last decade, probably being the hottest topic in photovoltaics for that long. Therefore, many aspects of these materials have been studied in detail and a simple DFT analysis presenting bandgaps and absorption spectra wouldn't bring much new knowledge to the field. One thing in common between all the research works dealing with perovskites for PV (as some other applications have emerged in the recent years)[285–288] is that they forcefully point out that the biggest challenge towards major commercialization of PSCs is their poor long-term stability compared to other solar cells in the market, like those based in silicon, CdTe or CIGS.[22,23,289] Additionally, the Lead toxicity is another major problem still to be addressed without hindering the PV performance.[29] With that in mind, the focus here has been to provide new insights into the stability and toxicity issues of these materials and try to offer solutions to them through compositional engineering. The scope has

been fixed on inorganic perovskites, according to the research line presented on previous studies here gathered completely focused on inorganic materials. Inorganic perovskites have been already proposed as a promising solution for the stability problems related to these materials, because of their stronger bonding between the monovalent cation and the anions that considerably reduce the rotation of the first ones, being one of the main causes of their stability problems.[290–293] Among inorganic perovskites, $CsPbI_3$ is the one that up to now has exhibited the best efficiency record, although it has not reached yet the efficiencies of the best-in-class MAPI. However, $CsPbI_3$ does not solve the toxicity problem, and it also brings new issues related with the size of the Cs for the crystal lattice void.[294,295] To deal with this issues the partial replacement of Cs and Pb by Rb and Sn has also been proposed as a possible solution,[296–298] although optimal concentration rates for each are not clear. Here, these substitutions, along with different halogen mixes mainly to adjust bandgaps have been studied performing a full screening of concentration rates.

In art.º3,[220] the introduction of Sn replacing Pb, for the reduction of toxicity, and of Br replacing I, pursuing the idea of making smaller the BX_6 octahedra (referred to the ABX_3 standard formula) for a better fitting with the Cs atom contained in it, is explored to see its effects on some stability-related properties of the material. A couple of structural tolerance factors, the main lattice parameters, some mechanical properties and the thermodynamic of the formation process (considering the formation from fundamental elements as well as from main precursors or competitor phases) have been evaluated. Similar trends upon concentration changes have been observed for some of these properties, which are compared aiming to stablish certain correlations that allow to predict the stability of these materials, taking as reference value the formation enthalpy of these compounds as a measurement of their intrinsic stability.

To study the chosen set of perovskites, the PBEsol functional has been used for the structural relaxation, while it was decided to use the SCAN functional for the thermodynamical analysis, with great accuracy in total energy results for solids. No further method was needed in this case as the electronic configuration of the compounds was not studied in this work. To define the series of compounds examined their general formula is defined through two concentration rates, *b* and *x*, describing the concentration of Pb/Sn in the divalent cationic positions and I/Br in the anionic sites as $CsPb_{1-b}Sn_b(I_{1-x}Br_x)_3$.

Looking at the main lattice parameters of the researched compounds, presented in Figure 2 of the corresponding work, the cell volume of the different compounds varies linearly upon concentration changes, in a more pronounced way for halogen concentration changes than for the divalent cations. This linear trend is not observed for the case of the lattice parameter and the shape ratio, which essentially measures how distorted is the original cubic shape characteristic of perovskites by deviations from the unity. The divalent cation concentration variations have a mild effect on the lattice parameter, which slightly decrease in line with the atom size of the two elements (Pb and Sn), while it does not affect at all the shape ratio of the compounds. It is the modification of the I and Br relative concentration what mostly affects the lattice constant of the compound cell, although in a not linear way. In compounds where there is a clear preponderance of either I or Br slight changes are observed in the lattice constant, however upon certain limit value of highly mixed concentrations, defining a range

approximately between *x*=0.33-0.66, a quick decrease of the lattice parameter occurs according to the smaller size of Br atoms. The shape factor is defined by the *x* concentration in a not linear way as well, leading to a shortened/enlarged structure for the intervals x=0-0.33 and 0.66-1 where Br and I atoms occupy opposed sites in a fixed direction of the octahedra respectively, while for the range between those two the trend is reverted, reaching again a completely cubic structure almost at *x*=0.6.

Apart from the basic parameters related to the lattice constant, some others also related to structural aspects and the chemical composition have been calculated. The Goldschmidt's tolerance factor, a commonly used indicator of the stability of perovskites, a modified version of it and the bonding strength have been used for the purpose of acquaint not only the basic distortions of the cell but the more local ones, involving few atoms and the bonds between them. Thus, these parameters focus on the equilibrium derived from the use of different elements and the possibility of bond breaking provoked by the commented local distortions. In that sense, the Goldschmidt and the Sun's parameter (its modified version) consider the optimal difference of size between the elements that made up the perovskite not to add to much stress to the structure, while the bonding strength basically measures how easily would the different bonds break upon that stress generated. From Figures 3 and 4 from art.º3, where the value of these parameters for the different compounds tested is presented, it can be seen that the maximum values (values closer to but below unity for the Goldschmidt's parameter), considered optimal, are reached for the pure $CsSnBr_3$ compound in the case of the Goldschmidt's factor and the bonding strength parameter, showing a linear increase upon the rise of *b* and *x* concentration rates, although more pronounced for *b* variations in the case of the Goldschmidt's factor and for *x* changes in the case of the bonding strength. Looking at the Sun's parameter the optimal compound would be $CsPbBr_3$, but not much better than $CsSnBr_3$ as this parameter is mostly influenced by the *x* concentration rate. A slight reduction of values of the Sun's parameter for compounds with concentration rates near *x*=0.5 is observed, leading to a kind of plateau in the ascending trend defined by the halogen concentration rate.

For the thermodynamical process, the formation enthalpy of the tested compounds has been assessed two different formation pathways. On one hand, the enthalpy relative to the fundamental elements (ΔH_f), on the other, the enthalpy referred to the binary compounds (ΔH_s) used as precursors in the standard synthesis procedure of perovskites.[299,300] Therefore, the formation enthalpy is calculated deducting the total energy of the precursor materials to the total energy of the perovskite compound. Figure 5 of art.º 3 shows the trend of the enthalpy values for the two pathways considered. Negative values in most of the region of compounds studied, with the only exception of the enthalpy vs binary precursors in the region defined by concentration values close to *x*=0 and *b*=0, i.e. $CsPbI_3$ compound, suggest that all the compounds here studied are intrinsically stable and that the proposed substitutions improve the stability of that starting compound. Interestingly, the most and less favored compounds, as well as the trend for all the compounds between those in x and b values, differs for the two pathways. While Br compounds are the ones with lower values of enthalpy (higher intrinsic stability) in both cases, Pb compounds present lower enthalpies when compared to their constituent elements and Sn compounds, on the contrary, are more stable when evaluating the formation from their

precursors. This difference comes from the ease of Pb to form binary compounds with the halogens compared with Sn, presenting the first ones a comparatively lower energy than the second ones when referred in turn to their constituent elements. Similar to what was observed for the Sun's parameter, a transitory deviation from the ascending trend in the ΔH_s enthalpy is observed for compounds with x values of 0.5, i.e., compounds with highly mixed halogen concentration, suggesting a relatively lower intrinsic stability than what could be expected according to the trend. This deviation goes in line with the plateau observed in the Sun's parameter and could be related with the loss of the cubic shape observed for those compounds.

The trends upon concentration variations observed for the formation enthalpies, as the commonly accepted indicators of intrinsic stability of the material, have been compared with those presented for the structural parameters. The advantage of this structural parameters is that they can be obtained without the need of a DFT calculation, or just one in the case of the bonding strength where optimized interatomic distances may be needed in case of highly doped (distorted) structures. For more simple structures where the relaxed structure is well-known it may even not be needed though. This way these parameters can perform as very good predictors of the intrinsic stability of the material, being that already a quite common practice in the case of the Goldschmidt's parameter. In this line, it has been observed that, for the group of compounds under study, the enthalpy against constituent elements is strongly correlated to the Sun's parameter, presenting a MAE of 6.8 meV/atom and a R^2 value of 0.993. These values prove the usefulness of the correction of the Goldschmidt's tolerance factor offered by the Sun's parameter, although the value predicted is the one associated with the constituent elements of the material, of lesser relevance than the enthalpy from binary precursors. To predict this value, the bonding strength performs much better, showing a little worse R^2 of 0.896 but an even better MAE value because of the narrower range of results, that makes this correlation perfectly usable for the compounds under examination.

Ultimately, some mechanical properties were calculated. The bulk modulus was obtained from the Birch-Murnaghan equation,[301,302] while the shear and Young's moduli and the Poisson's ratio were derived from the computed elastic constants according to the Voigt-Reuss-Hill approximations.[303–305] Obtained values for all these properties indicate that the studied materials present good mechanical properties, of relatively low rigidity (shear modulus values between 9-12 GPa), assertion supported by all the compounds meeting the elastic stability and Pugh's criteria, defining them as ductile materials. Looking at Figures 7 and 8 of the art.º3, a marked trend is observed, indicating that Br compounds present a significant improvement of their mechanical properties compared to I compounds. Regarding the bulk modulus, Sn compounds present higher values than Pb compounds, while for the quite alike cases of the shear and Young's moduli the results near the extremes (pure Sn and pure Pb compounds) are very similar between them. For these two last properties, also a substantial decrease of the stiffness to these two kinds of deformation is found for concentration values around b=0.3-0.5, suggesting that compounds close to those concentration rates would be few more brittle. A deviation from values according to the linear trend in all the properties can be noticed again for compounds with anion concentration rates around x=0.5, like it happened for binary precursors formation enthalpy and Sun's parameter.

After a complete revision of properties to some extent related to the stability of these perovskites a new line of work was defined by the partial substitution of Cs by Rb. This partial replacement has been previously evaluated and proposed at small rates as greatly beneficial because of the stability improvement without modifying the bandgap.[298,306–308] In art.º 4,[221] the series of compounds $CsPb_{1-b}Sn_bI_2Br$ is revisited, fixing in this case the halogens partial concentration looking for an optimal solution between the already commented gains in stability by means of Br introduction and the widening of the gap beyond those required for photovoltaic conversion. A small quantity of Rb has been added to these compounds, replacing some of the Cs atoms, mainly covering a partial concentration of 12.5% of this element out of the total monovalent cationic sites. Compounds with this concentration of Rb have been studied and compared with those without it, paying attention to a few stability-related parameters and primarily to their optoelectronic features.

To study these compounds with DFT, the PBEsol functional has been used for the structural relaxation, showing better agreement with experimental results for the lattice constants of the compound's cells than standard PBE functional.[309,310] PBE total energies have been used to evaluate the formation enthalpies of the compounds this time, because of their lower computational cost compared to SCAN calculations and their comparatively similar results. Aiming to obtain accurate optical properties, including the bandgap and absorption spectra of the compounds, an additional method is needed on top of the PBE calculations for a precise electronic configuration. In that sense, several methods were tested, including GW calculations at different levels, HSE06 hybrid functional and a combination of both. Accurate results for the bandgap, according to previously reported experimental values, were not reached with any of these methods, as presented in Table 1 of art.º 4. Therefore, the PBE+U method was used in this occasion, fitting experimental gaps at U values of 5.6 and 11 eV for the d-electrons of Pb and Sn respectively. The need of inclusion of the spin-orbit coupling correction (SOC)[311] to deal with the electromagnetic interactions that takes place between the magnetic dipoles of the d-electrons of Pb and Sn has also been assessed in a specifically dedicated section of art.º 4, where the minor differences in the absorption spectra results and the important extra computational cost associated led to conclude that SOC would not be used in this work.

Focusing on the stability of the compounds, once again the structural distortion, the thermodynamics of the formation process and the Goldschmidt's tolerance factor have been assessed. Because of the introduction of three partial substitutions at the same time in most of the compounds, notable imbalances may take place within the structure because of the different atom sizes, for that reason special attention is given to the structural deformation, with a detailed analysis of the distortion of the BX_6 octahedra forming the perovskite lattice. In Figures 2-4 in art.º 4, the main structural parameters of these perovskites are presented, including lattice parameter and shape factor, with regard to the unit cell, and averaged bond distances and inner angles of the octahedra. From the presented values, and according to what was seen in the previous work for the perovskites without Rb, the lattice constant of the cells monotonically decreases when Sn concentration rises, while the *b*-concentration hardly affects the shape factor (for the case of compounds without Rb). All the compounds here covered present a shortened direction along which Br atoms occupy the vertex of the octahedra, hence

the shown shape factors below unity for all the compounds, also in agreement with the results reported in art.º3. According to the variation of these parameters for the Rb compounds, in comparison with their counterparts without it, three degrees of distortion can be stablished, that will be seen repeatedly across the different properties evaluated.

- The first degree corresponds to the pure Sn and Pb compounds, where the introduction of Rb is hardly noticed in structural terms. The difference of size of the Rb atom compared to the Cs one is diluted throughout the lattice and absorbed by it, that way having practically unnoticeable effects on the lattice constant and just slightly reducing the shape factor. The bond distance between the anions and cations of the octahedra doesn't change practically, while the inner angle deviations are not significant. Henceforth, these two compounds are here classified as not distorted.

- There is a second group of compounds where the Rb atom introduction starts to play a role on the structural distortion of the compound. For compounds with a partial concentration of divalent cations between $0.25 \leq b \leq 0.75$, a modest decrease of the lattice constant takes place, while the minor decrease previously observed for the shape factor turns into a drastic reduction approximately 20 times bigger, still with total variations below 2% of the original value. Significant changes can also be seen in the bond distances, with moderately bigger and tilted up to 2° degrees BX_6 octahedra, because of the deformation of the voids between them occupied by the monovalent cations, clearly seen in the high standard deviations and the variations from Cs to Rb bond distances observed in Figure 3. This group of compounds is for that reason catalogued as slightly distorted.

- Among the distorted compounds, two of them, those where the concentration of Pb or Sn is minimal (b=0.125/0.875), present more pronounced effects caused by the Rb introduction than the rest. The trend in those effects is the same than for the other compounds where distortion is noticed, lower lattice parameter and shape factor, more differences in bond distances (specially along the Br chains direction) and highly modified inner angles, although comparatively the variation is greater that for the case of the other distorted compounds. The inner angle deviations are the most affected measurements, with remarkably higher values more than twice the ones presented for the other compounds in some cases. These two compounds are so grouped together as highly distorted.

Despite distortion is usually considered as an issue for stability, looking at the formation enthalpies shown in Figure 5 in art.º 4, again with the two formation pathways considered as in the previous work, it can be seen that in this particular case, the effect of the structural distortion upon the formation enthalpy of the Rb compounds is towards lower enthalpy values, consequently enhancing their intrinsic stability. While the not distorted compounds exhibit a little higher formation enthalpy than their homologous without Rb, for the rest of the range of *b* concentration rates, the formation enthalpies ΔH_f and ΔH_s are slightly lower. Although talking about beneficial distortion may seem to some extent counterintuitive, perovskites are known to own a very good defect tolerance, being defects in the end another cause of distortion. This

finding is also consistent with previous works where, as commented before, the partial introduction of Rb improved the stability and the passivation of defects in perovskites.[307] It is interesting to see how the Goldschmidt's factor perfectly fits the ΔH_s enthalpy variations, including the linear decrease upon b-concentration variations and the changes when Rb is introduced, outside the effects of distortion, which cannot be predicted by it. This fact reinforces the idea of relating the properties change to the structural distortion and not directly to the composition change, which essence is captured better by the Goldschmidt's parameter. On the contrary, the inverted trend of the ΔH_f, derived of the previously commented lower energies of Pb binary compounds compared with those with Sn, is wrongly described with this predictor in this case.

Studying the electronic configuration and the derived properties that will sketch the photovoltaic potential of these perovskites the differences between the compounds categorized in the three progressive degrees of distortion can be clearly seen too. In Figure 9 in art.º 4, where the bandgaps of all the tested compounds is presented, the linear decrease of bandgaps for the original pure Cs compounds upon Sn addition is shown. Compounds with a higher content of Sn, with lower values of bandgap below 1.5 eV would be more adequate for photovoltaic applications, being able to use a wider range of the solar spectrum photons, however the range of bandgaps of compounds with b-concentrations between 0.125 and 0.5, with values below 1.8 eV could be also useful in tandem configurations or even for SJSCs despite not being optimal. For the compounds with Rb, the different effect of the Rb atom introduction on the structural distortion is also seen in this case. Not distorted compounds present exactly the same bandgap than their counterparts without Rb, as suggested in previous works.[312] Contrarily, distorted compounds exhibit a considerably wider bandgap, approximately 0.25 and 0.4 eV wider for the case of slightly and highly distorted compounds respectively. Aiming to explore in further detail the effects of the Rb addition on the bandgaps, compounds with a smaller rate of Rb (6.25%) have been also studied only for this purpose. As seen in the orange dashed line of the graph, compounds with this smaller rate of Rb, present basically the same bandgaps than compounds without Rb. This result emphasize the role of the structural distortion on the bandgaps variations, and consequently on the photovoltaic potential of the compounds, as no other remarkable differences can be extracted from the qualitative analysis of the band diagrams presented in Figure 10 of art.º 4.

On the basis of the computed electronic configurations, the absorption spectra of all the compounds have been also calculated following the same methodology as in art.º 1, by means of the Kramers-Kronig relation and their dielectric constants. Looking at Figure 11 of art.º 4, where the spectra are presented, it can be confirmed that no great difference besides the bandgap, which cannot be clearly distinguished because of the extended range of energies covered. The slopes of the spectra for all the compounds is quite similar, with no many peaks in them, but for the compounds with more Sn quantities. Although it cannot be easily appreciated in this figure, as presented in Figure 12 of art.º 4 where the area under the spectral curves (AUC) is calculated, both not distorted compounds present barely the same absorption spectra. From that figure it can also be seen how Rb compounds with Sn partial concentrations between 0.5-0.875 present a total AUC a bit higher than the original $CsPbI_2Br$ compound, for which

outstanding efficiencies have been already reported,[313] denoting a comparable photovoltaic potential for these compounds, with the additional advantage of the reduced toxicity consequence of the lower Pb presence and the improved stability. Finally, as an alternative to the AUC for the quantification of the spectra, also taking into account the solar spectra, the SLME of these compounds has been obtained too, according to Yu and Zunger's method.[114] Similar conclusions can be extracted from these additional parameter, presented in Figure 13 of art.º 4 as a function of the thickness of the absorber layer in the device, finding maximum efficiencies close to 25% for the compounds mentioned before.

4.1.3. Configurational analysis with machine learning

In this last section of discussion, where the results from art.º 5[189] are commented, the implementation of the ML in our DFT workflows, and its tremendous usefulness, is reviewed. In it, spinel nitride materials are revisited, this time through a configurational analysis looking at the variations in a couple of basic properties upon the reorganization of the Ge and Sn atoms over the different cationic sites, octahedral and tetrahedral. The focus for this work was on a fixed partial concentration of cations, with twice more Sn than Ge atoms, as the most adequate concentration for standard PV applications (SJSCs and MJSCs) because of the bandgap values. Only for that cations ratio, there are 4222 possible inequivalent configurations, meaning that those configurations considered equivalent after applying basic symmetry operations are not counted. To study each and every one of those configurations with DFT would be quite an effort in terms of computational resources, but thanks to the use of ML we can drastically reduce those resources needed and, by the way, also get some insights on the influence of the different structural patterns on the studied properties of these compounds. That drastic reduction translates into less than a fourth of the total number of configurations computed with DFT, even much less regarding expensive methods for accurate electronic configurations as we will see, and still being able to characterize the whole configurational space with great precision, as the presented metrics of performance for the ML models prove.

The two properties that have been evaluated in this work are the mixing formation energy, as a measurement of the relative stability of every configuration, and the bandgap, to elucidate the real range of tunability of this property upon different cation arrangements, considering the formability of every configuration indicated by their mixing energy. Similar to what was done in previous works here presented, the mixing is calculated by subtracting the energy of the two binary compounds (Sn_3N_4 and Ge_3N_4), weighted according to the concentration of their respective cations in the ternary compound (consequently by 2/3 and 1/3 in this case), to the total energy of every configuration. As bandgap values are targeted as one of the properties to explore, beyond DFT methods are required to obtain precise values. We already saw in the previous subsection where the results from art.º 2 were discussed that accurate bandgaps were achieved for these materials with the GW approximation. However, in this case, due to the number of calculations to perform, a so costly method would be completely unaffordable. Thus, after a thorough method testing, it was decided to use the GGA+U and HSE methods for this second study on spinel nitrides. GGA+U was observed to improve the

agreement in terms of lattice parameters when used for the structural relaxations, without distorting the relative position of the energetic levels of the different electrons. Specially those for which the U was applied, in this case the d-electrons of Sn and Ge, with a very low value for the U of just 2 eV. That improvement can be clearly seen by comparing the values shown in the Table 1 from art.º 5 and those from Figure 2 from art.º 2. On top of those relaxed structures, static calculations with the HSE06 functional were performed to obtain very accurate values of bandgap compared with the experimental references, as seen in Table 1 from art.º 5 as well. Even though significantly less expensive than GW methods, the cost of performing more than a thousand calculations with a hybrid functional like HSE06 would still be huge. For that reason, and taking into account the great similarity between configurations, as part all of the same configurational space, a correlation between results from the first step of calculations with GGA+U, much cheaper, and those with HSE06, more accurate, was stablished after evaluating results for just 59 test configurations. Based on the very good results achieved, with MAEs below 2 meV (Figure 2 from art.º 5), completely derisory talking about bandgaps, these correlated results are used as final values when evaluating the models performance and to be used for extracting conclusions about the studied configurational space.

To characterize all the compounds within the configuration space defined, the results (including correlated bandgaps) from the 1013 DFT calculations carried out were used to train and test different ML models. To ensure the 1013 configurations were representative of the space, those were selected from different groups, proportionately to the total number of configurations in each of them. Those groups were defined according to the structural properties of the configurations, in particular to the occupancy ratio of Sn atoms at tetrahedral sites, defined as the inversion degree, as in the literature about other spinel compounds. Also the 59 configurations selected for the definition of the correlation between GGA+U and HSE results were chosen in that way. More details on the specific way those structures were selected are given at the end of section 2.2 in art.º 5.

To pass input data to the ML models that resembles to some extent the information used for DFT calculations several structural descriptors were tested besides the different models. On the side of descriptors, the CME, the MBTR and the CCFs were used, while on the models side, a standard linear regressor with LASSO regularization, a gradient boosted regressor based on decision trees and a multilayer perceptron were tested. All of them, descriptors and models are described in the corresponding section of chapter 3. More details on the parametrization and specific architecture of the ML models used for this work is given in section 2.3 of art.º 5. The performance of these models and descriptors has been evaluated through a train-test splitting scheme where 10% of the calculated configurations are reserved during the training process to be used later for the evaluation, where the MAE has been used as main metric of performance. The results for the two commented properties under study, in form of MAE between DFT calculated values and ML predictions, with the different model-descriptor pairs tested are presented as heat maps in Figure 3 in art.º 5. From there it is seen that the CCFs are the best performing descriptor with considerable difference, showing MAEs almost twice lower for the case of bandgaps and between 3-5 times better for mixing energies. The best errors achieved are of few meV for both cases, giving a tremendous credibility to the results that will

be outputted for the rest configurations. Other metrics of performance are presented as well in Figure 5 from art.º 5 for the best-performing model-descriptor pair in each case, the CCFs and the LR for the mixing energies and the CCFs with the MLP in the case of bandgaps. There it can be seen that R^2 values are above 0.98, reaching practically unity in the case of mixing energies, while maximum errors are of the order of few tens of meV for both. The errors within the test set configurations have been displayed too, showing that maximum errors are obtained for extreme values and singular configurations, i.e., those with inversion degrees that are also seen in very few configurations, like the only configuration with 0.0 inversion degree. All these results were obtained for training sets consisting of 80% of the calculated configurations, nevertheless, some tests were also performed for the best performing model-descriptors with reduced training sets, made up with 20% and 50% respectively of the configurations computed with DFT (5 and 12% approximately out of the total number of configurations). Those results, seen in Figure 4 from art.º 5, show that using just a 5% of the configurations, similar results to those previously presented could be reached for mixing energies and just slightly worse (around 2 meV higher MAEs) for bandgaps.

Some interesting information can be inferred from the results already presented. In first place is a little surprising that CCFs present the best performing metrics on this task, especially for predicting bandgaps, since the linear combination of CCFs has been in use for predicting energies of alloys within the cluster expansion method (CEM) for quite a long time now.[266,314–316] In contrast, previous works didn't show results as good as the ones obtained here for bandgaps prediction in other systems,[191,317] including a very similar study to this one for Mg and Zn oxides, where much better results were found with the CME. Based on these results we are prone to think that the nature of the chemical bonding might be a key aspect on the decision of the most adequate descriptor, as the more local description of the CCFs seem to be more suitable to describe covalent systems like these spinels, while the better described long-range interactions from CME performed better on more ionic systems. Nevertheless, further research in other alloy system would be needed to delve into this matter. Regarding the models, it seems reasonable based on the previous literature presented that a linear combination of CCFs gives good results for mixing energies, being a similar methodology to the one applied in the CEM, while a more complex model including non-linearities like the MLP captures better the more intricate structural patterns that lead to precise bandgap descriptions.

Apart from the knowledge gained directly from the results, some extra insight can be extracted by performing an analysis of the features importance in the model output. Thanks to it we can know which clusters are the ones with more influence in the model predictions and get to know more about the structural patters that define each property. Figure 6 from art.º 5 shows that importance for each property, mixing energies (6a in form of linear coefficients and 6b in form of SHAP values) and bandgaps (6c as SHAP values).[318] In accordance with the complexity of the model that gives better predictions for each, for mixing energies we see that clusters with higher influence, those which appear with more width in the graph, are of lower order (values for k in the graph), being the most important one by far the cluster corresponding to the individual octahedral sites. Taking into account the ratio of concentration for the two cations is fixed, occupation of sites of one type are univocally defined by occupation in the other,

so the commented individual cluster is analogous to use directly the inversion degree. The proportionality between clusters is also shown in the covariance matrix shown in Figure 7 from art.º 5, where we can see how higher cluster orders are much loosely relate one to each other than clusters of lower order, seeing also the covariance value of 1 for clusters number 1 and 2, i.e., the individual cluster for octahedral and tetrahedral occupation. That way we see that mixing energies in this case are mostly defined by the inversion degree and to a lesser extent by clusters of order two, showing the locality of this property description. On the contrary, for bandgaps the importance is much more distributed among clusters, being the most important ones of the highest order considered, in this case order three. That may raise the question of whether if we could obtain better results for this property including higher order clusters, however the MAEs are really low and for that reason adding extra complexity to the descriptor may not be worth the try, considering the increase of computational resources demanded. The high order of the most important clusters also underlines the complexity of the structural patterns that define bandgap values.

A configurational map can be drawn with the predictions from the models for all the inequivalent configurations in the studied space. With a completely trustable, based on the good metrics of performance, configurational map (see Figure 8 from art.º 5) singular configurations can be identified, like for example those with lowest mixing energies, and so more likely to crystallize, or those with lowest and highest bandgap values. Some trends can also be clearly noticed from the map, which shows for example a strong inverse dependence of the mixing energies upon the inversion degree, indicating that Sn atoms preferably occupy tetrahedral sites, probably because of the bigger size of Sn atoms compared to Ge atoms adjusting better to the tetrahedral sites, with larger interatomic distances as shown in Figure 2 from art.º 2. A weak inverse correlation between mixing energies and bandgaps can be observed too, resulting in bandgaps close to 2 eV corresponding to the more probable configurations. This last relation is weaker as inversion degree decreases, however those are configurations of not much interesting as their mixing energies as those are very unlikely structures to obtain.

Another useful application of our results is to perform a complete thermodynamical analysis of the configurational space. The inversion entropy of these spinels can be calculated through the formula presented in section 3.4 of art.º 5. With it, the free energy of every configuration can be calculated at different temperatures and then we can perform Boltzmann statistics to precisely obtain equilibrium properties, based on the free energies of every configuration. That analysis is presented in Figure 9 of art.º 5, where also the comparison with a traditional model based just on 3 points or configurations is shown. While yielding the same result at low temperatures, we see how the complete model (the one performed with all the configurations) shows significant deviations from the equilibrium inversion degree obtained with the 3 points model, adding much more importance to thermal effects and the related disorder. Thanks to that greater accuracy obtained with our model, we find that if during the synthesis process the characteristic disorder of high temperatures could be maintained, through some synthesis technique implying a rapid quenching for example, that could result in configurations with lower inversion degrees, and consequently with smaller bandgaps. Thus, this

fact could be propitiously used to tune the bandgap of the final compound, achieving bandgaps below 2 eV, more adequate for PV applications.

4.2. Conclusions

The purpose of the work performed in this thesis is to offer novel solutions in form of absorber materials with potential to break into the PV market, thanks to their enhanced absorption features or superior stabilities, replacing current technologies or complementing them. With that in mind, three different groups of materials have been studied trying to elucidate the suitability of their properties to be used either in standard single-junction solar cells (SJSCs), other commercial solutions like TSCs or more advanced configurations like IBSCs. Some of these materials are completely new in the PV field and therefore must be characterized from scratch, whereas others own an already proved potential to make a difference in the field, reason for which their main weak points towards a globalized commercialization are targeted with special attention.

The first group of materials studied corresponds to indium phosphide compounds hyper-doped with different transition metals. Although InP is a widely known III-V semiconductor in the PV industry, the goal in this case is its use as fundamental material to host a IB that could be obtained through that doping process with specific transition metals. Thus, the effect of different dopants on the electronic configuration of the host compound is investigated.

Another group of materials visited, in this case twice with very different studies, are tin and germanium nitride compounds with spinel structure, a family of materials which photovoltaic potential was yet to be explored. For these materials, which exhibit a considerably wider bandgap, not very adequate for SJSCs but much more for TSCs or IBSCs, a similar process was followed looking at the possibility of an IB formation through their doping with transition metals. Trying to take full advantage of the tunability of their bandgap through changes in their cation composition and concentration, also a ML-boosted study was conducted for these spinels, focused this time on the pure material without doping.

Finally, inorganic halide perovskites, one of the most promising family of materials in the PV field, were also studied mainly looking for ways to improve their stability. Devices made up of these materials have already reached PCE values close to those of Si cells, with record efficiencies of 25.7%,[1] 19.0% for inorganic perovskites with the advantage of higher stabilities than their relatives with organic cations.[319,320] Within the broad range of perovskite with PV applications, some of them present wider bandgaps than Si cells, very appropriate for TSCs together with Si. Peak efficiencies beyond 30% have been reached for this kind of devices.[1] Considering the already high efficiencies achieved the main issue of these materials is their degradation, which significantly deteriorate their performance over the operation years. This way, optimal composition to improve stability has been searched in here, keeping a close eye on the structural distortion provoked by the mix of different elements in the perovskite lattice positions.

In all these cases, although in slightly different manners, the work performed here focus on optimization of properties of interest through the modification of chemical composition. Changes in the constituent elements, whether as intrinsic constituents or high-concentration dopants, and in the concentration of every element are so explored, searching for introducing in-gap states to form an IB, to enhance the absorption by propitiously tuning the bandgap or to increase the stability of the material, as a basic requirement to manufacture devices that can operate in the long-term. The results presented in this compendium are a clear example of the great possibilities that this path of compositional engineering may offer, specially together with DFT because of the easiness to explore different compositions at a moderately reduced cost that way, or even ML-boosted DFT studies as the one performed here.

As stated while introducing DFT in the corresponding section of the third chapter of this memory, the great advantage of DFT with respect to other computational methods is its capability to deal with complex systems at a comparatively small cost, let alone the comparison in this sense with experimental research. Additionally, with some experimental reference as guidance to be able to select the most accurate functional and methods for each system, very precise electronic configurations are achieved, being so really useful for the study of materials for optoelectronic applications. Regarding stability, it is difficult and over all extremely expensive to assure with a DFT study whether a certain compound will be stable or not, as there are many pathways and mechanisms of decomposition, including those caused by external agents which are hard to address this way, as well as competitor phases and compounds to address, varying all of those from one material to the other. Besides, thermal effects cannot be addressed directly with this methodology as DFT calculations are performed at 0 K conditions. Experimental guidelines about which of these mechanisms and competitor compounds are the most common and concerning ones for a certain compound may facilitate this task, drastically reducing the extent of the analysis and increasing its applicability. Nevertheless, some calculations can always be performed to get an overall picture about the intrinsic stability of materials.

Reviewing the results presented and discussed in the previous section, for what concerns IB materials studied, all the indicators of the formation of an IB have been verified through the detailed DFT study of these two compounds. First, the dopant atoms introduction in the host compound was evaluated through the energetics of the process and the effects on the structural distortion. Then, the generation of in-gap states was proved through the accurate electronic configurations obtained, also checking that the formation of the IB was related to non-localized defect states through the analysis of its partial density. Finally, the absorption spectra were calculated and from them some rough estimations of a potential efficiency limit were given, with values close to 60% for the cases of Cr-doped InP and Co-doped $Sn_{1.5}Ge_{1.5}N_4$.

Regarding the two works on inorganic halide perovskites, a thorough analysis on the effects of partially or even completely replace Cs, Pb and I, considering $CsPbI_3$ the reference compound, by Rb, Sn and Br respectively was performed. For the range of compounds $CsPb_{1-b}Sn_b(I_{1-x}Br_x)_3$ it was observed that the proposed substitutions tend to improve the intrinsic stability of the compounds, having the *x* concentration ratio considerably more importance in this sense. Compounds with mixtures of halogens at similar proportions (*x* values around 0.5) present a little higher instability that may be caused by the loss of cell symmetry, particularly

accused for those compounds. A correlation between a couple of structural indicators and the formation enthalpy that could be of notable interest to be used as predictors of the stability of these materials was also found. Additionally, focusing on perovskites with a I to Br ratio of 2:1 (*x*=0.66), it was found that at small concentrations of Rb replacing Cs most of the effects that take place are related to the distortion of the structure, in terms of unit cell and interatomic distances giving shape to the BX_6 octahedra that form the perovskite lattice, when that occurs. Thus, pure Sn and Pb compounds hardly change their properties in comparison with their homologous compounds without Rb, while mixed divalent cation compounds present variations in formation enthalpies, counterintuitively favoring stability, and bandgaps proportionately to that distortion, which was quantified in detail. The absorption features of all the $Cs_{0.875}Rb_{0.125}Pb_{1-b}Sn_bI_2Br$ compounds were computed and so it could be concluded that compounds with a b concentration between 0.625 and 0.875 would be very adequate for PV applications, showing improved absorption coefficients, intrinsic stabilities and reduced toxicity compared to the inorganic efficiency champion $CsPbI_3$.

Finally, the great potential of ML combined with DFT exploring vast chemical spaces was demonstrated with the performed configurational analysis of the $GeSn_2N_4$ spinels. Only computing with DFT a bit less than a fourth of the total 4222 configurations, although later on it was seen that very similar results could be obtained with just a 5% of the configurations, the whole space could be described with excellent accuracy, as the metrics of performance from the models applied demonstrate. The most suitable descriptor for this system were found to be CCFs, interestingly opposed to previous findings in other systems, suggesting that optimal solutions are not global and could depend on the nature of the system, conclusion that could be extended to different models according to the complexity of the target property. Thanks to this analysis and its great results some insights about the system were also gained. It could be observed that mixing energies were mostly dependent of the inversion degree of the configuration, and to lesser extent to local structural patterns that explain the range of values within groups. In contrast, to accurately predict bandgaps much more complex structural motifs have to be considered, better captured by non-linear models like a MLP. Relating both target properties, energetically most favored configurations showed highest bandgaps among the predicted range, with values slightly above 2 eV, although it was seen by means of a thermodynamic analysis that, through different thermal processes during the synthesis of the compound, lightly smaller bandgaps could be achieved, being those more feasible at high temperatures.

4.3. Future lines

The research presented in this compendium is completely focused on absorber materials for photovoltaic cells. The absorber material is the most important layer in a solar cell, as the one performing the function it is intended to do, however it is not the only material needed to build a PV device. In commonly used cells with the p-n junction structure, apart from the absorber material, selective contacts are needed to effectively extract the charge carriers generated in the photon absorption process. The use of optimal selective contacts for the

corresponding absorber material is crucial for the performance of the solar cell, as not all the selective contacts are suitable for all the absorbers, because of mismatches in the bands alignment and lattice constants for the correct mechanical bonding. Integrated solutions can be studied with DFT, simulating a whole heterojunction system through slabs of the different materials forming the cell, the absorber material and the holes and electrons transport materials that constitute the selective contacts. The reason for not doing these from the beginning is the tremendous computational cost of these calculations, because of the largely increased number of atoms to consider, which makes the initial study of the absorber material individually a sensible decision. Being the proposal of new photovoltaic devices as a whole one of the goals of the research line in which this thesis is framed, although not of the thesis itself, this kind of more integral studies will be definitively performed, but now that we understand better the absorber materials, know which exact compound has the highest potential and have more expertise on them thanks to the work performed in this thesis.

Concerning absorber materials, some research can still be performed to deeper examine the materials here proposed or to discover new ones with similar or even higher photovoltaic potential. For both directions, exploratory or more specific and detailed studies, it has been demonstrated that DFT, especially in conjunction with ML, offers numerous opportunities to make high impact in materials science. The huge savings in computational resources consequence of applying ML, for example in supervised learning schemes like the one implemented here, into common DFT workflows can be clearly seen in our results, in particular for a configurational analysis, but it could be applied to other chemical spaces of huge size in a similar manner. Thus, the search for new functional materials must be computationally driven, at least at its initial stages.

The importance of disorder in the modelling of more realistic materials is also evident, being the great variation of properties of the different studied configurations shown here a clear example. To take advantage of that fact is possible if further studied with the methodology presented here and thanks to the great progress made in the manufacturing processes involving control of that disorder in solid solutions. The work here presented covering $GeSn_2N_4$ configurational space is planned to be expanded to other compositions with wider bandgaps (higher ratios of Ge-Sn) to explore those compounds more adequate for IBSC configurations, pursuing to enhance their absorption as much as possible. Also perovskites, because of their intrinsic high tolerance to disorder and defects, would be another materials for which a configurational analysis could be of high interest. Analysis that would give continuity to the research line of inorganic perovskites with a mixture of elements in their different structural sites.

Besides disorder, for solar cells, one of the points to carefully address is defects. Most of the times because of their interaction with light and the consequent degradation, certain number of defects appear in the absorber materials. These defects play a major role in the performance of the devices as they are the biggest source of non-radiative recombination, a phenomenon that can drastically reduce PCE, more notably for IBSCs. To delve into this phenomenon and be able to reproduce defective structures in the actual state they are after some time under irradiation is necessary to precisely evaluate the potential of these absorber

materials. In this sense, understanding defects as a special case of disorder where no atoms occupy specific positions within the lattice structure, if trained with the pertinent defective structures, ML models could also be used to perform a complete analysis of the effect of those defects in a similar way to the configurational analysis already performed.

Lastly, the ultimate goal of any theoretical study is to create a solid basis of knowledge that allows to put into practice the subject of the study at the best possible conditions. In this series of works, solar absorber materials are being explored by means of computational tools with certified precision, although none of them, but some perovskites with compositions similar to the ones proposed here, has been expressly tested in an experimental laboratory yet. Trying to synthetize and characterize these materials is a really important step in the process towards obtention of operative devices, as many unexpected difficulties may arise, and probably will, due to the interaction with the surrounding environment or not considered mechanisms. A fruitful synergy between theoretical and experimental analysis can be stablish then, but not before, as experimental results are needed to concentrate efforts and computational resources in the correct issue and some insights obtained from the pertinent analysis like these ones can be very helpful to guide the work in the laboratory as well. This is not a point in our hands, because as computational scientists we do not have the resources nor the knowledge to carry out experimental work, but collaboration with some experimental partners in this sense would be without a doubt a future step to take.

Bibliography

1. NREL. Best Research-Cell Efficiency Chart. Published online June 30, 2022. Accessed December 15, 2022. https://www.nrel.gov/pv/assets/pdfs/best-research-cell-efficiencies-rev220630.pdf

2. Shockley W, Queisser HJ. Detailed Balance Limit of Efficiency of *p-n* Junction Solar Cells. *J Appl Phys*. 1961;32(3):510-519. doi:10.1063/1.1736034

3. De Vos A. Detailed balance limit of the efficiency of tandem solar cells. *J Phys Appl Phys*. 1980;13(5):839-846. doi:10.1088/0022-3727/13/5/018

4. De Vos A, Pauwels H. On the thermodynamic limit of photovoltaic energy conversion. *Appl Phys*. 1981;25(2):119-125. doi:10.1007/BF00901283

5. Fraunhofer Institute for Solar Energy Systems. *Photovoltaics Report*.; 2022. https://www.ise.fraunhofer.de/en/publications/studies/photovoltaics-report.html

6. International Energy Agency (IEA). *Solar PV*.; 2022. https://www.iea.org/reports/solar-pv

7. International Energy Agency (IEA). *Special Report on Solar PV Global Supply Chains*.; 2022. https://www.iea.org/reports/solar-pv-global-supply-chains

8. Yoshikawa K, Kawasaki H, Yoshida W, et al. Silicon heterojunction solar cell with interdigitated back contacts for a photoconversion efficiency over 26%. *Nat Energy*. 2017;2(5):17032. doi:10.1038/nenergy.2017.32

9. Green MA, Dunlop ED, Hohl-Ebinger J, et al. Solar cell efficiency tables (Version 60). *Prog Photovolt Res Appl*. 2022;30(7):687-701. doi:10.1002/pip.3595

10. Hu D, Yuan S, Zhang J, et al. Higher quality composite silicon ingot with monocrystalline and multicrystalline bricks. *Sol Energy*. 2022;244:484-489. doi:10.1016/j.solener.2022.08.068

11. Nakamura M, Yamaguchi K, Kimoto Y, Yasaki Y, Kato T, Sugimoto H. Cd-Free Cu(In,Ga)(Se,S)$_2$ Thin-Film Solar Cell With Record Efficiency of 23.35%. *IEEE J Photovolt*. 2019;9(6):1863-1867. doi:10.1109/JPHOTOV.2019.2937218

12. Candelise C, Speirs JF, Gross RJK. Materials availability for thin film (TF) PV technologies development: A real concern? *Renew Sustain Energy Rev*. 2011;15(9):4972-4981. doi:10.1016/j.rser.2011.06.012

13. Genchi G, Sinicropi MS, Lauria G, Carocci A, Catalano A. The Effects of Cadmium Toxicity. *Int J Environ Res Public Health*. 2020;17(11):3782. doi:10.3390/ijerph17113782

14. Green MA. Thin-film solar cells: review of materials, technologies and commercial status. *J Mater Sci Mater Electron*. 2007;18(S1):15-19. doi:10.1007/s10854-007-9177-9

15. Efaz ET, Rhaman MM, Imam SA, et al. A review of primary technologies of thin-film solar cells. *Eng Res Express*. 2021;3(3):032001. doi:10.1088/2631-8695/ac2353

16. Anderson DL. Chemical composition of the mantle. *J Geophys Res*. 1983;88(S01):B41. doi:10.1029/JB088iS01p00B41

17. Kojima A, Teshima K, Shirai Y, Miyasaka T. Organometal halide perovskites as visible-light sensitizers for photovoltaic cells. *J Am Chem Soc*. 2009;131(17):6050-6051. doi:10.1021/ja809598r

18. Jeong M, Choi IW, Go EM, et al. Stable perovskite solar cells with efficiency exceeding 24.8% and 0.3-V voltage loss. *Science*. 2020;369(6511):1615-1620. doi:10.1126/science.abb7167

19. Correa-Baena JP, Abate A, Saliba M, et al. The rapid evolution of highly efficient perovskite solar cells. *Energy Environ Sci*. 2017;10(3):710-727. doi:10.1039/c6ee03397k

20. Diekmann J, Caprioglio P, Futscher MH, et al. Pathways toward 30% Efficient Single-Junction Perovskite Solar Cells and the Role of Mobile Ions. *Sol RRL*. 2021;5(8):2100219. doi:10.1002/solr.202100219

21. Al-Ashouri A, Köhnen E, Li B, et al. Monolithic perovskite/silicon tandem solar cell with >29% efficiency by enhanced hole extraction. *Science*. 2020;370(6522):1300-1309. doi:10.1126/science.abd4016

22. Ju MG, Chen M, Zhou Y, et al. Toward Eco-friendly and Stable Perovskite Materials for Photovoltaics. *Joule*. 2018;2(7):1231-1241. doi:10.1016/j.joule.2018.04.026

23. Fu Q, Tang X, Huang B, et al. Recent Progress on the Long-Term Stability of Perovskite Solar Cells. *Adv Sci*. 2018;5(5). doi:10.1002/advs.201700387

24. Boyd CC, Cheacharoen R, Leijtens T, McGehee MD. Understanding Degradation Mechanisms and Improving Stability of Perovskite Photovoltaics. *Chem Rev*. 2019;119(5):3418-3451. doi:10.1021/acs.chemrev.8b00336

25. Zhao X, Liu T, Burlingame QC, et al. Accelerated aging of all-inorganic, interface-stabilized perovskite solar cells. *Science*. 2022;377(6603):307-310. doi:10.1126/science.abn5679

26. Tan S, Huang T, Yavuz I, et al. Stability-limiting heterointerfaces of perovskite photovoltaics. *Nature*. 2022;605(7909):268-273. doi:10.1038/s41586-022-04604-5

27. Habisreutinger SN, Reese MO. Building perovskite solar cells that last. *Science*. 2022;377(6603):265-266. doi:10.1126/science.abq7013

28. Jing C, Meng X, Korfiatis GP. Lead leachability in stabilized/solidified soil samples evaluated with different leaching tests. *J Hazard Mater*. 2004;114(1):101-110. doi:10.1016/j.jhazmat.2004.07.017

29. Serrano-Lujan L, Espinosa N, Larsen-Olsen TT, Abad J, Urbina A, Krebs FC. Tin- and lead-based perovskite solar cells under scrutiny: An environmental perspective. *Adv Energy Mater*. 2015;5(20):1-5. doi:10.1002/aenm.201501119

30. Su P, Liu Y, Zhang J, et al. Pb-Based Perovskite Solar Cells and the Underlying Pollution behind Clean Energy: Dynamic Leaching of Toxic Substances from Discarded Perovskite Solar Cells. *J Phys Chem Lett*. 2020;11(8):2812-2817. doi:10.1021/acs.jpclett.0c00503

31. Ikram M, Malik R, Raees R, et al. Recent advancements and future insight of lead-free non-toxic perovskite solar cells for sustainable and clean energy production: A review. *Sustain Energy Technol Assess*. 2022;53:102433. doi:10.1016/j.seta.2022.102433

32. Luo H, Li P, Ma J, Han L, Zhang Y, Song Y. Sustainable Pb Management in Perovskite Solar Cells toward Eco-Friendly Development. *Adv Energy Mater*. 2022;12(30):2201242. doi:10.1002/aenm.202201242

33. Schileo G, Grancini G. Lead or no lead? Availability, toxicity, sustainability and environmental impact of lead-free perovskite solar cells. *J Mater Chem C*. 2021;9(1):67-76. doi:10.1039/D0TC04552G

34. Chen S, Deng Y, Xiao X, Xu S, Rudd PN, Huang J. Preventing lead leakage with built-in resin layers for sustainable perovskite solar cells. *Nat Sustain*. 2021;4(7):636-643. doi:10.1038/s41893-021-00701-x

35. Ravi VK, Mondal B, Nawale VV, Nag A. Don't Let the Lead Out: New Material Chemistry Approaches for Sustainable Lead Halide Perovskite Solar Cells. *ACS Omega*. 2020;5(46):29631-29641. doi:10.1021/acsomega.0c04599

36. Gong Y, Zhu Q, Li B, et al. Elemental de-mixing-induced epitaxial kesterite/CdS interface enabling 13%-efficiency kesterite solar cells. *Nat Energy*. 2022;7(10):966-977. doi:10.1038/s41560-022-01132-4

37. Kim S, Park JS, Walsh A. Identification of Killer Defects in Kesterite Thin-Film Solar Cells. *ACS Energy Lett*. 2018;3(2):496-500. doi:10.1021/acsenergylett.7b01313

38. Dimitrievska M, Oliva F, Guc M, et al. Defect characterisation in $Cu_2ZnSnSe_4$ kesterites via resonance Raman spectroscopy and the impact on optoelectronic solar cell properties. *J Mater Chem A*. 2019;7(21):13293-13304. doi:10.1039/C9TA03625C

39. Crovetto A, Kim S, Fischer M, et al. Assessing the defect tolerance of kesterite-inspired solar absorbers. *Energy Environ Sci*. 2020;13(10):3489-3503. doi:10.1039/D0EE02177F

40. Kim S, Walsh A. *Ab initio* calculation of the detailed balance limit to the photovoltaic efficiency of single p-n junction kesterite solar cells. *Appl Phys Lett*. 2021;118(24):243905. doi:10.1063/5.0049143

41. Tong Y, Xiao Z, Du X, et al. Progress of the key materials for organic solar cells. *Sci China Chem*. 2020;63(6):758-765. doi:10.1007/s11426-020-9726-0

42. Wang K, Li Y, Li Y. Challenges to the Stability of Active Layer Materials in Organic Solar Cells. *Macromol Rapid Commun*. 2020;41(4):1900437. doi:10.1002/marc.201900437

43. Zhu L, Zhang M, Xu J, et al. Single-junction organic solar cells with over 19% efficiency enabled by a refined double-fibril network morphology. *Nat Mater*. 2022;21(6):656-663. doi:10.1038/s41563-022-01244-y

44. Chen W, Zhu Y, Xiu J, et al. Monolithic perovskite/organic tandem solar cells with 23.6% efficiency enabled by reduced voltage losses and optimized interconnecting layer. *Nat Energy*. 2022;7(3):229-237. doi:10.1038/s41560-021-00966-8

45. Wang Y, Lee J, Hou X, et al. Recent Progress and Challenges toward Highly Stable Nonfullerene Acceptor-Based Organic Solar Cells. *Adv Energy Mater*. 2021;11(5):2003002. doi:10.1002/aenm.202003002

46. Fukuda K, Yu K, Someya T. The Future of Flexible Organic Solar Cells. *Adv Energy Mater*. 2020;10(25):2000765. doi:10.1002/aenm.202000765

47. Nozik AJ. Quantum dot solar cells. *Phys E Low-Dimens Syst Nanostructures*. 2002;14(1):115-120. doi:10.1016/S1386-9477(02)00374-0

48. Kirmani AR, Luther JM, Abolhasani M, Amassian A. Colloidal Quantum Dot Photovoltaics: Current Progress and Path to Gigawatt Scale Enabled by Smart Manufacturing. *ACS Energy Lett*. 2020;5(9):3069-3100. doi:10.1021/acsenergylett.0c01453

49. Ferry DK, Whiteside VR, Sellers IR. Pathways to hot carrier solar cells. *J Photonics Energy*. 2022;12(2):022204. doi:10.1117/1.JPE.12.022204

50. Ramiro I, Martí A. Intermediate band solar cells: Present and future. *Prog Photovolt Res Appl*. 2021;29(7):705-713. doi:10.1002/pip.3351

51. Dimmock JAR, Day S, Kauer M, Smith K, Heffernan J. Demonstration of a hot-carrier photovoltaic cell. *Prog Photovolt Res Appl*. 2014;22(2):151-160. doi:10.1002/pip.2444

52. Chen P, Qin M, Chen H, Yang C, Wang Y, Huang F. Cr incorporation in $CuGaS_2$ chalcopyrite: A new intermediate-band photovoltaic material with wide-spectrum solar absorption. *Phys Status Solidi A*. 2013;210(6):1098-1102. doi:10.1002/pssa.201228721

53. Lucena R, Conesa JC, Aguilera I, Palacios P, Wahnón P. V-substituted In_2S_3: an intermediate band material with photocatalytic activity in the whole visible light range. *J Mater Chem A*. 2014;2(22):8236-8245. doi:10.1039/C4TA00513A

54. López N, Reichertz LA, Yu KM, Campman K, Walukiewicz W. Engineering the Electronic Band Structure for Multiband Solar Cells. *Phys Rev Lett*. 2011;106(2):028701. doi:10.1103/PhysRevLett.106.028701

55. Martí A, Antolín E, Stanley CR, et al. Production of Photocurrent due to Intermediate-to-Conduction-Band Transitions: A Demonstration of a Key Operating Principle of the Intermediate-Band Solar Cell. *Phys Rev Lett*. 2006;97(24):247701. doi:10.1103/PhysRevLett.97.247701

56. Ekins-Daukes NJ, Honsberg C, Yamaguchi M. Signature of intermediate band materials from luminescence measurements: 31st IEEE Photovoltaic Specialists Conference - 2005. *Conf Rec IEEE Photovolt Spec Conf*. Published online 2005:49-54. doi:10.1109/PVSC.2005.1488066

57. Green MA. *Third Generation Photovoltaics: Advanced Solar Energy Conversion*. Springer; 2006.

58. Rühle S. Tabulated values of the Shockley–Queisser limit for single junction solar cells. *Sol Energy*. 2016;130:139-147. doi:10.1016/j.solener.2016.02.015

59. Auger P. Sur les rayons β secondaires produits dans un gaz par des rayons X. *Comptes Rendus Hebd Séances Académie Sci*. 1923;177:169-171.

60. Shockley W, Read WT. Statistics of the Recombinations of Holes and Electrons. *Phys Rev*. 1952;87(5):835-842. doi:10.1103/PhysRev.87.835

61. Hall RN. Electron-Hole Recombination in Germanium. *Phys Rev*. 1952;87(2):387-387. doi:10.1103/PhysRev.87.387

62. Luque A, Martí A. Increasing the Efficiency of Ideal Solar Cells by Photon Induced Transitions at Intermediate Levels. *Phys Rev Lett*. 1997;78(26):4. doi:10.1103/PhysRevLett.78.5014

63. Wolf M. Limitations and Possibilities for Improvement of Photovoltaic Solar Energy Converters: Part I: Considerations for Earth's Surface Operation. *Proc IRE*. 1960;48(7):1246-1263. doi:10.1109/JRPROC.1960.287647

64. Hosokawa H, Tamaki R, Sawada T, et al. Solution-processed intermediate-band solar cells with lead sulfide quantum dots and lead halide perovskites. *Nat Commun*. 2019;10(1):43. doi:10.1038/s41467-018-07655-3

65. Ekins-Daukes NJ, Schmidt TW. A molecular approach to the intermediate band solar cell: The symmetric case. *Appl Phys Lett*. 2008;93(6):063507. doi:10.1063/1.2970157

66. Yu KM, Walukiewicz W, Wu J, et al. Diluted II-VI Oxide Semiconductors with Multiple Band Gaps. *Phys Rev Lett*. 2003;91(24):246403. doi:10.1103/PhysRevLett.91.246403

67. Pusch A, Yoshida M, Hylton NP, et al. Limiting efficiencies for intermediate band solar cells with partial absorptivity: the case for a quantum ratchet. *Prog Photovolt Res Appl*. 2016;24(5):656-662. doi:10.1002/pip.2751

68. García G, Sánchez-Palencia P, Palacios P, Wahnón P. Transition Metal-Hyperdoped InP Semiconductors as Efficient Solar Absorber Materials. *Nanomaterials*. 2020;10(2):283. doi:10.3390/nano10020283

69. Sánchez-Palencia P, García G, Conesa JC, Wahnón P, Palacios P. Spinel-Type nitride compounds with improved features as solar cell absorbers. *Acta Mater*. 2020;197:316-329. doi:10.1016/j.actamat.2020.07.034

70. Marsen B, Klemz S, Unold T, Schock HW. Investigation of the Sub-Bandgap Photoresponse in $CuGaS_2$: Fe for Intermediate Band Solar Cells. *Prog Photovolt Res Appl*. 2012;20(6):625-629. doi:10.1002/pip.1197

71. Pavarini E, Koch E, Anders F, Jarrell M, eds. Crystal-field Theory, Tight-binding Method, and Jahn-Teller Effect. In: *Correlated Electrons: From Models to Materials*. Schriften des Forschungszentrums Jülich. Reihe Modeling and Simulation. Forschungszentrum Jülich, Zentralbibliothek, Verlag Jülich; 2012.

72. Hautier G, Jain A, Ong SP. From the computer to the laboratory: materials discovery and design using first-principles calculations. *J Mater Sci*. 2012;47(21):7317-7340. doi:10.1007/s10853-012-6424-0

73. Chen LQ, Chen LD, Kalinin SV, et al. Design and discovery of materials guided by theory and computation. *Npj Comput Mater*. 2015;1(1):1-2. doi:10.1038/npjcompumats.2015.7

74. Olson GB. Designing a New Material World. *Science*. 2000;288(5468):993-998. doi:10.1126/science.288.5468.993

75. National Science and Technology Council. *Materials Genome Initiative*.; 2011. https://www.mgi.gov/sites/default/files/documents/materials_genome_initiative-final.pdf

76. Aspuru-Guzik A, Persson K. *Materials Acceleration Platform: Accelerating Advanced Energy Materials Discovery by Integrating High-Throughput Methods and Artificial Intelligence.* Mission Innovation: Innovation Challenge 6; 2018. https://dash.harvard.edu/handle/1/35164974

77. Draxl C, Scheffler M. The NOMAD laboratory: from data sharing to artificial intelligence. *J Phys Mater*. 2019;2(3):036001. doi:10.1088/2515-7639/ab13bb

78. Schöppe P, Schönherr S, Chugh M, et al. Revealing the origin of the beneficial effect of cesium in highly efficient Cu(In,Ga)Se_2 solar cells. *Nano Energy*. 2020;71:104622. doi:10.1016/j.nanoen.2020.104622

79. Majumdar I, Sahoo SK, Parvan V, et al. Effects of KF and RbF treatments on Cu(In,Ga)Se_2-based solar cells: A combined photoelectron spectroscopy and DFT study. *Appl Surf Sci*. 2021;538:148085. doi:10.1016/j.apsusc.2020.148085

80. Kistanov AA, Cao W, Huttula M, et al. Impact of various dopant elements on the electronic structure of Cu_2ZnSnS_4 (CZTS) thin films: a DFT study. *CrystEngComm*. 2020;22(35):5786-5791. doi:10.1039/D0CE00802H

81. Grau-Luque E, Anefnaf I, Benhaddou N, et al. Combinatorial and machine learning approaches for the analysis of $Cu_2ZnGeSe_4$: influence of the off-stoichiometry on defect formation and solar cell performance. *J Mater Chem A*. 2021;9(16):10466-10476. doi:10.1039/D1TA01299A

82. Shafi MA, Khan L, Ullah S, et al. Novel compositional engineering for ~26% efficient CZTS-perovskite tandem solar cell. *Optik*. 2022;253:168568. doi:10.1016/j.ijleo.2022.168568

83. Jeon NJ, Noh JH, Yang WS, et al. Compositional engineering of perovskite materials for high-performance solar cells. *Nature*. 2015;517(7535):476-480. doi:10.1038/nature14133

84. Prakash J, Singh A, Sathiyan G, et al. Progress in tailoring perovskite based solar cells through compositional engineering: Materials properties, photovoltaic performance and critical issues. *Mater Today Energy*. 2018;9:440-486. doi:10.1016/j.mtener.2018.07.003

85. Jiang Y, He X, Liu T, et al. Intralayer A-Site Compositional Engineering of Ruddlesden–Popper Perovskites for Thermostable and Efficient Solar Cells. *ACS Energy Lett*. 2019;4(6):1216-1224. doi:10.1021/acsenergylett.9b00403

86. Ali R, Zhu ZG, Yan QB, et al. Compositional Engineering Study of Lead-Free Hybrid Perovskites for Solar Cell Applications. *ACS Appl Mater Interfaces*. 2020;12(44):49636-49647. doi:10.1021/acsami.0c14595

87. Park JG, Hong KH. Dual-Site Compositional Engineering of Bismuth-Based Halide Perovskites for Stable and Efficient Lead-free Solar Cells. *J Phys Chem C*. 2021;125(24):13138-13145. doi:10.1021/acs.jpcc.1c02057

88. Ornelas-Cruz I, González I, Pilo J, Trejo A, Oviedo-Roa R, Cruz-Irisson M. Impact of alkaline-earth doping on electronic properties of the photovoltaic perovskite $CsSnI_3$: insights from a DFT perspective. *Dalton Trans*. 2022;51(17):6607-6621. doi:10.1039/D1DT04041C

89. Seminovski Y, Palacios P, Wahnón P. Obtaining an intermediate band photovoltaic material through the Bi insertion in CdTe. *Sol Energy Mater Sol Cells*. 2013;114:99-103. doi:10.1016/j.solmat.2013.03.002

90. García G, Casanova-Páez M, Palacios P, Menéndez-Proupin E, Wahnón P. First principle study of V-implantation in highly-doped silicon materials. *Comput Mater Sci*. 2017;136:207-215. doi:10.1016/j.commatsci.2017.05.005

91. García G, Palacios P, Menéndez-Proupin E, Montero-Alejo AL, Conesa JC, Wahnón P. Influence of chromium hyperdoping on the electronic structure of $CH_3NH_3PbI_3$ perovskite: A first-principles insight. *Sci Rep*. 2018;8(1):1-12. doi:10.1038/s41598-018-20851-x

92. Haunschild R, Barth A, Marx W. Evolution of DFT studies in view of a scientometric perspective. *J Cheminformatics*. 2016;8(1):52. doi:10.1186/s13321-016-0166-y

93. Van Noorden R, Maher B, Nuzzo R. The top 100 papers. *Nat News*. 2014;514(7524):550. doi:10.1038/514550a

94. Chan MKY, Ceder G. Efficient Band Gap Prediction for Solids. *Phys Rev Lett*. 2010;105(19):196403. doi:10.1103/PhysRevLett.105.196403

95. Zheng X, Cohen AJ, Mori-Sánchez P, Hu X, Yang W. Improving Band Gap Prediction in Density Functional Theory from Molecules to Solids. *Phys Rev Lett*. 2011;107(2):026403. doi:10.1103/PhysRevLett.107.026403

96. Xiao H, Tahir-Kheli J, Goddard WAI. Accurate Band Gaps for Semiconductors from Density Functional Theory. *J Phys Chem Lett*. 2011;2(3):212-217. doi:10.1021/jz101565j

97. Verma P, Truhlar DG. Status and Challenges of Density Functional Theory. *Trends Chem*. 2020;2(4):302-318. doi:10.1016/j.trechm.2020.02.005

98. Wing D, Haber JB, Noff R, et al. Comparing time-dependent density functional theory with many-body perturbation theory for semiconductors: Screened range-separated hybrids and the *GW* plus Bethe-Salpeter approach. *Phys Rev Mater*. 2019;3(6):064603. doi:10.1103/PhysRevMaterials.3.064603

99. Kirchner-Hall NE, Zhao W, Xiong Y, Timrov I, Dabo I. Extensive Benchmarking of DFT+U Calculations for Predicting Band Gaps. *Appl Sci*. 2021;11(5):2395. doi:10.3390/app11052395

100. Albrecht S, Reining L, Del Sole R, Onida G. Ab Initio Calculation of Excitonic Effects in the Optical Spectra of Semiconductors. *Phys Rev Lett*. 1998;80(20):4510-4513. doi:10.1103/PhysRevLett.80.4510

101. Rohlfing M, Louie SG. Electron-Hole Excitations in Semiconductors and Insulators. *Phys Rev Lett*. 1998;81(11):2312-2315. doi:10.1103/PhysRevLett.81.2312

102. Rocca D, Lu D, Galli G. Ab initio calculations of optical absorption spectra: Solution of the Bethe–Salpeter equation within density matrix perturbation theory. *J Chem Phys*. 2010;133(16):164109. doi:10.1063/1.3494540

103. Freysoldt C, Grabowski B, Hickel T, et al. First-principles calculations for point defects in solids. *Rev Mod Phys*. 2014;86(1):253-305. doi:10.1103/RevModPhys.86.253

104. Kim S, Hood SN, Park JS, Whalley LD, Walsh A. Quick-start guide for first-principles modelling of point defects in crystalline materials. *J Phys Energy*. 2020;2(3):036001. doi:10.1088/2515-7655/aba081

105. Mosquera-Lois I, Kavanagh SR, Walsh A, Scanlon DO. ShakeNBreak: Navigating the defect configurational landscape. *J Open Source Softw*. 2022;7(80):4817. doi:10.21105/joss.04817

106. Nieminen RM. Issues in first-principles calculations for defects in semiconductors and oxides. *Model Simul Mater Sci Eng*. 2009;17(8):084001. doi:10.1088/0965-0393/17/8/084001

107. Mosquera-Lois I, Kavanagh SR. In search of hidden defects. *Matter*. 2021;4(8):2602-2605. doi:10.1016/j.matt.2021.06.003

108. Whalley LD, Frost JM, Morgan BJ, Walsh A. Impact of nonparabolic electronic band structure on the optical and transport properties of photovoltaic materials. *Phys Rev B*. 2019;99(8):085207. doi:10.1103/PhysRevB.99.085207

109. Kavanagh SR, Scanlon DO, Walsh A, Freysoldt C. Impact of metastable defect structures on carrier recombination in solar cells. *Faraday Discuss*. 2022;239(0):339-356. doi:10.1039/D2FD00043A

110. Kim J, Lee SH, Lee JH, Hong KH. The Role of Intrinsic Defects in Methylammonium Lead Iodide Perovskite. *J Phys Chem Lett*. 2014;5(8):1312-1317. doi:10.1021/jz500370k

111. Kavanagh SR, Walsh A, Scanlon DO. Rapid Recombination by Cadmium Vacancies in CdTe. *ACS Energy Lett*. 2021;6(4):1392-1398. doi:10.1021/acsenergylett.1c00380

112. Kittler M, Seifert W, Krüger O. Electrical Behaviour of Crystal Defects in Silicon Solar Cells. *Solid State Phenom*. 2001;78-79:39-48. doi:10.4028/www.scientific.net/SSP.78-79.39

113. Rau U, Schock HW. Electronic properties of $Cu(In,Ga)Se_2$ heterojunction solar cells–recent achievements, current understanding, and future challenges. *Appl Phys A*. 1999;69(2):131-147. doi:10.1007/s003390050984

114. Yu L, Zunger A. Identification of potential photovoltaic absorbers based on first-principles spectroscopic screening of materials. *Phys Rev Lett*. 2012;108(6):1-5. doi:10.1103/PhysRevLett.108.068701

115. Kim S, Márquez JA, Unold T, Walsh A. Upper limit to the photovoltaic efficiency of imperfect crystals from first principles. *Energy Environ Sci*. 2020;13(5):1481-1491. doi:10.1039/D0EE00291G

116. Jain A, Hautier G, Ong SP, et al. Formation enthalpies by mixing GGA and GGA + U calculations. *Phys Rev B*. 2011;84(4):045115. doi:10.1103/PhysRevB.84.045115

117. Stevanović V, Lany S, Zhang X, Zunger A. Correcting density functional theory for accurate predictions of compound enthalpies of formation: Fitted elemental-phase reference energies. *Phys Rev B*. 2012;85(11):115104. doi:10.1103/PhysRevB.85.115104

118. Kirklin S, Saal JE, Meredig B, et al. The Open Quantum Materials Database (OQMD): assessing the accuracy of DFT formation energies. *Npj Comput Mater*. 2015;1(1):1-15. doi:10.1038/npjcompumats.2015.10

119. Deml AM, O'Hayre R, Wolverton C, Stevanović V. Predicting density functional theory total energies and enthalpies of formation of metal-nonmetal compounds by linear regression. *Phys Rev B*. 2016;93(8):85142. doi:10.1103/PhysRevB.93.085142

120. Friedrich R, Usanmaz D, Oses C, et al. Coordination corrected ab initio formation enthalpies. *Npj Comput Mater*. 2019;5(1):1-12. doi:10.1038/s41524-019-0192-1

121. Jain A, Hautier G, Moore CJ, et al. A high-throughput infrastructure for density functional theory calculations. *Comput Mater Sci*. 2011;50(8):2295-2310. doi:10.1016/j.commatsci.2011.02.023

122. Oses C, Gossett E, Hicks D, et al. AFLOW-CHULL: Cloud-Oriented Platform for Autonomous Phase Stability Analysis. *J Chem Inf Model*. 2018;58(12):2477-2490. doi:10.1021/acs.jcim.8b00393

123. Sun W, Bartel CJ, Arca E, et al. A map of the inorganic ternary metal nitrides. *Nat Mater*. 2019;18(7):732-739. doi:10.1038/s41563-019-0396-2

124. Li Y, Yang K. High-throughput computational design of halide perovskites and beyond for optoelectronics. *WIREs Comput Mol Sci*. 2021;11(3):e1500. doi:10.1002/wcms.1500

125. Zhang T, Cai Z, Chen S. Chemical Trends in the Thermodynamic Stability and Band Gaps of 980 Halide Double Perovskites: A High-Throughput First-Principles Study. *ACS Appl Mater Interfaces*. 2020;12(18):20680-20690. doi:10.1021/acsami.0c03622

126. Sun W, Dacek ST, Ong SP, et al. The thermodynamic scale of inorganic crystalline metastability. *Sci Adv*. 2016;2(11):e1600225. doi:10.1126/sciadv.1600225

127. Lederer Y, Toher C, Vecchio KS, Curtarolo S. The search for high entropy alloys: A high-throughput ab-initio approach. *Acta Mater*. 2018;159:364-383. doi:10.1016/j.actamat.2018.07.042

128. Ikeda Y, Grabowski B, Körmann F. Ab initio phase stabilities and mechanical properties of multicomponent alloys: A comprehensive review for high entropy alloys and compositionally complex alloys. *Mater Charact*. 2019;147:464-511. doi:10.1016/j.matchar.2018.06.019

129. Wang T, Daiber B, Frost JM, et al. Indirect to direct bandgap transition in methylammonium lead halide perovskite. *Energy Environ Sci*. 2017;10(2):509-515. doi:10.1039/c6ee03474h

130. Zhu X, Su H, Marcus RA, Michel-Beyerle ME. Computed and Experimental Absorption Spectra of the Perovskite $CH_3NH_3PbI_3$. *J Phys Chem Lett*. 2014;5(17):3061-3065. doi:10.1021/jz501174e

131. Menéndez-Proupin E, Ríos CLB, Wahnón P. Nonhydrogenic exciton spectrum in perovskite $CH_3NH_3PbI_3$. *Phys Status Solidi - Rapid Res Lett*. 2015;9(10):559-563. doi:10.1002/pssr.201510265

132. Filippetti A, Mattoni A, Caddeo C, Saba MI, Delugas P. Low electron-polar optical phonon scattering as a fundamental aspect of carrier mobility in methylammonium lead halide CH3NH3PbI3 perovskites. *Phys Chem Chem Phys*. 2016;18(22):15352-15362. doi:10.1039/c6cp01402j

133. Montero-Alejo AL, Menéndez-Proupin E, Palacios P, Wahnón P, Conesa JC. Ferroelectric Domains May Lead to Two-Dimensional Confinement of Holes, but not of Electrons, in $CH_3NH_3PbI_3$ Perovskite. *J Phys Chem C*. 2017;121(48):26698-26705. doi:10.1021/acs.jpcc.7b09625

134. Wang Y, Fang WH, Long R, Prezhdo OV. Symmetry Breaking at $MAPbI_3$ Perovskite Grain Boundaries Suppresses Charge Recombination: Time-Domain ab Initio Analysis. *J Phys Chem Lett*. 2019;10(7):1617-1623. doi:10.1021/acs.jpclett.9b00763

135. Even J, Pedesseau L, Jancu JM, Katan C. DFT and k · p modelling of the phase transitions of lead and tin halide perovskites for photovoltaic cells. *Phys Status Solidi RRL – Rapid Res Lett*. 2014;8(1):31-35. doi:10.1002/pssr.201308183

136. Frost JM, Butler KT, Brivio F, Hendon CH, van Schilfgaarde M, Walsh A. Atomistic Origins of High-Performance in Hybrid Halide Perovskite Solar Cells. *Nano Lett*. 2014;14(5):2584-2590. doi:10.1021/nl500390f

137. Hong F, Saparov B, Meng W, Xiao Z, Mitzi DB, Yan Y. Viability of Lead-Free Perovskites with Mixed Chalcogen and Halogen Anions for Photovoltaic Applications. *J Phys Chem C*. 2016;120(12):6435-6441. doi:10.1021/acs.jpcc.6b00920

138. Rajeev Kumar N, Radhakrishnan R. Electronic, optical and mechanical properties of lead-free halide double perovskites using first-principles density functional theory. *Mater Lett*. 2018;227:289-291. doi:10.1016/j.matlet.2018.05.082

139. Li Q, Cao D, Liu X, Zhou X, Chen X, Shu H. Hierarchical computational screening of layered lead-free metal halide perovskites for optoelectronic applications. *J Mater Chem A*. 2021;9(10):6476-6486. doi:10.1039/D0TA10098F

140. Bousahla MA, Faizan M, Seddik T, et al. DFT study on the crystal structure, optoelectronic, and thermoelectric properties of lead-free inorganic A_2PdBr_6 (A = K, Rb, and Cs) perovskites. *Mater Today Commun*. 2022;30:103061. doi:10.1016/j.mtcomm.2021.103061

141. Ahmed H, Mukhtar S, Agathopoulos S, Ilyas SZ. Structural, Electronic, and Optical Properties of Ga-Based Lead-Free Mixed-Halide Perovskites $Cs_3GaI_{6-x}Br_x$ ($0 \le x \le 6$) for Solar Cell Applications: A DFT Study. *Phys B Condens Matter*. 2022;640:414085. doi:10.1016/j.physb.2022.414085

142. Umari P, Mosconi E, De Angelis F. Relativistic GW calculations on $CH_3NH_3PbI_3$ and $CH_3NH_3SnI_3$ Perovskites for Solar Cell Applications. *Sci Rep*. 2014;4(1):4467. doi:10.1038/srep04467

143. Ma ZQ, Pan H, Wong PK. A First-Principles Study on the Structural and Electronic Properties of Sn-Based Organic–Inorganic Halide Perovskites. *J Electron Mater*. 2016;45(11):5956-5966. doi:10.1007/s11664-016-4822-9

144. A decade of perovskite photovoltaics. *Nat Energy*. 2019;4(1):1-1. doi:10.1038/s41560-018-0323-9

145. Fadla MA, Bentria B, Dahame T, Benghia A. First-principles investigation on the stability and material properties of all-inorganic cesium lead iodide perovskites $CsPbI_3$ polymorphs. *Phys B Condens Matter*. 2020;585(January):412118. doi:10.1016/j.physb.2020.412118

146. Li J, Yu Q, He Y, et al. $Cs_2PbI_2Cl_2$, All-Inorganic Two-Dimensional Ruddlesden–Popper Mixed Halide Perovskite with Optoelectronic Response. *J Am Chem Soc*. 2018;140(35):11085-11090. doi:10.1021/jacs.8b06046

147. Mao X, Sun L, Wu T, Chu T, Deng W, Han K. First-Principles Screening of All-Inorganic Lead-Free ABX_3 Perovskites. *J Phys Chem C*. Published online March 20, 2018. doi:10.1021/acs.jpcc.8b02448

148. Liu D, Peng H, Li Q, Sa R. A DFT study of the stability and optoelectronic properties of all-inorganic lead-free halide perovskites. *J Phys Chem Solids*. 2022;161:110413. doi:10.1016/j.jpcs.2021.110413

149. Jin RJ, Lou YH, Wang ZK. Doping Strategies for Promising Organic–Inorganic Halide Perovskites. *Small*. Published online 2023:2206581. doi:10.1002/smll.202206581

150. Euvrard J, Yan Y, Mitzi DB. Electrical doping in halide perovskites. *Nat Rev Mater*. 2021;6(6):531-549. doi:10.1038/s41578-021-00286-z

151. Chen Y, Jing H, Ling F, et al. Tuning the electronic structures of all-inorganic lead halide perovskite $CsPbI_3$ via heterovalent doping: A first-principles investigation. *Chem Phys Lett*. 2019;722:90-95. doi:10.1016/j.cplett.2019.02.050

152. Volonakis G, Filip MR, Haghighirad AA, et al. Lead-Free Halide Double Perovskites via Heterovalent Substitution of Noble Metals. *J Phys Chem Lett*. 2016;7(7):1254-1259. doi:10.1021/acs.jpclett.6b00376

153. Palacios P, Sánchez K, Conesa JC, Fernández JJ, Wahnón P. Theoretical modelling of intermediate band solar cell materials based on metal-doped chalcopyrite compounds. *Thin Solid Films*. 2007;515(15):6280-6284. doi:10.1016/j.tsf.2006.12.170

154. Seminovski Y, Palacios P, Wahnón P. Analysis of SnS_2 hyperdoped with V proposed as efficient absorber material. *J Phys Condens Matter*. 2014;26(39):395501. doi:10.1088/0953-8984/26/39/395501

155. Vörös M, Galli G, Zimanyi GT. Colloidal Nanoparticles for Intermediate Band Solar Cells. *ACS Nano*. 2015;9(7):6882-6890. doi:10.1021/acsnano.5b00332

156. Rasukkannu M, Velauthapillai D, Vajeeston P. Computational Modeling of Novel Bulk Materials for the Intermediate-Band Solar Cells. *ACS Omega*. 2017;2(4):1454-1462. doi:10.1021/acsomega.6b00534

157. Rasukkannu M, Velauthapillai D, Vajeeston P. A first-principle study of the electronic, mechanical and optical properties of inorganic perovskite Cs_2SnI_6 for intermediate-band solar cells. *Mater Lett*. 2018;218:233-236. doi:10.1016/j.matlet.2018.02.034

158. Sogabe T, Hung CY, Tamaki R, et al. Experimental demonstration of energy-transfer ratchet intermediate-band solar cell. *Commun Phys*. 2021;4(1):1-10. doi:10.1038/s42005-021-00543-1

159. Luque A, Martí A. The Intermediate Band Solar Cell: Progress Toward the Realization of an Attractive Concept. *Adv Mater*. 2010;22(2):160-174. doi:10.1002/adma.200902388

160. Schmidt J, Marques MRG, Botti S, Marques MAL. Recent advances and applications of machine learning in solid-state materials science. *Npj Comput Mater*. 2019;5:83. doi:10.1038/s41524-019-0221-0

161. Kulik HJ, Hammerschmidt T, Schmidt J, et al. Roadmap on Machine learning in electronic structure. *Electron Struct*. 2022;4(2):023004. doi:10.1088/2516-1075/ac572f

162. Hautier G, Fischer CC, Jain A, Mueller T, Ceder G. Finding Nature's Missing Ternary Oxide Compounds Using Machine Learning and Density Functional Theory. *Chem Mater*. 2010;22(12):3762-3767. doi:10.1021/cm100795d

163. Schmidt J, Chen L, Botti S, Marques MAL. Predicting the stability of ternary intermetallics with density functional theory and machine learning. *J Chem Phys*. 2018;148(24):241728. doi:10.1063/1.5020223

164. Davies DW, Butler KT, Walsh A. Data-Driven Discovery of Photoactive Quaternary Oxides Using First-Principles Machine Learning. *Chem Mater*. 2019;31(18):7221-7230. doi:10.1021/acs.chemmater.9b01519

165. Schmidt J, Shi J, Borlido P, Chen L, Botti S, Marques MAL. Predicting the Thermodynamic Stability of Solids Combining Density Functional Theory and Machine Learning. *Chem Mater*. 2017;29(12):5090-5103. doi:10.1021/acs.chemmater.7b00156

166. Li W, Jacobs R, Morgan D. Predicting the thermodynamic stability of perovskite oxides using machine learning models. *Comput Mater Sci*. 2018;150:454-463. doi:10.1016/j.commatsci.2018.04.033

167. Im J, Lee S, Ko TW, Kim HW, Hyon Y, Chang H. Identifying Pb-free perovskites for solar cells by machine learning. *Npj Comput Mater*. 2019;5(1):1-8. doi:10.1038/s41524-019-0177-0

168. Stanley JC, Mayr F, Gagliardi A. Machine Learning Stability and Bandgaps of Lead-Free Perovskites for Photovoltaics. *Adv Theory Simul*. 2020;3(1):1900178. doi:10.1002/adts.201900178

169. Gu GH, Jang J, Noh J, Walsh A, Jung Y. Perovskite synthesizability using graph neural networks. *Npj Comput Mater*. 2022;8(1):1-8. doi:10.1038/s41524-022-00757-z

170. Jørgensen PB, Mesta M, Shil S, et al. Machine learning-based screening of complex molecules for polymer solar cells. *J Chem Phys*. 2018;148(24):241735. doi:10.1063/1.5023563

171. Padula D, D. Simpson J, Troisi A. Combining electronic and structural features in machine learning models to predict organic solar cells properties. *Mater Horiz*. 2019;6(2):343-349. doi:10.1039/C8MH01135D

172. Mahmood A, Wang JL. Machine learning for high performance organic solar cells: current scenario and future prospects. *Energy Environ Sci*. 2021;14(1):90-105. doi:10.1039/D0EE02838J

173. Lee A, Sarker S, Saal JE, et al. Machine learned synthesizability predictions aided by density functional theory. *Commun Mater*. 2022;3(1):1-11. doi:10.1038/s43246-022-00295-7

174. Meredig B, Agrawal A, Kirklin S, et al. Combinatorial screening for new materials in unconstrained composition space with machine learning. *Phys Rev B*. 2014;89(9):094104. doi:10.1103/PhysRevB.89.094104

175. Laakso J, Todorović M, Li J, Zhang GX, Rinke P. Compositional engineering of perovskites with machine learning. *Phys Rev Mater*. 2022;6(11):113801. doi:10.1103/PhysRevMaterials.6.113801

176. Zhuo Y, Mansouri Tehrani A, Brgoch J. Predicting the Band Gaps of Inorganic Solids by Machine Learning. *J Phys Chem Lett*. 2018;9(7):1668-1673. doi:10.1021/acs.jpclett.8b00124

177. Borlido P, Schmidt J, Huran AW, Tran F, Marques MAL, Botti S. Exchange-correlation functionals for band gaps of solids: benchmark, reparametrization and machine learning. *Npj Comput Mater*. 2020;6(1):1-17. doi:10.1038/s41524-020-00360-0

178. Wang T, Tan X, Wei Y, Jin H. Accurate bandgap predictions of solids assisted by machine learning. *Mater Today Commun*. 2021;29:102932. doi:10.1016/j.mtcomm.2021.102932

179. Brandt RE, Stevanović V, Ginley DS, Buonassisi T. Identifying defect-tolerant semiconductors with high minority-carrier lifetimes: Beyond hybrid lead halide perovskites. *MRS Commun*. 2015;5(2):265-275. doi:10.1557/mrc.2015.26

180. Choudhary K, Bercx M, Jiang J, Pachter R, Lamoen D, Tavazza F. Accelerated Discovery of Efficient Solar Cell Materials Using Quantum and Machine-Learning Methods. *Chem Mater*. 2019;31(15):5900-5908. doi:10.1021/acs.chemmater.9b02166

181. Feng HJ, Wu K, Deng ZY. Predicting Inorganic Photovoltaic Materials with Efficiencies >26% via Structure-Relevant Machine Learning and Density Functional Calculations. *Cell Rep Phys Sci*. 2020;1(9):100179. doi:10.1016/j.xcrp.2020.100179

182. Pilania G, Wang C, Jiang X, Rajasekaran S, Ramprasad R. Accelerating materials property predictions using machine learning. *Sci Rep*. 2013;3(1):2810. doi:10.1038/srep02810

183. Morita K, Davies DW, Butler KT, Walsh A. Modeling the dielectric constants of crystals using machine learning. *J Chem Phys*. 2020;153:024503. doi:10.1063/5.0013136

184. Arrigoni M, Madsen GKH. Evolutionary computing and machine learning for discovering of low-energy defect configurations. *Npj Comput Mater*. 2021;7(1):1-13. doi:10.1038/s41524-021-00537-1

185. Pentyala P, Singhania V, Duggineni VK, Deshpande PA. Machine learning-assisted DFT reveals key descriptors governing the vacancy formation energy in Pd-substituted multicomponent ceria. *Mol Catal*. 2022;522:112190. doi:10.1016/j.mcat.2022.112190

186. Artrith N. Machine learning for the modeling of interfaces in energy storage and conversion materials. *J Phys Energy*. 2019;1(3):032002. doi:10.1088/2515-7655/ab2060

187. Huang Y, Yu C, Chen W, et al. Band gap and band alignment prediction of nitride-based semiconductors using machine learning. *J Mater Chem C*. 2019;7(11):3238-3245. doi:10.1039/C8TC05554H

188. Braeckevelt T, Goeminne R, Vandenhaute S, et al. Accurately Determining the Phase Transition Temperature of $CsPbI_3$ via Random-Phase Approximation Calculations and Phase-Transferable Machine Learning Potentials. *Chem Mater*. 2022;34(19):8561-8576. doi:10.1021/acs.chemmater.2c01508

189. Sánchez-Palencia P, Hamad S, Palacios P, Grau-Crespo R, Butler KT. Spinel nitride solid solutions: charting properties in the configurational space with explainable machine learning. *Digit Discov*. 2022;1(5):665-678. doi:10.1039/D2DD00038E

190. Eremin RA, Zolotarev PN, Ivanshina OYu, Bobrikov IA. $Li(Ni,Co,Al)O_2$ Cathode Delithiation: A Combination of Topological Analysis, Density Functional Theory, Neutron Diffraction, and Machine Learning Techniques. *J Phys Chem C*. 2017;121(51):28293-28305. doi:10.1021/acs.jpcc.7b09760

191. Midgley SD, Hamad S, Butler KT, Grau-Crespo R. Bandgap Engineering in the Configurational Space of Solid Solutions via Machine Learning: (Mg,Zn)O Case Study. *J Phys Chem Lett*. 2021;12(21):5163-5168. doi:10.1021/acs.jpclett.1c01031

192. Birschitzky VC, Ellinger F, Diebold U, Reticcioli M, Franchini C. Machine learning for exploring small polaron configurational space. *Npj Comput Mater*. 2022;8(1):1-9. doi:10.1038/s41524-022-00805-8

193. Ghanekar PG, Deshpande S, Greeley J. Adsorbate chemical environment-based machine learning framework for heterogeneous catalysis. *Nat Commun*. 2022;13(1):5788. doi:10.1038/s41467-022-33256-2

194. von Lilienfeld OA, Burke K. Retrospective on a decade of machine learning for chemical discovery. *Nat Commun*. 2020;11(1):4895. doi:10.1038/s41467-020-18556-9

195. Behler J, Parrinello M. Generalized Neural-Network Representation of High-Dimensional Potential-Energy Surfaces. *Phys Rev Lett*. 2007;98(14):146401. doi:10.1103/PhysRevLett.98.146401

196. Chen S, Hou Y, Chen H, et al. Exploring the Stability of Novel Wide Bandgap Perovskites by a Robot Based High Throughput Approach. *Adv Energy Mater*. 2018;8(6):1701543. doi:10.1002/aenm.201701543

197. Li F, Peng X, Wang Z, et al. Machine Learning (ML)-Assisted Design and Fabrication for Solar Cells. *ENERGY Environ Mater*. 2019;2(4):280-291. doi:10.1002/eem2.12049

198. Higgins K, Valleti SM, Ziatdinov M, Kalinin SV, Ahmadi M. Chemical Robotics Enabled Exploration of Stability in Multicomponent Lead Halide Perovskites via Machine Learning. *ACS Energy Lett*. 2020;5(11):3426-3436. doi:10.1021/acsenergylett.0c01749

199. Kirman J, Johnston A, Kuntz DA, et al. Machine-Learning-Accelerated Perovskite Crystallization. *Matter*. 2020;2(4):938-947. doi:10.1016/j.matt.2020.02.012

200. Kim D, Muckley ES, Creange N, et al. Exploring Transport Behavior in Hybrid Perovskites Solar Cells via Machine Learning Analysis of Environmental-Dependent Impedance Spectroscopy. *Adv Sci*. 2021;8(15):2002510. doi:10.1002/advs.202002510

201. Sun S, Tiihonen A, Oviedo F, et al. A data fusion approach to optimize compositional stability of halide perovskites. *Matter*. 2021;4(4):1305-1322. doi:10.1016/j.matt.2021.01.008

202. Gong S, Wang S, Xie T, et al. Calibrating DFT Formation Enthalpy Calculations by Multifidelity Machine Learning. *JACS Au*. 2022;2(9):1964-1977. doi:10.1021/jacsau.2c00235

203. Yu L, Kokenyesi RS, Keszler DA, Zunger A. Inverse Design of High Absorption Thin-Film Photovoltaic Materials. *Adv Energy Mater*. 2013;3(1):43-48. doi:10.1002/aenm.201200538

204. Zunger A. Inverse design in search of materials with target functionalities. *Nat Rev Chem*. 2018;2(4):1-16. doi:10.1038/s41570-018-0121

205. Chen L, Zhang W, Nie Z, Li S, Pan F. Generative models for inverse design of inorganic solid materials. *J Mater Inform*. 2021;1(1):4. doi:10.20517/jmi.2021.07

206. Coley CW. Defining and Exploring Chemical Spaces. *Trends Chem*. 2021;3(2):133-145. doi:10.1016/j.trechm.2020.11.004

207. Westermayr J, Gilkes J, Barrett R, Maurer RJ. High-throughput property-driven generative design of functional organic molecules. *Nat Comput Sci*. Published online February 6, 2023:1-10. doi:10.1038/s43588-022-00391-1

208. United Nations. *The Sustainable Development Goals Report 2022*.; 2022. https://unstats.un.org/sdgs/report/2022/

209. European Commission. *State of the Energy Union 2022*.; 2022. https://eur-lex.europa.eu/legal-content/EN/TXT/?uri=CELEX%3A52022DC0547&qid=1666595113558

210. International Renewable Energy Agency (IRENA). *World Energy Transitions Outlook 2022: 1.5°C Pathway*.; 2022. https://www.irena.org/publications/2022/Mar/World-Energy-Transitions-Outlook-2022

211. International Energy Agency (IEA). *World Energy Outlook 2022*.; 2022. https://www.iea.org/reports/world-energy-outlook-2022

212. BloombergNEF. *Executive Factbook*.; 2021. https://assets.bbhub.io/professional/sites/24/BNEF-2021-Executive-Factbook.pdf

213. Lazard. *Lazard's Levelized Cost of Energy Analysis*.; 2021. https://www.lazard.com/media/451905/lazards-levelized-cost-of-energy-version-150-vf.pdf

214. International Renewable Energy Agency (IRENA). *Renewable Capacity Statistics 2022*.; 2022. https://www.irena.org/Publications/2022/Apr/Renewable-Capacity-Statistics-2022

215. bp. *Statistical Review of World Energy 2022*.; 2022. https://www.bp.com/en/global/corporate/energy-economics/statistical-review-of-world-energy.html

216. bp. Statistical Review of World Energy - Historical Data Workbook. Published online 2022. https://www.bp.com/en/global/corporate/energy-economics/statistical-review-of-world-energy.html

217. Surana K, Jordaan SM. The climate mitigation opportunity behind global power transmission and distribution. *Nat Clim Change*. 2019;9(9):660-665. doi:10.1038/s41558-019-0544-3

218. Hoffacker MK, Hernandez RR. Local Energy: Spatial Proximity of Energy Providers to Their Power Resources. *Front Sustain*. 2020;1:585110. doi:10.3389/frsus.2020.585110

219. NREL. Champion Module Efficiencies. Published online April 1, 2022. Accessed January 3, 2023. https://www.nrel.gov/pv/assets/pdfs/champion-module-efficiencies-rev220401b.pdf

220. Sánchez-Palencia P, García G, Wahnón P, Palacios P. The effects of the chemical composition on the structural, thermodynamic, and mechanical properties of all-inorganic halide perovskites. *Inorg Chem Front*. 2021;8(16):3803-3814. doi:10.1039/D1QI00347J

221. Sánchez-Palencia P, García G, Wahnón P, Palacios P. Cation substitution effects on the structural, electronic and sun-light absorption features of all-inorganic halide perovskites. *Inorg Chem Front*. 2022;9(7):1337-1353. doi:10.1039/D1QI01553B

222. Schrödinger E. An undulatory theory of the mechanics of atoms and molecules. *Phys Rev*. 1926;28(6):1049-1070. doi:10.1103/PhysRev.28.1049

223. Hohenberg P, Kohn W. Inhomogeneous Electron Gas. *Phys Rev*. 1964;136(3B):864-871. doi:10.1103/PhysRev.136.B864

224. Kohn W, Sham LJ. Self-Consistent Equations Including Exchange and Correlation Effects. *Phys Rev*. 1965;140(4A):1133-1138. doi:10.1103/PhysRev.140.A1133

225. Perdew JP, Burke K, Ernzerhof M. Generalized gradient approximation made simple. *Phys Rev Lett*. 1996;77(18):3865-3868. doi:10.1103/PhysRevLett.77.3865

226. Stephens PJ, Devlin FJ, Chabalowski CF, Frisch MJ. Ab Initio Calculation of Vibrational Absorption and Circular Dichroism Spectra Using Density Functional Force Fields. *J Phys Chem*. 1994;98:11623-11627. doi:10.1021/j100096a001

227. Aryasetiawan F, Gunnarsson O. The GW method. *Rep Prog Phys*. 1998;61(3):237. doi:10.1088/0034-4885/61/3/002

228. Hartree DR, Hartree W. Self-consistent field, with exchange, for beryllium. *Proc R Soc Lond Ser Math Phys Sci*. 1935;150(869):9-33. doi:10.1098/rspa.1935.0085

229. Fock V. „Selfconsistent field“ mit Austausch für Natrium. *Z Für Phys*. 1930;62(11):795-805. doi:10.1007/BF01330439

230. Hubbard J. Electron correlations in narrow energy bands. *Proc R Soc Lond Ser Math Phys Sci*. 1963;276(1365):238-257. doi:10.1098/rspa.1963.0204

231. Born M, Oppenheimer R. Zur Quantentheorie der Molekeln. *Ann Phys*. 1927;389(20):457-484. doi:10.1002/andp.19273892002

232. Dirac PAM. A new notation for quantum mechanics. *Math Proc Camb Philos Soc*. 1939;35(3):416-418. doi:10.1017/S0305004100021162

233. Slater JC. The Theory of Complex Spectra. *Phys Rev*. 1929;34(10):1293-1322. doi:10.1103/PhysRev.34.1293

234. Lehtola S, Steigemann C, Oliveira MJT, Marques MAL. Recent developments in libxc — A comprehensive library of functionals for density functional theory. *SoftwareX*. 2018;7:1-5. doi:10.1016/j.softx.2017.11.002

235. Perdew JP. Jacob’s ladder of density functional approximations for the exchange-correlation energy. In: *AIP Conference Proceedings*. Vol 577. AIP; 2001:1-20. doi:10.1063/1.1390175

236. Ceperley DM, Alder BJ. Ground State of the Electron Gas by a Stochastic Method. *Phys Rev Lett*. 1980;45(7):566-569. doi:10.1103/PhysRevLett.45.566

237. Perdew JP, Zunger A. Self-interaction correction to density-functional approximations for many-electron systems. *Phys Rev B*. 1981;23(10):5048-5079. doi:10.1103/PhysRevB.23.5048

238. Perdew JP, Wang Y. Accurate and simple analytic representation of the electron-gas correlation energy. *Phys Rev B*. 1992;45(23):13244-13249. doi:10.1103/PhysRevB.45.13244

239. Perdew JP, Ruzsinszky A, Csonka GI, et al. Restoring the density-gradient expansion for exchange in solids and surfaces. *Phys Rev Lett*. 2008;100(13):1-4. doi:10.1103/PhysRevLett.100.136406

240. Sun J, Ruzsinszky A, Perdew J. Strongly Constrained and Appropriately Normed Semilocal Density Functional. *Phys Rev Lett*. 2015;115(3):1-6. doi:10.1103/PhysRevLett.115.036402

241. Becke AD. Density-functional thermochemistry. III. The role of exact exchange. *J Chem Phys*. 1993;98(7):5648-5652. doi:10.1063/1.464913

242. Lee C, Yang W, Parr RG. Development of the Colle-Salvetti correlation-energy formula into a functional of the electron density. *Phys Rev B*. 1988;37(2):785-789. doi:10.1103/PhysRevB.37.785

243. Vosko SH, Wilk L, Nusair M. Accurate spin-dependent electron liquid correlation energies for local spin density calculations: a critical analysis. *Can J Phys*. 1980;58(8):1200-1211. doi:10.1139/p80-159

244. Heyd J, Scuseria GE, Ernzerhof M. Hybrid functionals based on a screened Coulomb potential. *J Chem Phys*. 2003;118(18):8207-8215. doi:10.1063/1.1564060

245. Hartree DR. The Wave Mechanics of an Atom with a Non-Coulomb Central Field. Part I. Theory and Methods. *Math Proc Camb Philos Soc*. 1928;24(1):89-110. doi:10.1017/S0305004100011919

246. Hartree DR. The Wave Mechanics of an Atom with a Non-Coulomb Central Field. Part II. Some Results and Discussion. *Math Proc Camb Philos Soc*. 1928;24(1):111-132. doi:10.1017/S0305004100011920

247. Hartree DR. The Wave Mechanics of an Atom with a non-Coulomb Central Field. Part III. Term Values and Intensities in Series in Optical Spectra. *Math Proc Camb Philos Soc*. 1928;24(3):426-437. doi:10.1017/S0305004100015954

248. Fock V. Näherungsmethode zur Lösung des quantenmechanischen Mehrkörperproblems. *Z Für Phys*. 1930;61(1):126-148. doi:10.1007/BF01340294

249. Slater JC. Note on Hartree's Method. *Phys Rev*. 1930;35(2):210-211. doi:10.1103/PhysRev.35.210.2

250. Wannier GH. The Structure of Electronic Excitation Levels in Insulating Crystals. *Phys Rev*. 1937;52(3):191-197. doi:10.1103/PhysRev.52.191

251. Dudarev S, Botton G. Electron-energy-loss spectra and the structural stability of nickel oxide: An LSDA+U study. *Phys Rev B*. 1998;57(3):1505-1509. doi:10.1103/PhysRevB.57.1505

252. Hedin L. New Method for Calculating the One-Particle Green's Function with Application to the Electron-Gas Problem. *Phys Rev*. 1965;139(3A):796-823. doi:10.1103/PhysRev.139.A796

253. Abadi M, Agarwal A, Barham P, et al. TensorFlow: Large-Scale Machine Learning on Heterogeneous Distributed Systems. doi:10.5281/zenodo.4724125

254. Larsen AH, Mortensen JJ, Blomqvist J, et al. The atomic simulation environment—a Python library for working with atoms. *J Phys Condens Matter*. 2017;29(27):273002. doi:10.1088/1361-648X/aa680e

255. Ong SP, Richards WD, Jain A, et al. Python Materials Genomics (pymatgen): A robust, open-source python library for materials analysis. *Comput Mater Sci*. 2013;68:314-319. doi:10.1016/j.commatsci.2012.10.028

256. Himanen L, Jäger MOJ, Morooka EV, et al. DScribe: Library of descriptors for machine learning in materials science. *Comput Phys Commun*. 2020;247:undefined-undefined. doi:10.1016/j.cpc.2019.106949

257. Ward L, Dunn A, Faghaninia A, et al. Matminer: An open source toolkit for materials data mining. *Comput Mater Sci*. 2018;152:60-69. doi:10.1016/j.commatsci.2018.05.018

258. Troppenz M, Rigamonti S, Draxl C. Predicting Ground-State Configurations and Electronic Properties of the Thermoelectric Clathrates $Ba_8Al_xSi_{46-x}$ and $Sr_8Al_xSi_{46-x}$. *Chem Mater*. 2017;29(6):2414-2424. doi:10.1021/acs.chemmater.6b05027

259. Rigamonti S, Troppenz M, Kuban M, et al. CELL: a python package for cluster expansion with a focus on complex alloys. Published online To be published.

260. Tibshirani R. Regression Shrinkage and Selection Via the Lasso. *J R Stat Soc Ser B Methodol*. 1996;58(1):267-288. doi:10.1111/j.2517-6161.1996.tb02080.x

261. Friedman JH. Stochastic gradient boosting. *Comput Stat Data Anal*. 2002;38(4):367-378. doi:10.1016/S0167-9473(01)00065-2

262. Hornik K, Stinchcombe M, White H. Multilayer feedforward networks are universal approximators. *Neural Netw*. 1989;2(5):359-366. doi:10.1016/0893-6080(89)90020-8

263. Faber F, Lindmaa A, Von Lilienfeld OA, Armiento R. Crystal structure representations for machine learning models of formation energies. *Int J Quantum Chem*. 2015;115(16):1094-1101. doi:10.1002/qua.24917

264. Rupp M, Tkatchenko A, Müller KR, Von Lilienfeld OA. Fast and accurate modeling of molecular atomization energies with machine learning. *Phys Rev Lett*. 2012;108:058301. doi:10.1103/PhysRevLett.108.058301

265. Huo H, Rupp M. Unified Representation of Molecules and Crystals for Machine Learning. Published online 2017. doi:10.48550/arXiv.1704.06439

266. Sanchez JM, Ducastelle F, Gratias D. Generalized cluster description of multicomponent systems. *Phys Stat Mech Its Appl*. 1984;128(1-2):334-350. doi:10.1016/0378-4371(84)90096-7

267. Garcia-Hemme E, García G, Palacios P, et al. Vanadium supersaturated silicon system: a theoretical and experimental approach. *J Phys Appl Phys*. 2017;50(49):495101. doi:10.1088/1361-6463/aa9360

268. Luque A, Martí A, Antolín E, Tablero C. Intermediate bands versus levels in non-radiative recombination. *Phys B Condens Matter*. 2006;382(1-2):320-327. doi:10.1016/j.physb.2006.03.006

269. Pulko SH, Pearsall NM, Winckler J. “First-Generation” Model Of The Indium Tin Oxide-Indium Phosphide Solar Cell. In: *SPIE Proceedings Vol.1016: Optical Materials Technology for Energy Efficiency and Solar Energy Conversion VII*. SPIE; 1989:78-83. doi:10.1117/12.949916

270. Raj V, dos Santos TS, Rougieux F, et al. Indium phosphide based solar cell using ultra-thin ZnO as an electron selective layer. *J Phys Appl Phys*. 2018;51(39):395301. doi:10.1088/1361-6463/aad7e3

271. Jalali HB, Sadeghi S, Dogru Yuksel IB, Onal A, Nizamoglu S. Past, present and future of indium phosphide quantum dots. *Nano Res*. 2022;15(5):4468-4489. doi:10.1007/s12274-021-4038-z

272. Kato Y, Fujimoto S, Kozawa M, Fujiwara H. Maximum Efficiencies and Performance-Limiting Factors of Inorganic and Hybrid Perovskite Solar Cells. *Phys Rev Appl*. 2019;12(2):024039. doi:10.1103/PhysRevApplied.12.024039

273. Tanaka A. Toxicity of indium arsenide, gallium arsenide, and aluminium gallium arsenide. *Toxicol Appl Pharmacol*. 2004;198(3):405-411. doi:10.1016/j.taap.2003.10.019

274. Katz RN. High-Temperature Structural Ceramics. *Science*. 1980;208(4446):841-847. doi:10.1126/science.208.4446.841

275. Mo SD, Ouyang L, Ching WY, Tanaka I, Koyama Y, Riedel R. Interesting physical properties of the new spinel phase of Si_3N_4 and C_3N_4. *Phys Rev Lett*. 1999;83(24):5046-5049. doi:10.1103/PhysRevLett.83.5046

276. Zerr A, Miehe G, Serghiou G, et al. Synthesis of cubic silicon nitride. *Nature*. 1999;400:340-342. doi:10.1038/22493

277. Zerr A, Riedel R, Sekine T, Lowther JE, Ching WY, Tanaka I. Recent advances in new hard high-pressure nitrides. *Adv Mater*. 2006;18(22):2933-2948. doi:10.1002/adma.200501872

278. Boyko TD, Hunt A, Zerr A, Moewes A. Electronic structure of spinel-type nitride compounds Si_3N_4, Ge_3N_4, and Sn_3N_4 with tunable band gaps: Application to light emitting diodes. *Phys Rev Lett*. 2013;111(9):097402. doi:10.1103/PhysRevLett.111.097402

279. Molina B, Sansores LE. Electronic structure of Ge_3N_4 possible structures. *Int J Quantum Chem*. 2000;80(2):249-257. doi:10.1002/1097-461X(2000)80:2<249::AID-QUA19>3.0.CO;2-9

280. Bikowski A, Siol S, Gu J, et al. Design of Metastable Tin Titanium Nitride Semiconductor Alloys. *Chem Mater*. 2017;29(15):6511-6517. doi:10.1021/acs.chemmater.7b02122

281. Arca E, Lany S, Perkins JD, et al. Redox-Mediated Stabilization in Zinc Molybdenum Nitrides. *J Am Chem Soc*. 2018;140(12):4293-4301. doi:10.1021/jacs.7b12861

282. Gajdoš M, Hummer K, Kresse G, Furthmüller J, Bechstedt F. Linear optical properties in the projector-augmented wave methodology. *Phys Rev B - Condens Matter Mater Phys*. 2006;73(4):1-9. doi:10.1103/PhysRevB.73.045112

283. Salpeter EE, Bethe HA. A Relativistic Equation for Bound-State Problems. *Phys Rev*. 1951;84(6):1232-1242. doi:10.1103/PhysRev.84.1232

284. Krishna A, Krich JJ. Increasing efficiency in intermediate band solar cells with overlapping absorptions. *J Opt*. 2016;18(7):074010. doi:10.1088/2040-8978/18/7/074010

285. Lei L, Dong Q, Gundogdu K, So F. Metal Halide Perovskites for Laser Applications. *Adv Funct Mater*. 2021;31(16):2010144. doi:10.1002/adfm.202010144

286. Younis A, Lin C, Guan X, et al. Halide Perovskites: A New Era of Solution-Processed Electronics. *Adv Mater*. 2021;33(23):2005000. doi:10.1002/adma.202005000

287. Arandiyan H, S. Mofarah S, Sorrell CC, et al. Defect engineering of oxide perovskites for catalysis and energy storage: synthesis of chemistry and materials science. *Chem Soc Rev*. 2021;50(18):10116-10211. doi:10.1039/D0CS00639D

288. Jana A, Cho S, Patil SA, et al. Perovskite: Scintillators, direct detectors, and X-ray imagers. *Mater Today*. 2022;55:110-136. doi:10.1016/j.mattod.2022.04.009

289. Urbina A. The balance between efficiency, stability and environmental impacts in perovskite solar cells: a review. *J Phys Energy*. 2020;2(2):022001. doi:10.1088/2515-7655/ab5eee

290. Bakulin AA, Selig O, Bakker HJ, et al. Real-Time Observation of Organic Cation Reorientation in Methylammonium Lead Iodide Perovskites. *J Phys Chem Lett*. 2015;6(18):3663-3669. doi:10.1021/acs.jpclett.5b01555

291. Carignano MA, Kachmar A, Hutter J. Thermal effects on $CH_3NH_3PbI_3$ perovskite from Ab initio molecular dynamics simulations. *J Phys Chem C*. 2015;119(17):8991-8997. doi:10.1021/jp510568n

292. Mattoni A, Filippetti A, Saba MI, Delugas P. Methylammonium Rotational Dynamics in Lead Halide Perovskite by Classical Molecular Dynamics: The Role of Temperature. *J Phys Chem C*. 2015;119(30):17421-17428. doi:10.1021/acs.jpcc.5b04283

293. Mladenović M, Vukmirović N. Effects of thermal disorder on the electronic structure of halide perovskites: Insights from MD simulations. *Phys Chem Chem Phys*. 2018;20(40):25693-25700. doi:10.1039/c8cp03726d

294. Chen L, Wan L, Li X, et al. Inverted All-Inorganic $CsPbI_2Br$ Perovskite Solar Cells with Promoted Efficiency and Stability by Nickel Incorporation. *Chem Mater*. Published online 2019:2-9. doi:10.1021/acs.chemmater.9b03277

295. Zeng Z, Zhang J, Gan X, et al. In Situ Grain Boundary Functionalization for Stable and Efficient Inorganic $CsPbI_2Br$ Perovskite Solar Cells. *Adv Energy Mater*. 2018;8(25):1-8. doi:10.1002/aenm.201801050

296. Hu M, Chen M, Guo P, et al. Sub-1.4eV bandgap inorganic perovskite solar cells with long-term stability. *Nat Commun*. 2020;11(1):1-10. doi:10.1038/s41467-019-13908-6

297. Yang Z, Zhang X, Yang W, Eperon GE, Ginger DS. Tin–Lead Alloying for Efficient and Stable All-Inorganic Perovskite Solar Cells. *Chem Mater*. 2020;32(7):2782-2794. doi:10.1021/acs.chemmater.9b04265

298. Saliba M, Matsui T, Domanski K, et al. Incorporation of rubidium cations into perovskite solar cells improves photovoltaic performance. *Science*. 2016;354(6309):206-209. doi:10.1126/science.aah5557

299. Mitzi DB. Synthesis, Structure, and Properties of Organic-Inorganic Perovskites and Related Materials. In: Karlin KD, ed. *Progress in Inorganic Chemistry*. John Wiley & Sons, Inc.; 1999:1-121. doi:10.1002/9780470166499.ch1

300. Saliba M, Matsui T, Seo JY, et al. Cesium-containing triple cation perovskite solar cells: improved stability, reproducibility and high efficiency. *Energy Environ Sci*. 2016;9(6):1989-1997. doi:10.1039/C5EE03874J

301. Birch F. Finite elastic strain of cubic crystals. *Phys Rev*. 1947;71(11):809-824. doi:10.1103/PhysRev.71.809

302. Murnaghan FD. The Compressibility of Media under Extreme Pressures. *Proc Natl Acad Sci U S A*. 1944;30(9):244-247. doi:10.1073/pnas.30.9.244

303. Voigt W. *Lehrbuch der Kristallphysik (mit Ausschluss der Kristalloptik).* 1st ed. B.G.Teubner; 1910.

304. Reuss A. Berechnung der Fließgrenze von Mischkristallen auf Grund der Plastizitätsbedingung für Einkristalle . *ZAMM - Z Für Angew Math Mech*. 1929;9(1):49-58. doi:10.1002/zamm.19290090104

305. Hill R. The Elastic Behaviour of a Crystalline Aggregate. *Proc Phys Soc Sect A*. 1952;65:349-354. doi:10.1088/0370-1298/65/5/307

306. Patil JV, Mali SS, Hong CK. A-Site Rubidium Cation-Incorporated $CsPbI_2Br$ All-Inorganic Perovskite Solar Cells Exceeding 17% Efficiency. *Sol RRL*. 2020;4(7). doi:10.1002/solr.202000164

307. Khadka DB, Shirai Y, Yanagida M, Miyano K. Attenuating the defect activities with a rubidium additive for efficient and stable Sn-based halide perovskite solar cells. *J Mater Chem C*. 2020;8(7):2307-2313. doi:10.1039/c9tc06206h

308. Zhang W, Xiong J, Li J, Daoud WA. Guanidinium Passivation for Air-Stable Rubidium-Incorporated $Cs_{(1-x)}Rb_xPbI_2Br$ Inorganic Perovskite Solar Cells. *Sol RRL*. 2020;4(6). doi:10.1002/solr.202000112

309. Brivio F, Walker AB, Walsh A. Structural and electronic properties of hybrid perovskites for high-efficiency thin-film photovoltaics from first-principles. *APL Mater*. 2013;1(4):042111. doi:10.1063/1.4824147

310. da Silva EL, Skelton JM, Parker SC, Walsh A. Phase stability and transformations in the halide perovskite $CsSnI_3$. *Phys Rev B*. 2015;91(14):144107. doi:10.1103/PhysRevB.91.144107

311. Boross P, Dóra B, Kiss A, Simon F. A unified theory of spin-relaxation due to spin-orbit coupling in metals and semiconductors. *Sci Rep*. 2013;3:1-5. doi:10.1038/srep03233

312. Jong UG, Yu CJ, Kim YS, Kye YH, Kim CH. First-principles study on the material properties of the inorganic perovskite $Rb_{1-x}Cs_xPbI_3$ for solar cell applications. *Phys Rev B*. 2018;98(12):125116. doi:10.1103/PhysRevB.98.125116

313. He J, Liu J, Hou Y, Wang Y, Yang S, Yang HG. Surface chelation of cesium halide perovskite by dithiocarbamate for efficient and stable solar cells. *Nat Commun*. 2020;11(1):1-8. doi:10.1038/s41467-020-18015-5

314. Sanchez JM. Cluster expansion and the configurational theory of alloys. *Phys Rev B*. 2010;81(22):224202. doi:10.1103/PhysRevB.81.224202

315. Blum V, Zunger A. Mixed-basis cluster expansion for thermodynamics of bcc alloys. *Phys Rev B*. 2004;70(15):155108. doi:10.1103/PhysRevB.70.155108

316. Wu Q, He B, Song T, Gao J, Shi S. Cluster expansion method and its application in computational materials science. *Comput Mater Sci*. 2016;125:243-254. doi:10.1016/j.commatsci.2016.08.034

317. Xu X, Jiang H. Cluster expansion based configurational averaging approach to bandgaps of semiconductor alloys. *J Chem Phys*. 2019;150(3). doi:10.1063/1.5078399

318. Lundberg SM, Lee SI. A Unified Approach to Interpreting Model Predictions. In: *NIPS'17: Proceedings of the 31st International Conference on Neural Information Processing Systems*. Curran Associates Inc.; 2017:4768-4777.

319. Chang X, Fang J, Fan Y, et al. Printable $CsPbI_3$ Perovskite Solar Cells with PCE of 19% via an Additive Strategy. *Adv Mater*. 2020;32(40):1-8. doi:10.1002/adma.202001243

320. Duan J, Xu H, Sha WEI, et al. Inorganic perovskite solar cells: An emerging member of the photovoltaic community. *J Mater Chem A*. 2019;7(37):21036-21068. doi:10.1039/c9ta06674h

Appendix

In this appendix all the data, figures and even specific methodology published as supplementary material of the different articles here gathered are presented. Despite most of that information is not directly cited in the discussion of the results, it is considered necessary to fully understand the work conducted in the different publications, and it is referenced in those. Additionally, some figures from the supplementary material of articles nº 1 and 2 are explicitly commented during the analysis of this results in section 4.1.1, referring to band diagrams of compounds doped with transition metals that do not introduce the desired energetic levels to produce an IB scheme.

The order in which this supplementary material is presented is the one followed for the articles in chapter 3.

Supplementary material
First publication

nanomaterials

MDPI

Supplementary

Transition Metal-Hyperdoped InP Semiconductors as Efficient Solar Absorber Materials

Gregorio García [1,2,*], Pablo Sánchez-Palencia [1,2], Pablo Palacios [1,3] and Perla Wahnón [1,2]

[1] Instituto de Energía Solar, ETSI Telecomunicación, Universidad Politécnica de Madrid, Ciudad Universitaria, s/n, 28040 Madrid, Spain; p.sanchez-palencia@upm.es (P.S.-P.); pablo.palacios@upm.es (P.P.); perla@etsit.upm.es (P.W.)

[2] Departamento de Tecnología Fotónica y Bioingeniería, ETSI Telecomunicación, Universidad Politécnica de Madrid, Ciudad Universitaria, s/n, 28040 Madrid, Spain

[3] Departamento de Física aplicada a las Ingenierías Aeronáutica y Naval, ETSI Aeronáutica y del Espacio, Universidad Politécnica de Madrid, Pz. Cardenal Cisneros, 3, 28040 Madrid, Spain.

* Correspondence: ggmoreno@etsit.upm.es

Received: 14 January 2020; Accepted: 04 February 2020; Published: date

Table S1. Crystal Structure of TM (TM = Ti, V, Cr, Mn), In and P atoms.

Atom	Space Group	Unit cell parameters
In	123	$a = b = 3.25$ Å $c = 4.95$ Å $\alpha = \beta = \gamma = 90^{o}$
Ti	187	$a = b = 2.95$ Å $c = 4.69$ Å $\alpha = \beta = 90^{o}$ $\gamma = 120^{o}$
V	221	$a = b = c = 3.03$ Å $\alpha = \beta = \gamma = 90^{o}$
Cr	221	$a = b = c = 2.91$ Å $\alpha = \beta = \gamma = 90^{o}$
Mn	217	$a = b = c = 8.92$ Å $\alpha = \beta = \gamma = 90^{o}$
P	2	$a = 7.86$ Å $b = 5.50$ Å $c = 11.26$ Å $\alpha = 73.38^{o}$ $\beta = 90.53^{o}$ $\gamma = 71{,}62^{o}$

Experimental data take from: https://periodictable.com/Properties/A/CrystalStructure.an.wt.html.

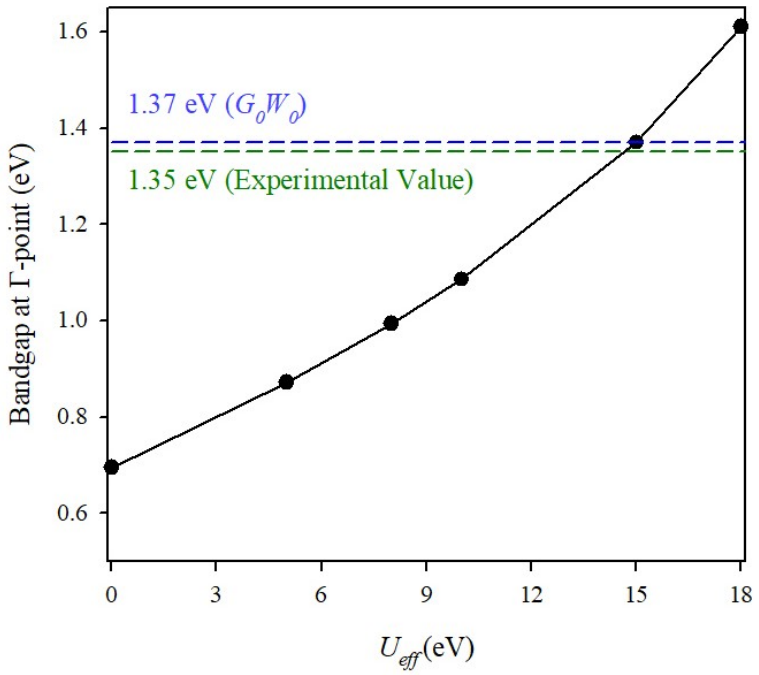


Figure S1. Calculated bandgap at Γ-point for InP by using PBE+*U* formalism (U_{eff} = 5, 8, 10, 15, 18 eV). Crystal structure optimizations were performed using the PBEsol. Blue and green dotted lines stand for G_0W_0 and experimental value.

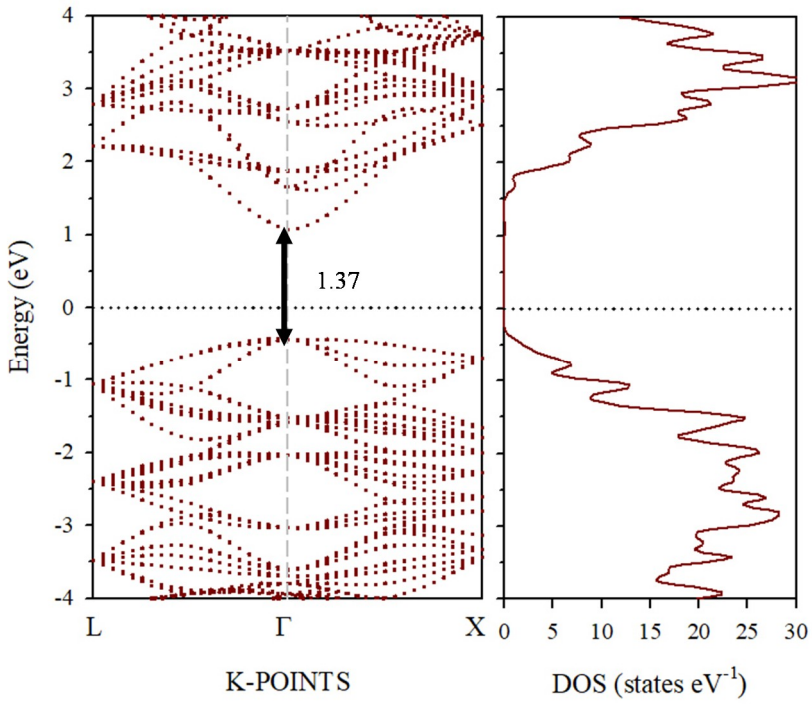


Figure S2. Electronic band structure (left) and Density of States (right) of InP calculated within G_0W_0 approach along to main energy differences at Γ-point. The zero energy has been set to the Fermi level (black dotted line). Spin-up and spin-down bands and DOS are not given separately as both contributions are the same for the native InP material.

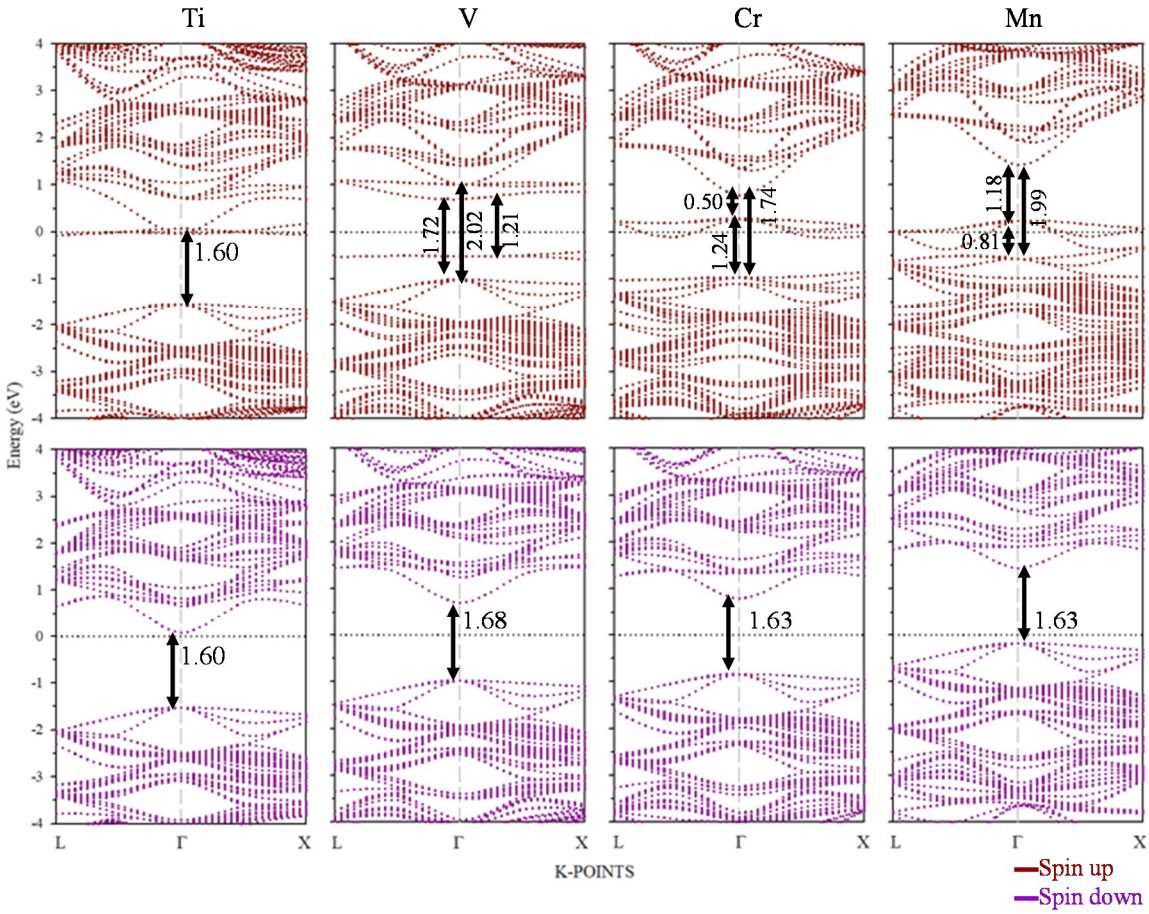


Figure S3. Electronic band structure of TM@InP (TM = Ti, V, Cr, Mn) calculated within G_0W_0 approach along to main energy differences at Γ-point. The zero of energy has been set at the Fermi level (black dotted line).

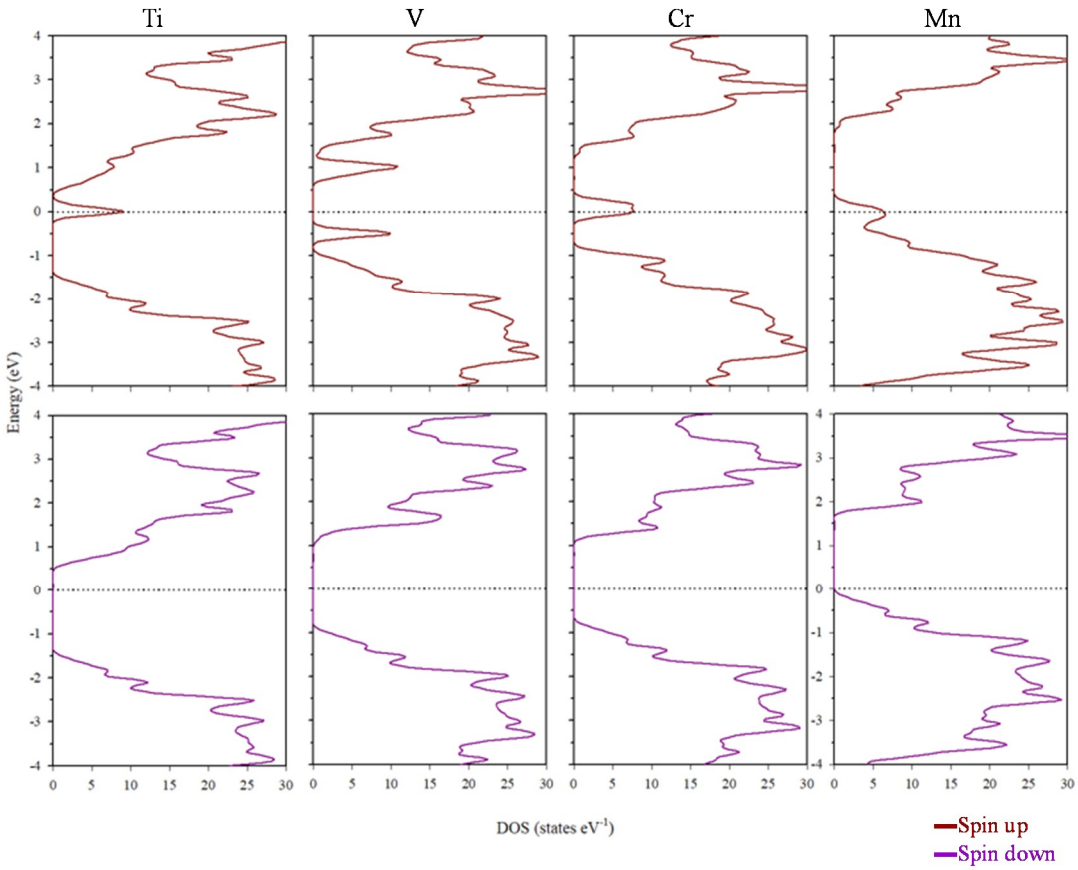


Figure S4. Density of States of TM@InP (TM = Ti, V, Cr, Mn) calculated within G_0W_0 approach. The zero of energy has been set at the Fermi level (black dotted line).

Supplementary material
Second publication

Spinel-Type Nitride Compounds with improved features as Solar Cell Absorbers

Pablo Sánchez-Palencia,[1,2] Gregorio García,[1,2*] José C. Conesa,[3] Perla Wahnón,[1,2] Pablo Palacios[1,4]

[1] Instituto de Energía Solar, ETSI Telecomunicación, Universidad Politécnica de Madrid, Ciudad Universitaria, s/n, 28040, Madrid, Spain

[2] Departamento de Tecnología Fotónica y Bioingeniería, ETSI Telecomunicación, Universidad Politécnica de Madrid, Ciudad Universitaria, s/n, 28040 Madrid, Spain

[3] Instituto de Catálisis y Petroleoquímica, Consejo Superior de Investigaciones Científicas, Marie Curie 2, 28049, Madrid, Spain

[4] Departamento de Física aplicada a las Ingenierías Aeronáutica y Naval. ETSI Aeronáutica y del Espacio, Universidad Politécnica de Madrid, Pz. Cardenal Cisneros, 3, 28040 Madrid, Spain.

* Corresponding author: ggmoreno@etsit.upm.es (G.G.)

Supplementary Material

Hardness Calculation

In general, the hardness is defined as the resistance of a solid to both elastic and plastic deformations. The hardness is a complex physical property not only governed by intrinsic factors (such as chemical composition and crystallographic structure), but also by extrinsic factors such as morphology, defects or crystalline size. Therefore, different processing parameters such temperature or pressure would lead to different hardness measurements. In this paper, we have focused on the concept of intrinsic hardness. In this paper, the intrinsic hardness (from now own, Hardness , H) calculation is based on the method firstly proposed by Šimůnek *et al.* [1], and later modified by Boyko *et al.* [2] to study ternary compounds with spinel structure. The hardness calculation proposed by Boyko *et al.* has shown to be successful for materials with spinel structure γ-$A_{(t)}B_{(o)2}N_4$, where $A_{(t)}$ and $B_{(o)}$ are the cations A and B having tetrahedral and octahedral coordination, respectively. The hardness is calculated from the bond strengths (S) of the tetrahedral and octahedral bonds (S_{AN} and S_{BN}):

$$H = \frac{32\eta}{a^3}\left(S_{A_{(t)}N}S^3_{B_{(o)}N}\right)^{\frac{1}{4}} exp(-\sigma f_e) \quad \text{(S1)}$$

where a is the lattice constant, while η ($\eta = 1550$) and σ ($\sigma = 4$) are scaling constants required to fit the hardness values for well-known materials. The bond strength is calculated from the bond lengths $d(A_{(t)}\text{-}N)$ and $d(B_{(o)}\text{-}N)$ and the average electron densities (e_i):

$$S_{A_{(t)}N} = \frac{\sqrt{e_{A_{(t)}} e_N}}{4d(A_{(t)}-N)} \quad \text{(S2a)}$$

$$S_{B_{(t)}N} = \frac{\sqrt{e_{B_{(o)}} e_N}}{6d(A_{(o)}-N)} \quad \text{(S2b)}$$

$$e_i = \frac{Z_i}{R_i} \qquad (i = A_{(t)}, B_{(o)} \text{ or } N \text{ atoms}) \quad \text{(S3)}$$

Average electron densities are calculated based on DFT calculations. Thus, the radius for a given atom *i* within a solid (R_i) is determined by choosing a sphere the radius R_i that contains the electronic valence charge (Z_i), *i.e.*, the radius of the sphere required to enclose the total valence charge. Note, that the bandgap and the electronic density should be calculated by using accurate DFT methods. Finally, the effective difference in the boding potentials (f_e) is defined as:

$$f_e = 1 - \left(\frac{\sqrt[7]{e_{A_{(t)}} e_{B_{(o)}}^2 e_N^4}}{e_{A_{(t)}} + 2e_{B_{(o)}} + 4e_N} \right)^2 \quad \text{(S4)}$$

As seen, information about the crystal structure and the electronic band structure are need for determining the hardness. Here, we have simplified the determination of e_i: Z_i is taken from the electronic configuration and R_i is defined as the atomic radius. This modification removes the need to perform accurate electronic structure calculations with a very dense k-point mesh. We are aware that this approach could lead to some errors in calculated hardness values. It should be mentioned that our aim is not accurately calculating hardness values but assessing the likelihood of a specific material to be synthetized as well as its stability, which offer an interesting tool to study both the hardness and the existence of hypothetical materials. Table S3 and Fig. S1 display calculated hardness values according with our modified approach for several spinel nitrides along to previously published results. Our results are, in general, in good accordance with previous ones [1, 2] and experimental data.[3, 4] Our approach accurately predicts hardness trends. Compared to Boyko *et al.* values,[2] hardness of compounds with Ge, Sn and Pb are in a reasonable agreement, while, the largest differences are obtained for those compounds with C and Si atoms. In our manuscript we are dealing with spinel nitrides compounds with Ge and Sn, *i.e.,* with a chemical composition between γ-Ge_3N_4 and γ-Sn_3N_4. Therefore, it would be plausible to apply this approach to the compounds studied in our manuscript to get a qualitative prediction of their hardness.

Although the methodology proposed by Boyko *et al.* is adequate to treat compounds with tetrahedral and octahedral coordination, it cannot be applied when the same position is occupied for two kinds of atoms (*e.g.,* in γ-$(SnGe)_3N_4$ octahedral positions are occupied by Sn and Ge). We have also tailored this approach to treat the ternary compounds with spinel structure here studied. For γ-$(Sn_{0.5}Ge_{0.5})_3N_4$ and γ-$(M_mSn_{0.5-m}Ge_{0.5})_3N_4$ compounds, tetrahedral positions are only occupied by Sn atoms, while octahedral positions are occupied by Sn, Ge (and M atoms for hyperdoped compounds).

Thus, the bond strength for octahedral bonds ($S_{B(o)N}$) and the average electronic density for octahedral positions ($e_{B(o)}$) are redefined considering the contributions of each atom that occupies an octahedral position:

$$S_{B_{(o)}N} = \frac{1}{2}\left[mS_{M_{(o)}N} + (x-m)S_{Sn_{(o)}N} + (2-x)S_{Ge_{(o)}N}\right] \quad \text{(S5)}$$

$$e_{B_{(o)}} = \frac{1}{2}\left[me_{M_{(o)}} + (x-m)e_{Sn_{(o)}} + (2-x)e_{Ge_o}\right] \quad \text{(S6)}$$

where for each atom with octahedral coordination (Ge, Sn and M), bond strength for octahedral bonds ($S_{B(o)N}$) and the average electronic density are calculated according to equations S2b and S3, respectively.

Electronic band structure of γ-($M_mSn_{0.5-m}Ge_{0.5}$)$_3N_4$ (M = Sc, Ti, Mn, Ni, Nb) spinels with a single gap.

This family includes those compounds with a single gap due to VB - CB energy difference for those bands belonging to the host semiconductor transitions . Except for M = Mn, these spinels yields a bandgap ~ 2.0 eV (E_g for the host material). Rigorously speaking, these spinels own a nearly direct bandgap at Γ-point, while the indirect bandgap is measured at M-Γ points (see Table 6S) due to non-degenerated energies of the highest valence bands at Γ and M points upon the hyperdoping with M. Since the differences between direct and indirect bands are ≤ 0.15 eV, from now on will be focused on the nearly direct bandgap at Γ (this is also noted for most cases with a single gap electronic band structure). In general, for spin-down channel, these hyperdoped-spinels own a similar band structure patter with a bandgap at Γ-point ~ 2.0. In addition, similar conclusions are obtained for both m concentrations here studied.

Starting from the electronic shell configuration of Sn (*Z*: $5s^25p^2$) and Sc (*Z:* $3d^14s^2$) or Ti (*Z:* $3d^24s^2$), M *d*-states are empty and located within the conduction band at high energies (see Figures S3 and S4). Thus, the bandgap (measured as VB → CB energy difference) is mainly due to the band edges of the host spinel. For substitution of Sn by Sc leads to a hole-doped system, where the Fermi level is shifted within the valence band. For substitutional doping with Ti, the main contribution from transition metal atom to the electronic band structure is found at energy somewhat higher than the CBM.

For Mn (*Z:* $3d^54s^2$) at low concentrations (m = 0.042), the t_{2g} triplet for spin up component is filled due to the extra electrons respect to Sn, while e_g doublet is empty (see Figure S7). Low energy triplet / high energy doublet appears highly hybridized with the valence / conduction band states belonging to the host material. In consequence a E_g = 2.26 eV is measured at Γ-point. For spin-down channel, Mn-hyperdoped spinel yields a similar band structure with a bandgap opened to 2.28 eV, where *d*-orbitals are mixed with the CB. At higher concentrations (m = 0.083), there is a larger

splitting between filled t_{2g} and empty e_g states, which leads to a bandgap of 3.31 eV for spin-up channel (3.37 eV for spin-down).

Ni (*Z:* $3d^8 4s^2$) coordination leads to a spin-low configuration, where the six extra electrons are located at the t_{2g} manifold (see Figure S10). Note that as we move from left to the right along the 3*d* row, we are approaching to the heavier 3*d* metals, whose atomic 3d levels are deeper in energy. Thus, the interaction between heavier transition metals and N would become stronger. In fact, this low-spin configuration is due to a high energy split (~3.5 eV) between filled t_{2g} and empty e_g states. As results, t_{2g} states appear highly hybridized with deep valence bands (~1.5 eV below the VBM), while the lowest energy conduction bands are mainly due to the e_g doublet. In short, Ni-hyperdoped spinels yield a semiconductor electronic-band structure with a bandgap $E_g \simeq 2.31$ / 2.24 eV for spin up/down due to valence and conduction band edges of the host spinel.

For M = Nb (*Z:* $4d^4 5s^1$) the E_{Fermi} penetrates in the lowest conduction bands, which are mainly due to Nb-t_{2g} orbitals (see Figure S13). Even though, the largest contribution to the CBM comes from $Sn_{(o)}$, $Ge_{(o)}$ and N atoms. The only one electron of Nb is located at one of the three t_{2g} states for spin up. Although average d($Nb_{(o)}$-N) = 2.12 Å, there is a small compression of the octahedron along its longitudinal *z*-axis, which splits the three fold t_{2g} level into the occupied one (d_{xy} orbital, which is below the Fermi level), while d_{xz} and d_{yz} orbitals are empty (above the Fermi level). This compression leas to a small energy difference (~ 0.43 eV) between occupied and empty t_{2g} states. The e_g doublet appear at much higher energies highly mixed with the CB.

Electronic band structure of γ-$(M_mSn_{0.5-m}Ge_{0.5})_3N_4$ (M = V, Fe, Zn, Mo) spinels with a *pseudo*-in-gap-band.

In this paper, a *pseudo*-in-gap-band (*pseudo*-IGB) has been defined as a band located inside the gap of the host semiconductor, which meets some requirements to be defined as an IGB: *i*) have its own small dispersion, without being at a discrete level; ii) be well isolated from the band edges. However, this pseudo-IGB is not partially filled. In addition to VB → CB transitions belonging to the host material, these semiconductors would only allow an extra sub-bandgap VB → *pseudo*-IGB or *pseudo*-IGB → CB transition for filled or empty *pseudo*-IGB, respectively.

As described for Nb-hyperdoped spinel, V-hyperdoped (*Z*: $3d^3 4s^2$) one also yields a small compression of the octahedral around the transition metal along the longitudinal *z*-axis, which leads to non-degenerated t_{2g} triplet (see Figure S5). For spin-up component, the low-energy d_{xy} orbital is occupied with one electron, while d_{xz} and d_{yz} ones are empty. For m = 0.042, occupied d_{xy} level is located at 0.54 eV below the E_{Fermi}, as well as this level is well differentiated from the remaining valence band states belonging to the host spinel. Hence, this level is classified as a *pseudo*-IGB. The

lowest-energy conduction bands are mainly due to empty d_{xz} and d_{yz} states. Though the VB-CB energy differences for those bands belonging to the host material reach a value of 2.39 eV, the bandgap of V-hyperdoped spinels is notably smaller (0.91 eV), which corresponds to the energy split between the pseudo-IGB and empty d_{xz} and d_{yz} states. For spin-down channel, V-hyperdoped spinel yields a semiconductor electronic band structure with a (nearly) direct bandgap at Γ-point, which is opened to 2.30 eV. Similar conclusions can be drawn with respect to the effect of V-concentrations. Higher m concentration (m = 0.083) leads to the double of t_{2g} states (three for each atoms) which follow the same behavior above described. However, the wider dispersion for occupied one and empty t_{2g} states leads to a bandgap < 0.01 eV.

As we move from left to the right along the 3*d* row, Fe (*Z*: $3d^3 4s^2$) is the first atom for which two (high- or low-) spin configurations would be possible (it also occurs for M = Co, Ni, Cu). Our results point out that M-hyperdoping (M = Fe, Co, Ni, Cu) always leads to a low-spin configuration for M-hyperdoped spinels. This preference is related with strong crystal coordination fields around M. Electronic band structure of Fe-hyperdoped spinels for spin-up component is characterized by a direct bandgap E_g = 2.32 eV (2.35 eV) for m = 0.042 (m = 0.083) at Γ-point (see Figure S8). The low-energy t_{2g} triplet is fully occupied with three electrons. As seen in Fig. S8 and 5, this level is highly hybridized with depth valence bands. Low-energy t_{2g} triplet is observed ~ 0.31 eV below the VBM (~ 2.17 eV below the E_{Fermi}). In addition, ~ 0.7 eV above the CBM (~ 1.30 eV above the E_{Fermi}), two levels (4 four levels for m = 0.083) are found due to the e_g states. Thus, the crystal-field splitting energy separating the t_{2g} and e_g states is estimated to be approximately 3.47 eV. For spin-down channel, a filled *pseudo*-IGB is formed due to one non-degenerate t_{2g} orbital occupied by one electron, while the CBM is dominated by the remaining t_{2g} orbitals. Anew, the octahedral environment around M is level distorted (there is a small compression along the longitudinal axis), which leads to a split the t_{2g} manifold. Though the VB-CB energy difference for those bands belonging to the host material reaches a value of 2.32 eV for m = 0.042 (2.41 eV for m = 0.083), the bandgap of Fe-hyperdoped spinels is notably smaller, E_g = 1.05 eV (0.49 eV) , which corresponds to the energy split between the *pseudo*-IGB and empty d_{xz} and d_{xz} states.

Zn-hyperdoped spinels (*Z*: $3d^{10} 4s^2$) yield a low-spin configuration, where Zn *3d* (both t_{2g} and e_g manifolds) levels for spin up are filled (5 electrons), while the remaining 3 extra electrons are located at the low-energy t_{2g} triplet for spin-down component (see Figure S12). Instead of M concentration, the electronic band structure for spin-up yield a bandgap $E_g \simeq$ 1.96 eV. The VBM is dominated by e_g electrons of the Zn *3d* orbitals, while t_{2g} states appears highly mixed with lower valence bands. For spin-down component, an empty *pseudo*-IGB is formed in the bandgap region, which is dominated by empty e_g doublet. At Γ-point, the *pseudo*-IGB is located 0.99 eV / 2.43 eV over / below the VBM / CMB which leads to VB-CB energy difference of 3.42 eV for the host spinel

(for m = 0.042). Because of t_{2g} levels appears at much lower energy within the valence band, the bandgap of the system (0.99 eV at Γ-point) does not match with the energy splitting between t_{2g} triplet and e_g doublet. Due to the curvature of the *pseudo*-IGB, the lowest bandgap energy (0.37 eV) is located at M-point. For the highest M concentration (m = 0.083), larger dispersion of the *pseudo* - IGB (now it is formed by 4 states) reduces the bandgap up to 0.74 eV at Γ-point (0.17 at M-point).

For spin-down channel, Mo-hyperdoped (Z: $4d^5 5s^1$) spinel yields an electronic band structure with a bandgap of 2.13 eV for m = 0.042 (2.17 eV for m = 0.083) at Γ-point, which is due to VB-CB energy differences belonging to the host spinel (see Figure S14). Mo *3d* levels are empty and located within the CB. At Γ-point, the low-energy t_{2g} triplet appears ~ 0.75 eV above the CBM. For spin-up channel, the low-energy t_{2g} triplet is occupied with the two extra electrons. However, the octahedral void around Mo atom is slightly compressed along the *z*-axis, which splits the degeneration. Hence, the low-energy d_{xy} orbital is occupied with one electron, while d_{xz} and d_{yz} ones are semi-filled with the other one extra electron. The low energy d_{xy} is located between the VBM (with an energy difference of 1.27 eV for m = 0.042 at Γ-point) and the CBM (0.84 eV at Γ-point). This state can be defined as a filled *pseudo*-IGB. Thus, for m = 0.042, the bandgap of the host semiconductor is opened up to 2.11 eV. Semi-filled d_{xz} and d_{yz} states are located at the E_{Fermi} energy as well as they define the CBM. Therefore, the bandgap of Mo-hyperdoped spinel at the lowest M concentration is 0.99 eV. This system could be also defined as IGB-material, where the IGB is due to semi-filled d_{xz} and d_{xz}, which are not well differentiated from the conduction bands. At higher M concentration (m = 0.083), the dispersion of t_{2g} levels leads to a no gap between these states.

Decomposed absorption coefficient of M-hyperdoped spinels.

For the host spinel material, the AUC = $1.87 \cdot 10^4$ $cm^{-1} \cdot eV$, which corresponds to the electron transitions from the VB to the CB. For M = Cr, the AUC keeps unchanged respect the host material. For Cr-hyperdoped, the AUC for VB → IGB / IGB → CB / VB →CB transitions entail 9.95 / 10.65 / 79.46 % of the total AUC. As seen in Fig. 9 the absorption coefficient considerably decreases over 2.0 eV. Then, although there is loss of the photo-absorption of the host, this is compensated due to new transitions across the IGB. Partial contribution caused by electron transitions from VB to IGB present two main peaks. This curve reaches the highest intensity at ~ 1.00 eV, which agrees with energy differences between the VB and IGB measured in Fig. 7 at Γ-point. The other peak at ~ 0.50 – 0.60 eV is due to electronic transitions between the highest occupied valence band and the IGB, whose energy difference is equal to 0.59 eV at Γ-point. The absorption curve due to VB → CB transitions is characterized by two peaks at ~ 1.80 and 2.20 eV. The former has been assigned to electronic transitions between the highest valence band and the CB belonging to host material (the

energy difference for this transition is equal to 1.76 eV at Γ-point), while the latter is due to the bandgap of the host material (2.18 eV at Γ-point for both spin-up and spin-down components).

For M = Co, the *AUC* due to VB → CB transitions ($1.89 \cdot 10^4$ $cm^{-1} \cdot eV$) is comparable to the total *AUC* of the host material. Even though, the *AUC* for VB → IGB / IGB → CB ($3.76 \cdot 10^3$ $cm^{-1} \cdot eV$ and $2.60 \cdot 10^3$ $cm^{-1} \cdot eV$, respectively) considerable increases the total value up to $AUC = 2.52 \cdot 10^4$ $cm^{-1} \cdot eV$. Hence, VB → IGB / IGB → CB / VB →CB transitions represent 14.86 / 10.28 / 74.70 % of the total photo-absorption. For VB → IGB, it is noticed that there are two main contributions at ~ 0.70 eV and 1.60 eV. Lower energy peak is due to the electronic transitions between the highest valence band (which is due to Co-*3d* levels, see Fig. 5 and 7) and the IGB, while the latter peak is due to electronic transitions between deep valence bands and the IGB. Partial contribution due to IGB → CB transitions reaches the highest intensity at ~ 1.25, which matches the energy difference between these states (Fig. 7). Finally, the absorption edge considerably increases from ~ 2.0 eV due to VB → CB transitions, which are related to the energy differences of 2.15 eV (spin-up) and 1.97 eV (spin-down) between band edges at Γ-point (Fig. 7).

Substitutional hyperdoping with M = Cu provides the best improvement of the gained photo-absorption ($AUC = 3.01 \cdot 10^4$ $cm^{-1} \cdot eV$). VB → IGB / IGB → CB / VB →CB contributions stand for 10.37 / 9.67 / 80.01 % to the total absorption. On this occasion, the gained photo-absorption is also due to VB → CB. As seen in Fig. 10, *AUC* for VB → CB increases up to $2.41 \cdot 10^4$ $cm^{-1} \cdot eV$. As seen in Fig. 9, the absorption curve defining VB → CB transitions considerable increases from ~ 1.75 eV. This broad absorption peak is due to the sum of several (gaussian) peaks centered at ~ 1.7, 2.0 and 2.3 eV, which agree with energy differences between VB and the lowest CB (mainly defined empty Cu-*3d* levels) for spin-down, bandgap of the host material for spin-down and bandgap of the host for spin-up, respectively measured at Γ-point (see Fig. 7). Respect to VB → IGB and IGB → CB partial contributions, their maximums are obtained at ~ 1.0 and 1.3 eV, which agree with energy differences shown in Fig. 7.

Table S1. Lattice parameters (*a*) and bond distances (*d*) obtained for optimized crystal structure of γ-$(Sn_xGe_{1-x})_3N_4$ (x = 0.0, 0.5, 1.0). For more details, see Fig. 1. Units are in Angstroms (Å).

	γ-Ge_3N_4 [a]	γ-Ge_3N_4	γ-Sn_3N_4 [b]	γ-Sn_3N_4	γ-$(Sn_{0.5}Ge_{0.5})_3N_4$
a	8.212	8.301	9.037	9.085	8.738
d($Ge_{(t)}$-N)	1.88	1.92			
d($Ge_{(o)}$-N)	1.99	2.01			2.04
d($Sn_{(t)}$-N)			2.11	2.11	2.09
d($Sn_{(o)}$-N)			2.17	2.19	2.09

[a] Experimental data taken from reference [5].

[b] Experimental data taken from reference [6].

Table S2. Lattice parameters (*a*) and average bond distances (*d*) obtained for optimized crystal structure of γ-$(M_mSn_{0.5-m}Ge_{0.5})_3N_4$ (m = 0.042, 0.083). For more details, see Fig. 1. Units are in Angstroms (Å).

	Sc	Ti	V	Cr	Mn	Fe	Co	Ni	Cu	Zn	Nb	Mo
	m = 0.042											
a	8.708	8.693	8.687	8.681	8.678	8.675	8.673	8.674	8.686	8.696	8.716	8.708
d($Ge_{(o)}$-N)	2.02	2.02	2.02	2.02	2.02	2.02	2.02	2.02	2.02	2.01	2.02	2.02
d($Sn_{(t)}$-N)	2.18	2.17	2.17	2.17	2.17	2.17	2.17	2.17	2.17	2.17	2.18	2.18
d($Sn_{(o)}$-N)	2.06	2.07	2.08	2.08	2.08	2.07	2.07	2.07	2.08	2.08	2.08	2.08
d($M_{(o)}$-N)	2.19	2.09	2.05	2.02	2.01	2.00	2.00	2.01	2.08	2.14	2.12	2.10
	m = 0.083											
a	8.704	8.671	8.659	8.649	8.640	8.634	8.630	8.632	8.656	8.678	8.711	8.699
d($Ge_{(o)}$-N)	2.01	2.02	2.02	2.02	2.01	2.01	2.01	2.01	2.01	2.00	2.02	2.02
d($Sn_{(t)}$-N)	2.18	2.17	2.17	2.17	2.16	2.16	2.16	2.16	2.17	2.17	2.18	2.17
d($Sn_{(o)}$-N)	2.07	2.07	2.07	2.07	2.07	2.07	2.07	2.06	2.07	2.07	2.07	2.08
d($M_{(o)}$-N)	2.19	2.09	2.04	2.01	2.00	1.99	1.99	2.00	2.07	2.14	2.12	2.09

Table S3. Crystal structures of Ge, Sn and M (M = Sc, Ti, V, Cr, Mn, Fe, Co, Ni, Cu, Zn, Nb, Mo) atoms and N_2 molecule.

		Unit cell parameters	
Atom	Space Group	Experimental [a]	DFT [b]
Ge	225	*a* = *b* = *c* = 5.66 Å	*a* = *b* = *c* = 5.58 Å
Sn	141	*a* = *b* = 5.83 Å *c* = 3.18 Å	*a* = *b* = 5.92 Å *c* = 3.28 Å
Sc	194	*a* = *b* = 3.30 Å *c* = 5.27 Å	*a* = *b* = 3.29Å *c* = 5.21 Å
Ti	194	*a* = *b* = 2.95 Å *c* = 4.69 Å	*a* = *b* = 2.91 Å *c* = 4.65 Å
V	229	*a* = *b* = *c* = 3.03 Å	*a* = *b* = *c* = 2.98 Å
Cr	229	*a* = *b* = *c* = 2.91 Å	*a* = *b* = *c* = 2.88 Å
Mn	217	*a* = *b* = *c* = 8.91 Å	*a* = *b* = *c* = 8.82 Å
Fe	229	*a* = *b* = *c* = 2.87 Å	*a* = *b* = *c* = 2.75 Å
Co	194	*a* = *b* = 2.50 Å *c* = 4.07 Å	*a* = *b* = 2.46 Å *c* = 3.92 Å
Ni	225	*a* = *b* = *c* = 3.52 Å	*a* = *b* = *c* = 3.49 Å
Cu	225	*a* = *b* = *c* = 3.61 Å	*a* = *b* = *c* = 3.61 Å
Zn	194	*a* = *b* = 2.66 Å *c* = 4.95 Å	*a* = *b* = 2.65Å *c* = 4.89 Å
Nb	229	*a* = *b* = *c* = 3.30 Å	*a* = *b* = *c* = 3.29 Å
Mo	229	*a* = *b* = *c* = 3.14 Å	*a* = *b* = *c* = 3.12 Å
N [c]			

[a] Experimental data taken from https://periodic table.com/Properties/A/CrystalStructure.an.wt.html

[b] DFT optimized unit cell parameters here obtained with PBE functional

[c] For N atom, N_2 molecule is gas phase was optimized providing a *d(N-N)* = 1.09 Å

Table S4. Calculated Hardness values (*H*) along to several structure parameters for spinel nitrides γ-$A_{(t)}B_{(o)2}N_4$.

	Experimental	Šimůnek *et al.* [c]	Boyko *et al.* [d]	This work	
	H (GPa)	*H (GPa)*	*H (GPa)*	*a* (Å) [e]	*H (GPa)* [f]
γ-C_3N_4		70.1	76.9	6.730	126.94
γ-SiC_2N_4			58.5	7.182	87.22
γ-CSi_2N_4			42.9	7.384	58.74
γ-Si_3N_4	35-37 [a]	27.4	33.3	7.349	50.89
γ-$GeSi_2N_4$			31.1	7.915	38.62
γ-$SiGe_2N_4$			26.5	8.115	30.56
γ-Ge_3N_4	28-31 [b]	19.1	24.9	8.301	26.60
γ-$SnGe_2N_4$			19.9	8.576	19.36
γ-$GeSn_2N_4$			16.3	8.827	17.79
γ-Sn_3N_4	13 [b]		13.8	9.085	15.40
γ-$PbSn_2N_4$			13.2	9.268	13.83
γ-$SnPb_2N_4$			11.3	9.444	11.60
γ-Pb_3N_4			10.5	9.634	10.42

[a] Taken from reference [3] and [7].

[b] Taken from reference [4].

[c] Taken from reference [1].

[d] Taken from references [1, 2].

[e] Calculated by using crystal structure parameter here optimized at PBE level (see section 2).

[f] Atomic radii taken from reference [8].

Table S5. Calculated enthalpies (ΔH_f) and hardness values (*H*) for optimized crystal structure of γ-$(Sn_{x-m}Ge_{1-x})_3N_4$ (x = 0.0, 0.5, 1.0) and γ-$(M_mSn_{0.5-m}Ge_{0.5})_3N_4$.

	ΔH (eV/unit cell) [a]		*H (GPa)*	
p-Ge_3N_4	-16.56			
γ-Ge_3N_4	-12.35		26.60	
γ-Sn_3N_4	9.07		15.46	
γ-$(Sn_{0.5}Ge_{0.5})_3N_4$	-2.28 / -0.35 /1.46		20.98	
γ- $(M_mSn_{x-m}Ge_{1-x})_3N_4$	m = 0.042	m = 0.083	m = 0.042	m = 0.083
Sc	-9.04	-3.22	21.00	20.92
Ti	-1.67	-4.56	21.25	21.44
V	0.16	0.58	21.46	21.92
Cr	1.60	1.64	20.92	20.81
Mn	2.04	2.49	21.10	21.23
Fe	1.87	2.20	21.33	21.66
Co	1.96	2.47	21.50	22.00
Ni	2.15	2.91	21.64	22.30
Cu	4.02	6.73	20.88	20.81
Zn	3.65	6.04	21.02	21.00
Nb	-0.06	-1.44	21.21	21.41
Mo	1.96	2.32	20.73	20.39

[a] For p- Ge_3N_4, calculated value is multiplied by 4 because its unit cell contains 14 atoms; for p- Ge_3N_4, γ-Ge_3N_4 and γ-Sn_3N_4 only $\Delta H_{f,elements}$ are collected; for γ-$(Sn_{0.5}Ge_{0.5})_3N_4$, values correspond to $\Delta H_{f,elements}$ / $\Delta H_{f,spinel\text{-}spinel}$ / $\Delta H_{f,phenacite\text{-}spinel}$; for γ- $(M_mSn_{x-m}Ge_{1-x})_3N_4$ collected values stand for ΔH_s

Table S6. Bandgap values (E_g) and effective masses for holes and electrons (m^+ and m^-) for γ-$(Sn_xGe_{1-x})_3N_4$ (x = 0.0, 0.5, 1.0).

	E_g (eV) [a,b]	E_g (eV) [c]	m^+/m_0 [d]	m^-/m_0 [d]
γ-Ge_3N_4	3.17 (~ 3.50)	1.94	0.24 / 0.30 / 0.05 / 0.10	0.30 / 0.15 / 0.24 / 0.21
γ-Sn_3N_4	1.38 (1.15- 1.55)	0.39	0.73 / 1.00 / 2.34 / 1.08	0.14 / 0.09 / 0.10 / 0.11
γ-$(Sn_{0.5}Ge_{0.5})_3N_4$	2.00	0.89	0.41 / 0.93 / 1.75 / 0.73	0.15 / 0.09 / 0.10 / 0.11

[a] E_g calculated with sc-GcW_0 approach

[b] Experimental bandgap values are given in parenthesis. Taken from references [9, 10]

[c] E_g calculated with PBE functional

[d] Effective masses were calculated by parabolic fitting of the edge bands. Values correspond to effective mass along Γ-R / Γ-M / Γ-X directions and total effective mass.

Table S7. Bandgap values (E_g) for γ-$(M_mSn_{0.5-m}Ge_{0.5})_3N_4$ measured at Γ-point.

	m = 0.042				m = 0.083			
	Spin-Up		Spin-Down		Spin-Up		Spin-Down	
	E_g (eV) [a]	E_g (eV) [b]	E_g (eV) [a]	E_g (eV) [b]	E_g (eV) [a]	E_g (eV) [b]	E_g (eV) [a]	E_g (eV) [b]
Sc	1.97 (1.85) [c]	1.11 (1.03) [c]	1.97 (2.01) [c]	1.11 (1.04) [c]	1.97 (2.01) [c]	1.28 (1.12) [c]	2.01 (1.90) [c]	1.24 (1.12) [c]
Ti	2.29 (2.15) [c]	1.16 (1.09) [c]	2.35 (2.25) [c]	1.22 (1.12) [c]	2.35 (2.25) [c]	1.28 (1.22) [c]	2.41 (2.26) [c]	1.24 (1.16) [c]
V	0.91	0.38	2.30 (2.21) [c]	1.16	2.30 (2.21) [c]	-	2.31 (2.16) [c]	1.28 (1.22) [c]
Cr	0.59 /1.17 /1.76 [d]	0.43 / 0.75 / 1.18 [d]	2.18 (2.15) [c]	1.13 (1.16) [c]	2.18 (2.15) [c]	-	3.31 (3.18) [c]	1.29 (1.23) [c]
Mn	2.26 (2.19) [c]	1.20 (1.13) [c]	2.28 (2.24) [c]	1.16 (1.11) [c]	2.28 (2.24) [c]	0.58 (0.46) [c]	3.37 (3.26) [c]	1.23 (1.13) [c]
Fe	2.32 (2.18) [c]	1.13	1.05	0.54	1.05	1.31 (1.28) [c]	0.49	0.22
Co	2.15 (2.09) [c]	1.03 (1.15) [c]	0.71 /1.26 / 1.97 [d]	0.42 / 0.80 / 1.22 [d]	0.71 /1.26 / 1.97 [d]	1.32 (1.28) [c]	1.18	0.82
Ni	2.31 (2.17) [c]	1.19 (1.13) [c]	2.24 (2.16) [c]	1.00	2.24 (2.16) [c]	1.28 (1.26) [c]	2.36 (2.26) [c]	1.28 (1.26) [c]
Cu	1.13 / 1.30 / 2.43 [d]	0.83 / 0.32 / 1.15 [d]	1.69 (1.61) [c]	1.11 (1.04) [c]	1.01 / 1.20/ 2.21 [d]	0.77 / 0.50 / 1.27 [d]	1.68 (1.34) [c]	1.02 (0.66) [e]
Zn	1.94 (1.90) [c]	0.88	0.99 (0.37) [e]	0.66 (< 0.01) [e]	0.99 (0.37) [e]	0.95	0.74 (0.17) [e]	0.46 (< 0.01) [e]
Nb	1.99 (1.86) [c]	1.06	1.94 (1.89) [c]	1.06	1.94 (1.89) [c]	1.12 (1.09) [c]	2.02 (2.13) [c]	1.25 (1.15) [c]
Mo	0.88	0.75	2.13 (2.11) [c]	1.15 (1.09) [c]	2.13 (2.11) [c]	-	2.17 (2.01) [c]	1.18 (1.13) [c]

[a] E_g calculated with sc-GW_0 approach

[b] E_g calculated with PBE functional

[c] Reported value corresponds to a nearly direct bandgap at Γ point. Value in parenthesis stands for an indirect bandgap, in which the CBM and VBM are located at the Γ and M points, respectively.

[d] Three gaps are defined due to the presence of an IGB measured at Γ-point: VB-IGB / IGB-CB / VB-CB.

[e] Gap measured at Γ point. The lowest bandgap energy (due to the curvature of transition metal states) is given in parenthesis.

Table S8. Area under the curve (*AUC*) for the absorption coefficients of γ-$(Sn_{0.5}Ge_{0.5})_3N_4$ and γ-$(M_mSn_{0.5-m}Ge_{0.5})_3N_4$ (m =0.042; M = Cr, Co, Cu) obtained between 0.5 eV and 2.5 eV. Units are $cm^{-1}\cdot eV$.

	AUC	VB → IGB	IGB → CB	VB → CB	TOTAL [a]
γ-$(Sn_{0.5}Ge_{0.5})_3N_4$	1.87×10^4				
γ-$(M_mSn_{0.5-m}Ge_{0.5})_3N_4$					
Cr	1.87×10^4	1.84×10^3	1.97×10^3	1.47×10^4	1.85×10^4
Co	2.52×10^4	3.76×10^3	2.60×10^3	1.89×10^4	2.53×10^4
Cu	3.01×10^4	3.12×10^3	2.91×10^3	2.41×10^4	3.01×10^4

[a] Defined as the sum of the AUC for VB →IGB, IGB → CB and VB → CB transitions.

Table S9. Detailed-balance maximum Photovoltaic Efficiency (% η) for γ-$(Sn_{0.5}Ge_{0.5})_3N_4$ and γ-$(M_mSn_{0.5-m}Ge_{0.5})_3N_4$ (m =0.042; M = Cr, Co, Cu).

	% η	
	Non-overlapping Absorptions	Overlapping-Absorptions
γ-$(Sn_{0.5}Ge_{0.5})_3N_4$	25	
γ-$(M_mSn_{0.5-m}Ge_{0.5})_3N_4$		
Cr	35	45
Co	55	57
Cu	35	42

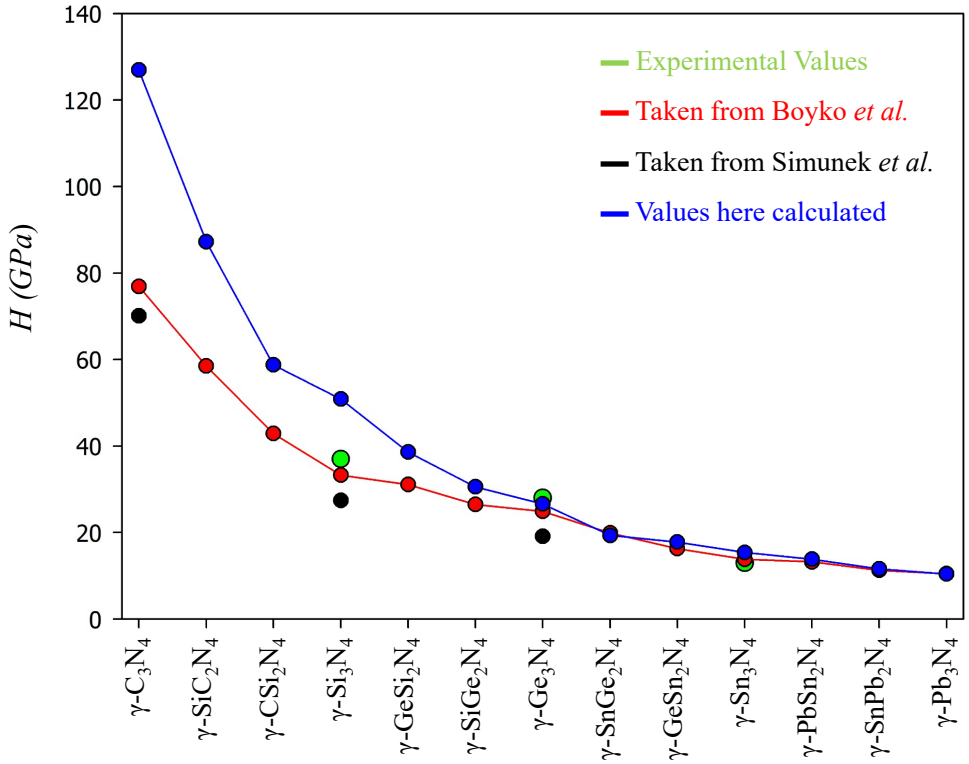


Fig. S1. The calculated Hardness values (*H*) along to previously published data. For more information, see Table S3.

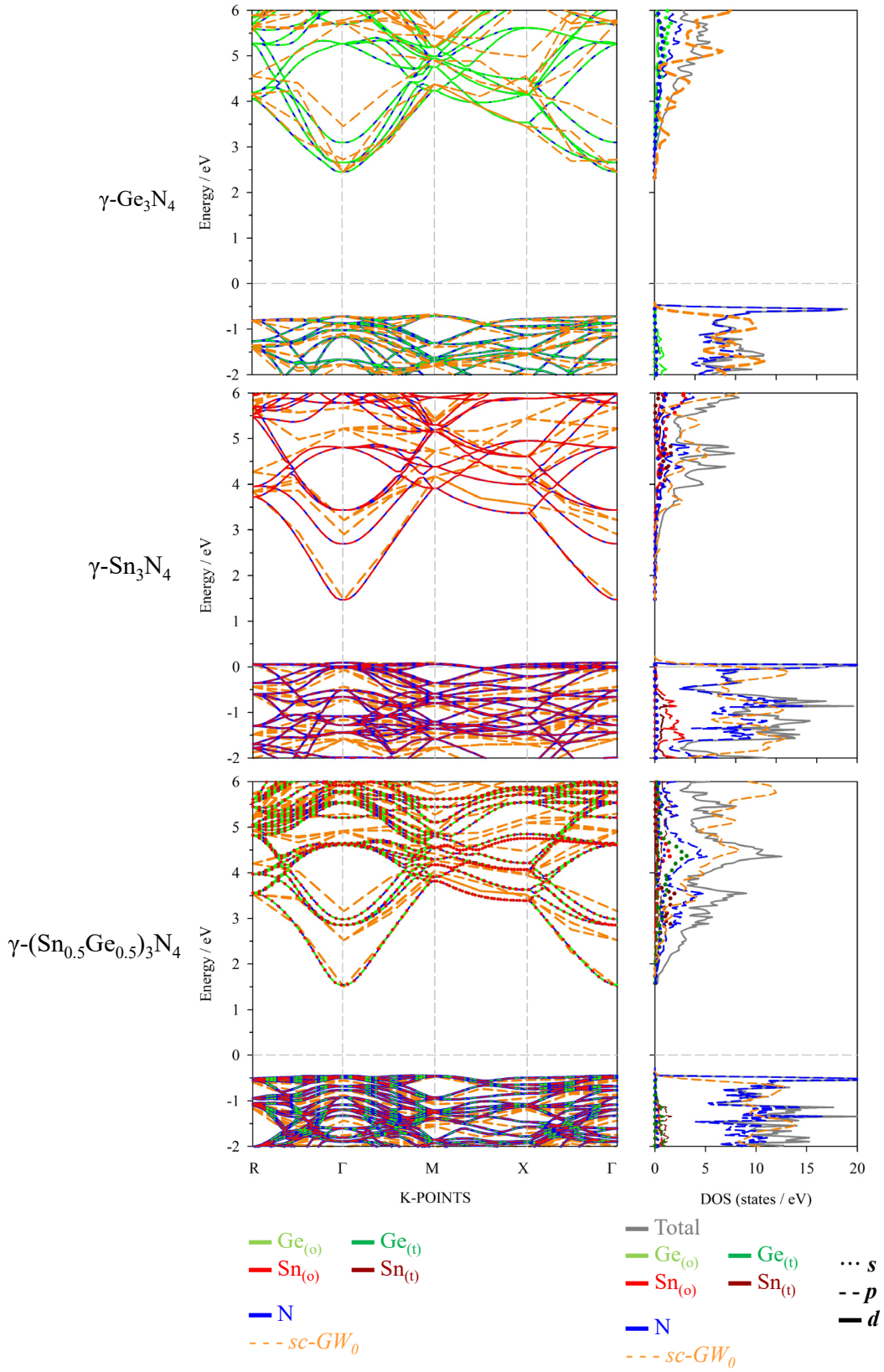


Fig. S2. Projected electronic band structure (only the main atomic contributions have been considered) and Density of States for γ-$(Sn_xGe_{1-x})_3N_4$ (x = 0.0, 0.5, 1.0) obtained after applying a scissor operator (based on sc-*GW*$_0$ approach) over PBE. Orange dotted lines stand for sc-*GW*$_0$ results. The zero of energy has been set at the Fermi level (grey dotted line). For more information about the application of a scissor operator see reference [11].

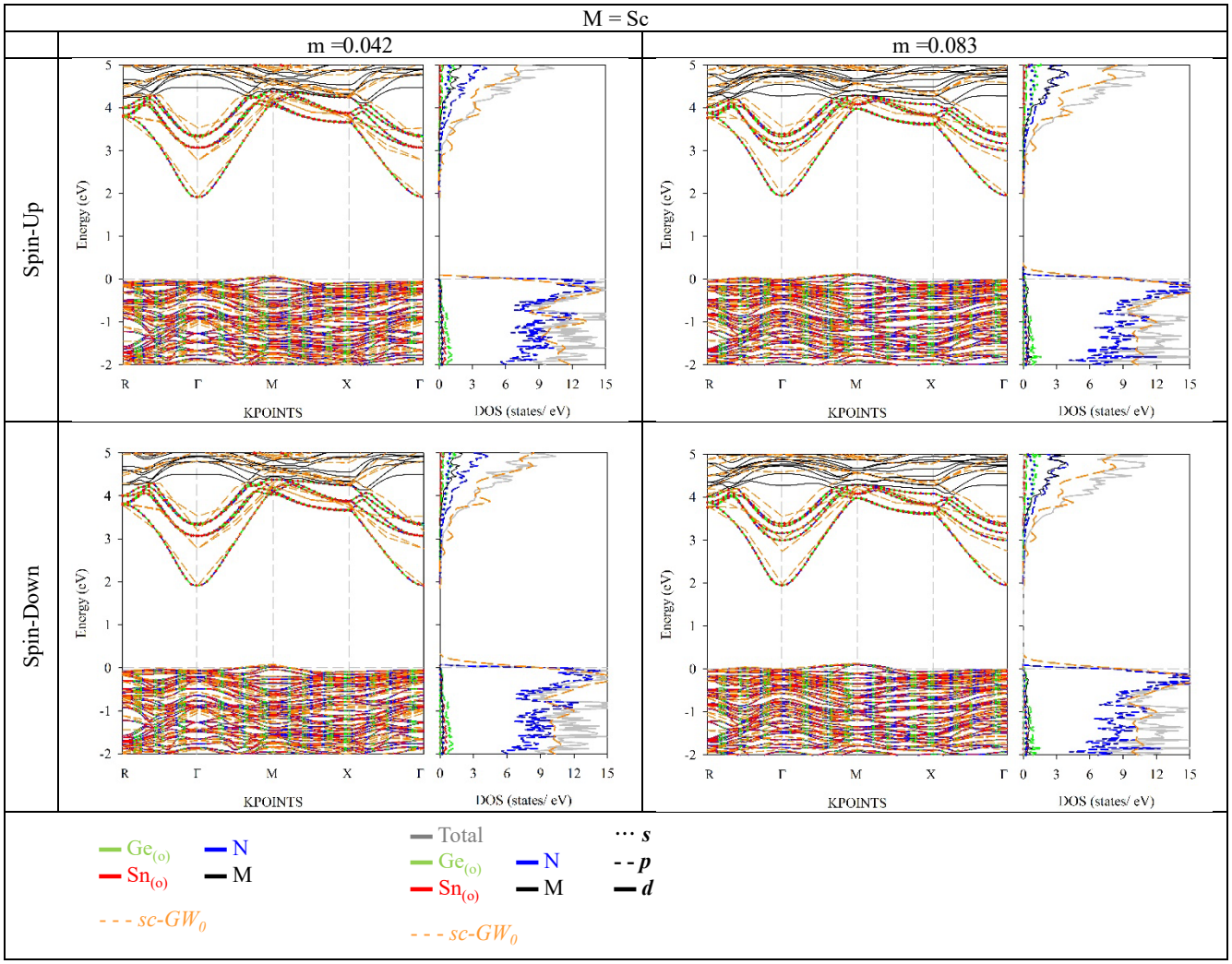


Fig. S3. Projected electronic band structure (only the main atomic contributions have been considered) and Density of States for γ-($Sc_mSn_{0.5-m}Ge_{0.5}$)$_3N_4$ obtained after applying a scissor operator (based on sc-*GW*$_0$ approach) over PBE. Orange dotted lines stand for sc-*GW*$_0$ results. The zero of energy has been set at the Fermi level (grey dotted line). For more information about the application of a scissor operator see reference [11].

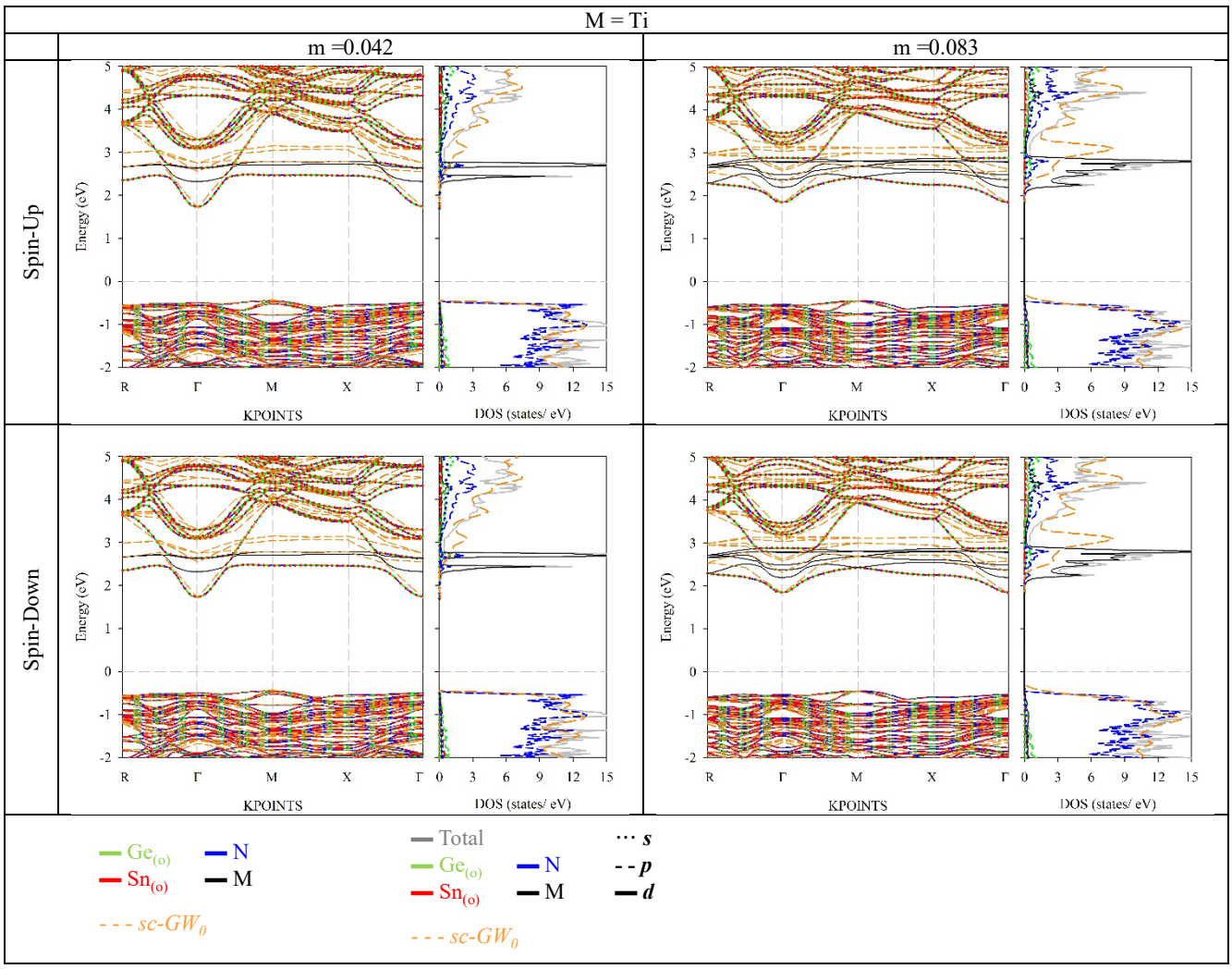


Fig. S4. Projected electronic band structure (only the main atomic contributions have been considered) and Density of States for γ-($Ti_mSn_{0.5-m}Ge_{0.5}$)$_3N_4$ obtained after applying a scissor operator (based on sc-*GW*$_0$ approach) over PBE. Orange dotted lines stand for sc-*GW*$_0$ results. The zero of energy has been set at the Fermi level (grey dotted line). For more information about the application of a scissor operator see reference [11].

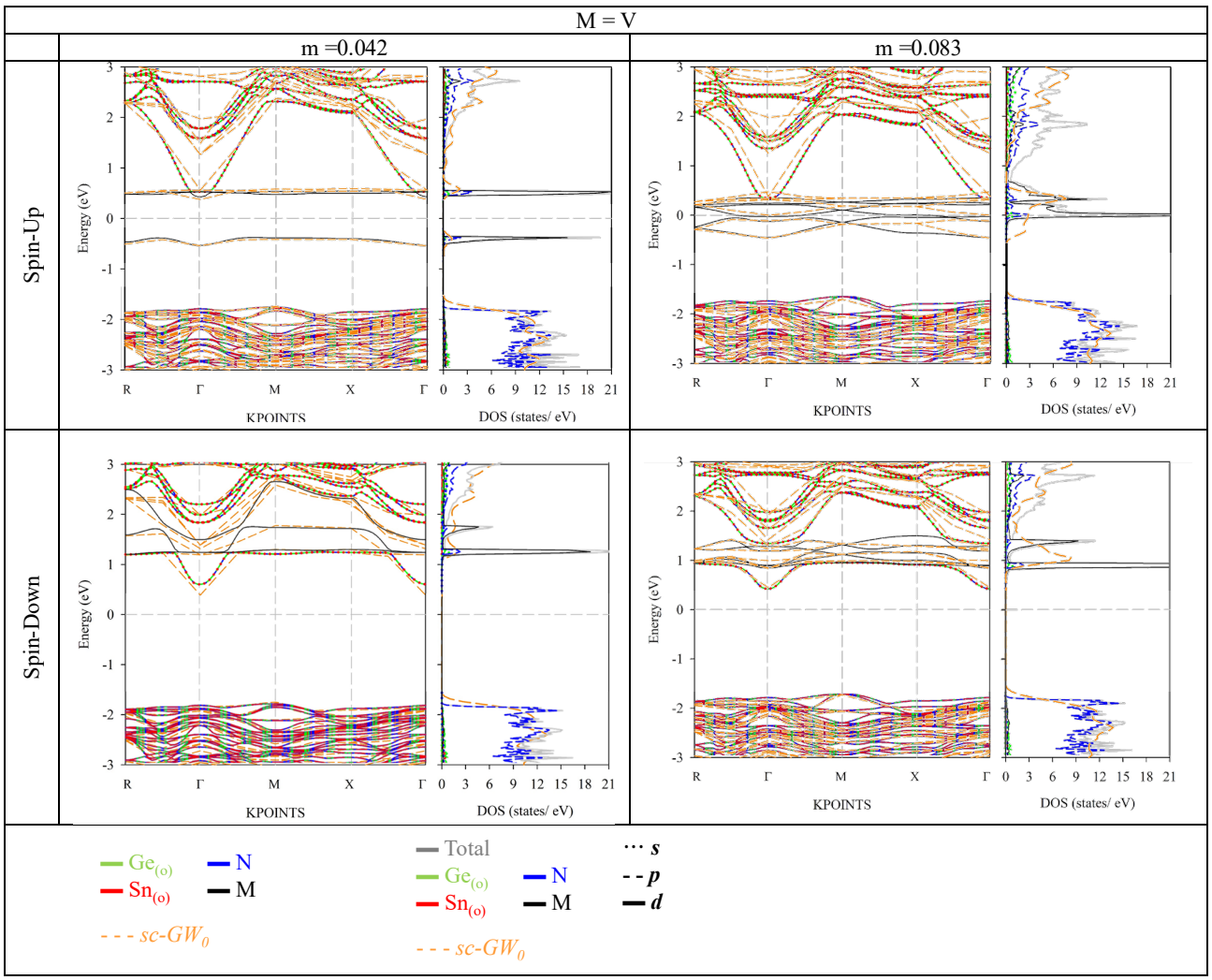


Fig. S5. Projected electronic band structure (only the main atomic contributions have been considered) and Density of States for γ-$(V_mSn_{0.5-m}Ge_{0.5})_3N_4$ obtained after applying a scissor operator (based on sc-*GW*$_0$ approach) over PBE. Orange dotted lines stand for sc-*GW*$_0$ results. The zero of energy has been set at the Fermi level (grey dotted line). For more information about the application of a scissor operator see reference [11].

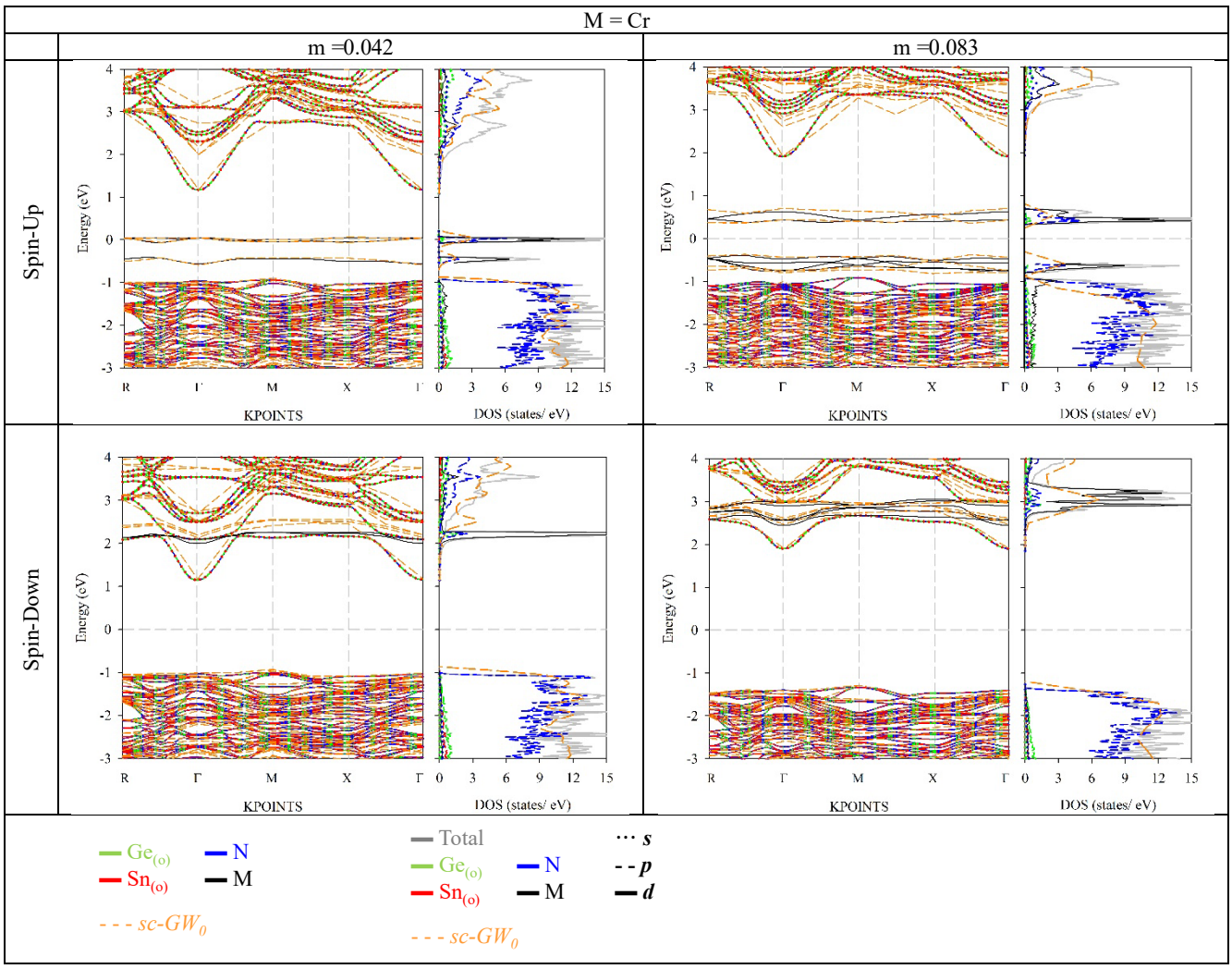


Fig. S6. Projected electronic band structure (only the main atomic contributions have been considered) and Density of States for γ-$(Cr_mSn_{0.5-m}Ge_{0.5})_3N_4$ obtained after applying a scissor operator (based on sc-GW_0 approach) over PBE. Orange dotted lines stand for sc-GW_0 results. The zero of energy has been set at the Fermi level (grey dotted line). For more information about the application of a scissor operator see reference [11].

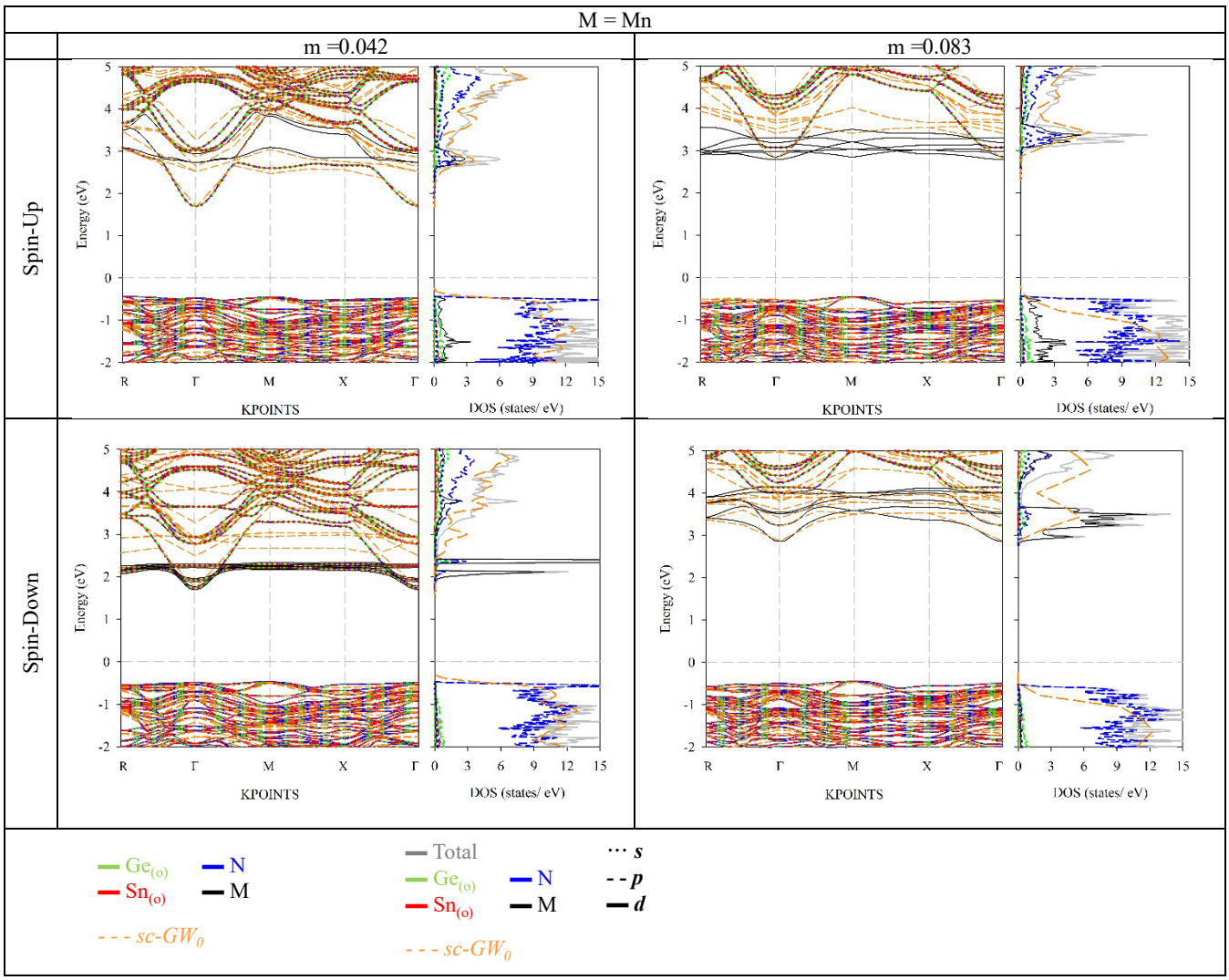


Fig. S7. Projected electronic band structure (only the main atomic contributions have been considered) and Density of States for γ-$(Mn_mSn_{0.5-m}Ge_{0.5})_3N_4$ obtained after applying a scissor operator (based on sc-GW_0 approach) over PBE. Orange dotted lines stand for sc-GW_0 results. The zero of energy has been set at the Fermi level (grey dotted line). For more information about the application of a scissor operator see reference [11].

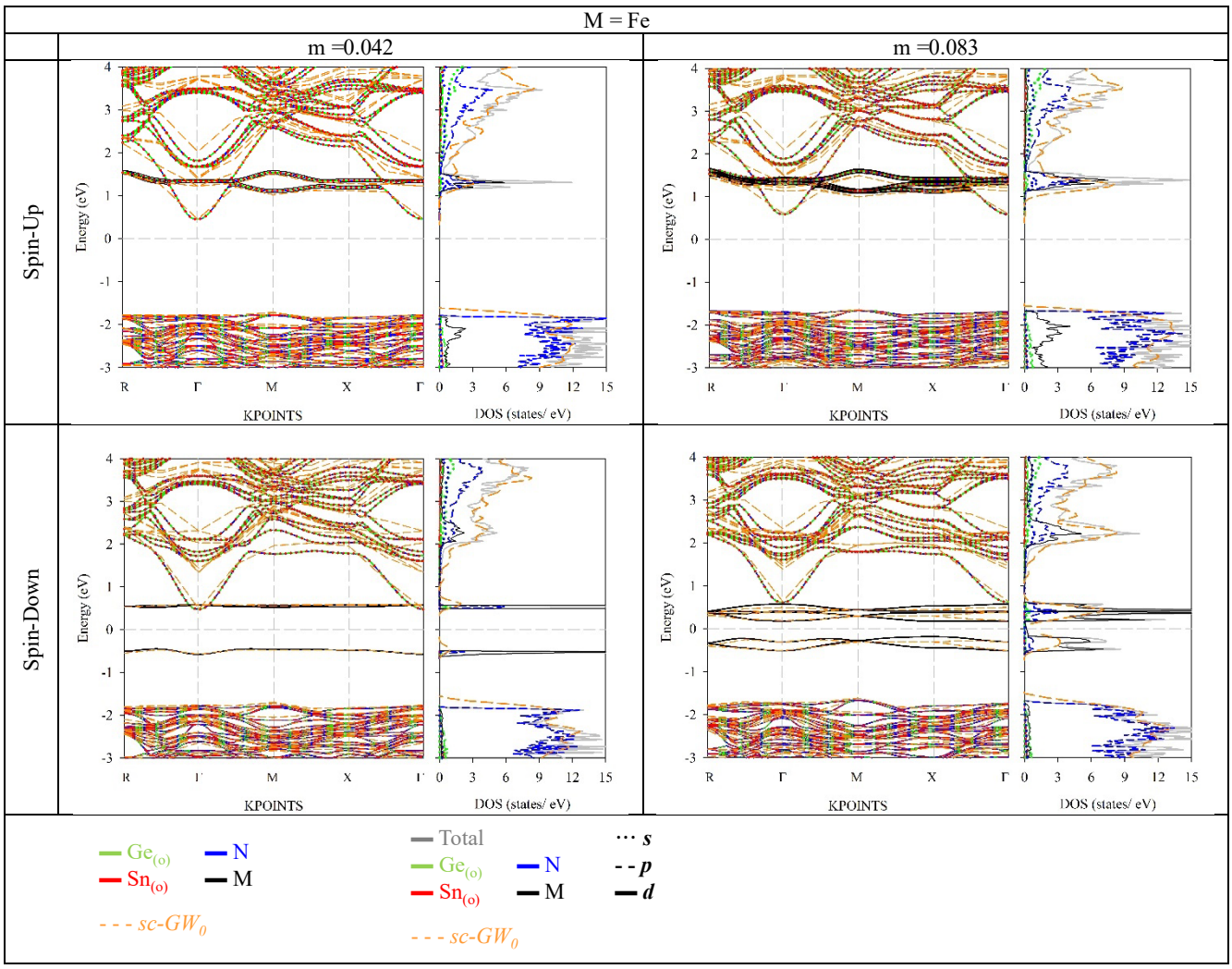


Fig. S8. Projected electronic band structure (only the main atomic contributions have been considered) and Density of States for γ-($Fe_mSn_{0.5-m}Ge_{0.5}$)$_3N_4$ obtained after applying a scissor operator (based on sc-*GW*$_0$ approach) over PBE. Orange dotted lines stand for sc-*GW*$_0$ results. The zero of energy has been set at the Fermi level (grey dotted line). For more information about the application of a scissor operator see reference [11].

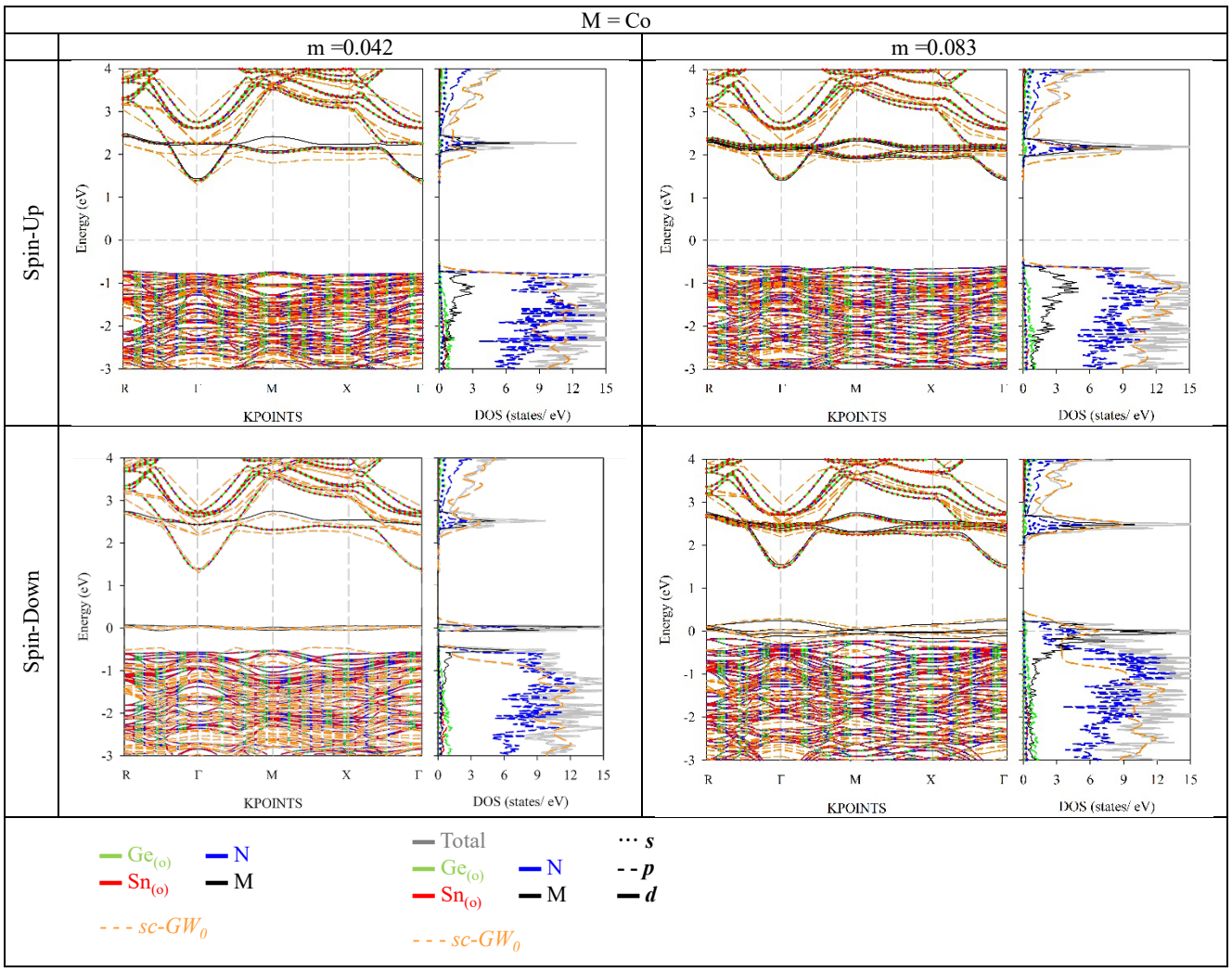


Fig. S9. Projected electronic band structure (only the main atomic contributions have been considered) and Density of States for γ-$(Co_mSn_{0.5-m}Ge_{0.5})_3N_4$ obtained after applying a scissor operator (based on sc-GW_0 approach) over PBE. Orange dotted lines stand for sc-GW_0 results. The zero of energy has been set at the Fermi level (grey dotted line). For more information about the application of a scissor operator see reference [11].

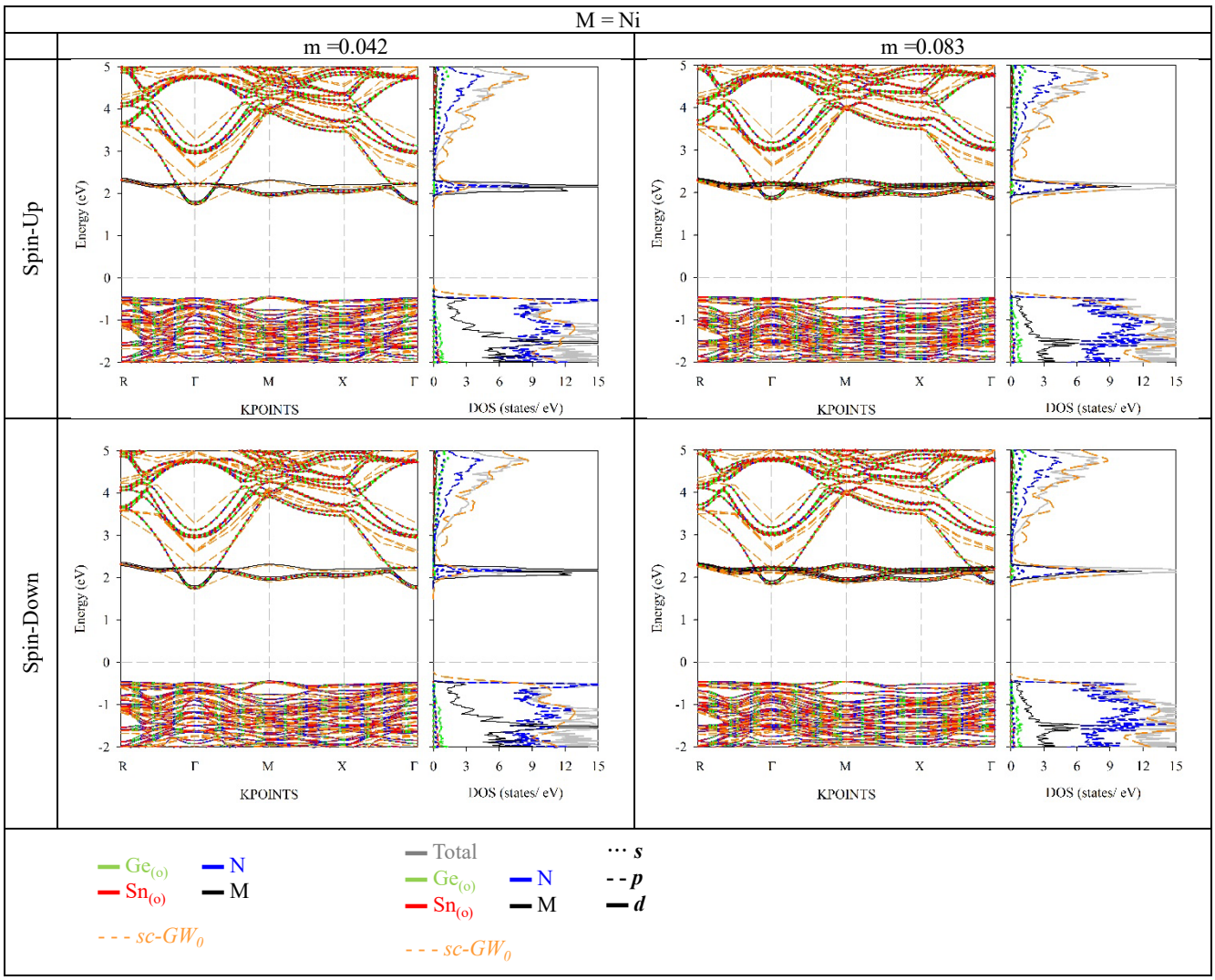


Fig. S10. Projected electronic band structure (only the main atomic contributions have been considered) and Density of States for γ-$(Ni_mSn_{0.5-m}Ge_{0.5})_3N_4$ obtained after applying a scissor operator (based on sc-GW_0 approach) over PBE. Orange dotted lines stand for sc-GW_0 results. The zero of energy has been set at the Fermi level (grey dotted line). For more information about the application of a scissor operator see reference [11].

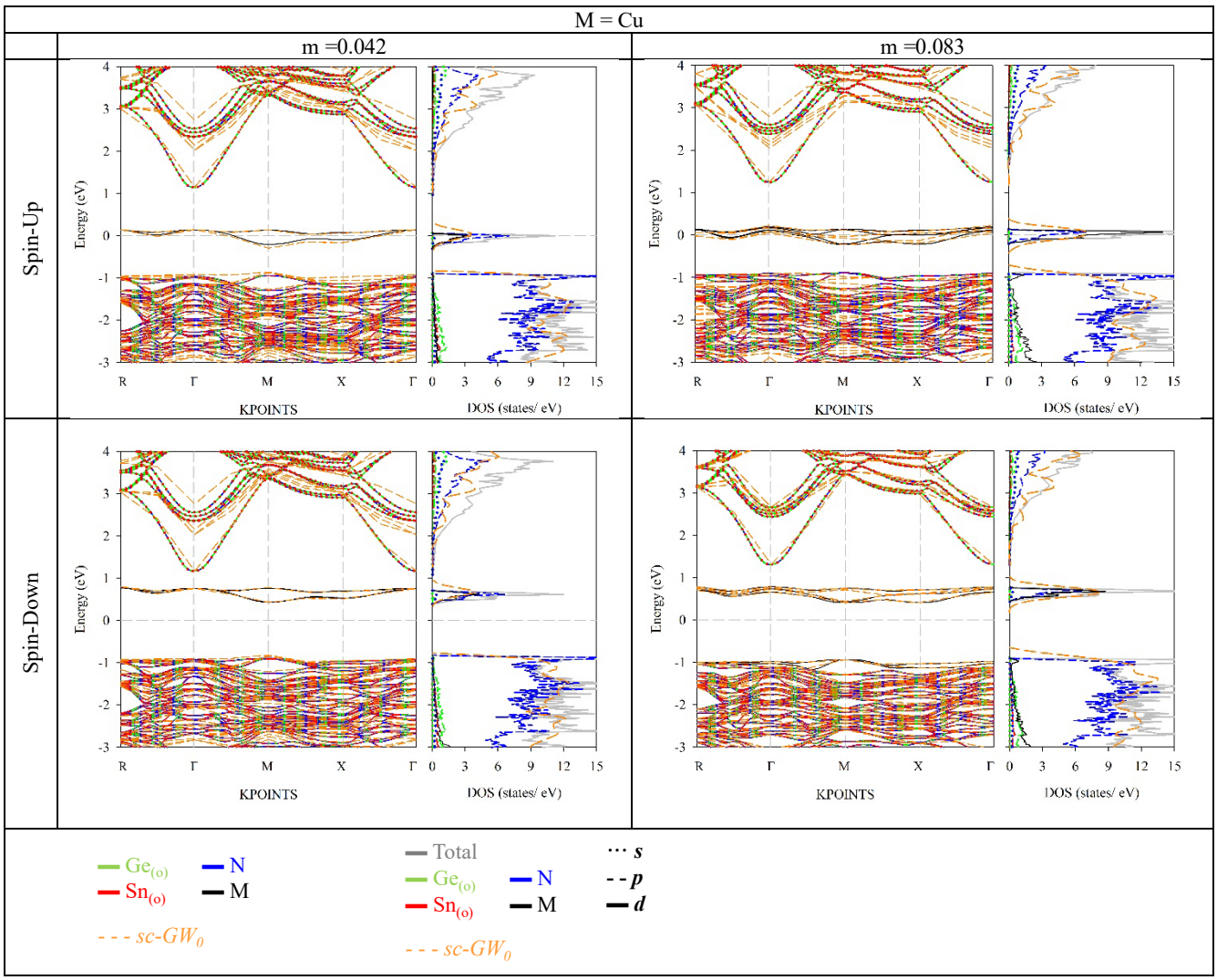


Fig. S11. Projected electronic band structure (only the main atomic contributions have been considered) and Density of States for γ-$(Cu_mSn_{0.5-m}Ge_{0.5})_3N_4$ obtained after applying a scissor operator (based on sc-GW_0 approach) over PBE. Orange dotted lines stand for sc-GW_0 results. The zero of energy has been set at the Fermi level (grey dotted line). For more information about the application of a scissor operator see reference [11].

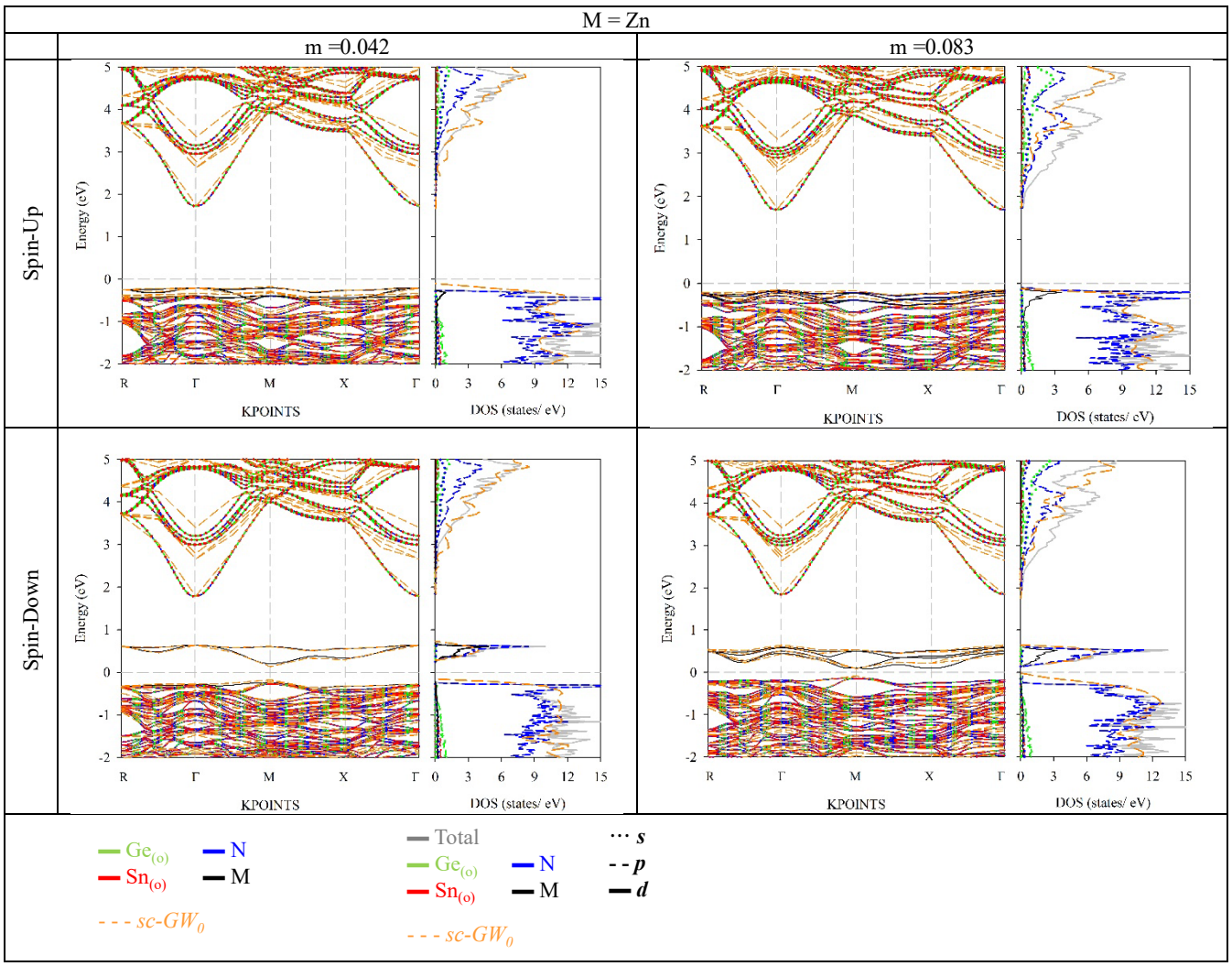


Fig. S12. Projected electronic band structure (only the main atomic contributions have been considered) and Density of States for γ-$(Zn_mSn_{0.5-m}Ge_{0.5})_3N_4$ obtained after applying a scissor operator (based on sc-*GW*$_0$ approach) over PBE. Orange dotted lines stand for sc-*GW*$_0$ results. The zero of energy has been set at the Fermi level (grey dotted line). For more information about the application of a scissor operator see reference [11].

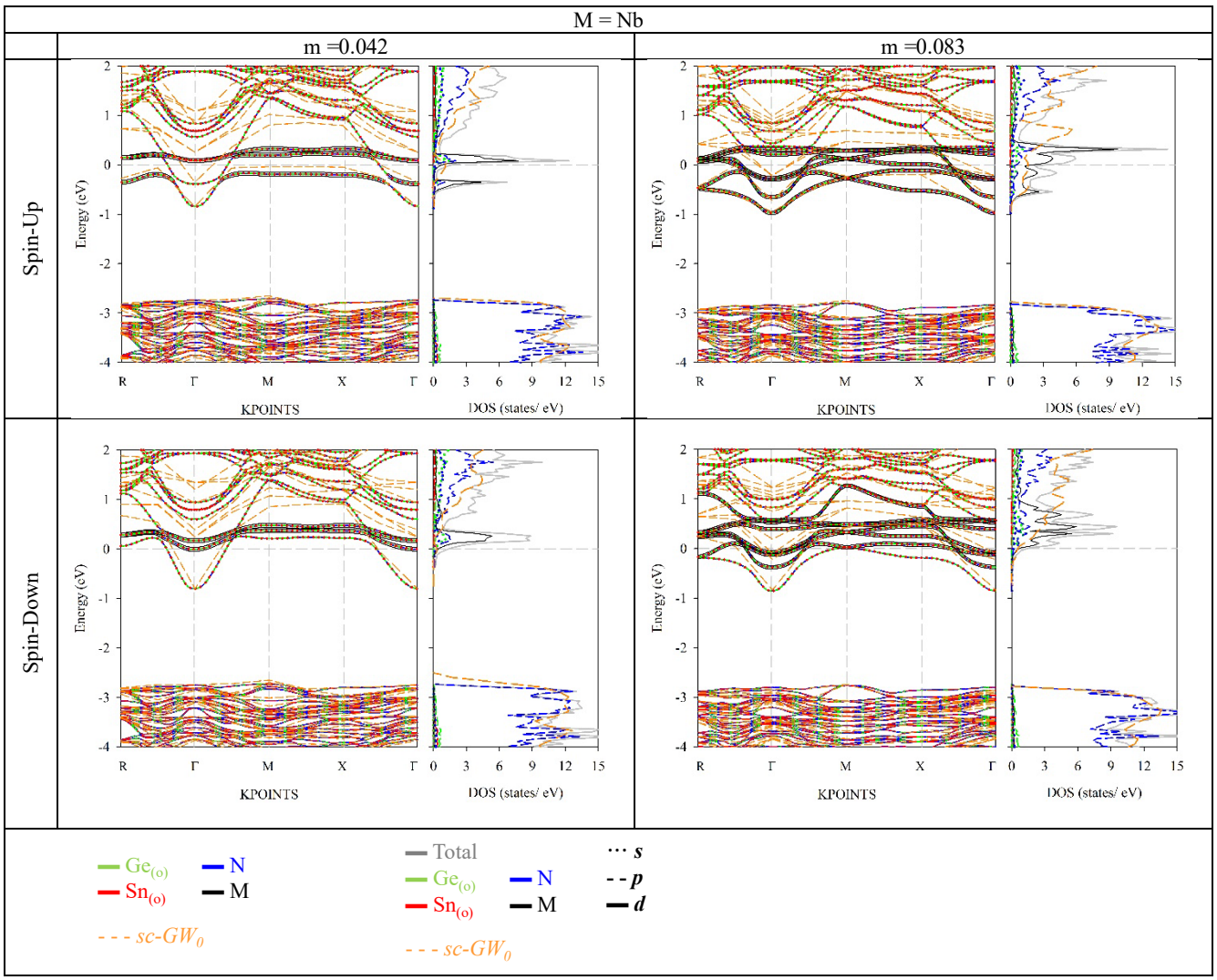


Fig. S13. Projected electronic band structure (only the main atomic contributions have been considered) and Density of States for γ-$(Nb_mSn_{0.5-m}Ge_{0.5})_3N_4$ obtained after applying a scissor operator (based on sc-GW_0 approach) over PBE. Orange dotted lines stand for sc-GW_0 results. The zero of energy has been set at the Fermi level (grey dotted line). For more information about the application of a scissor operator see reference [11].

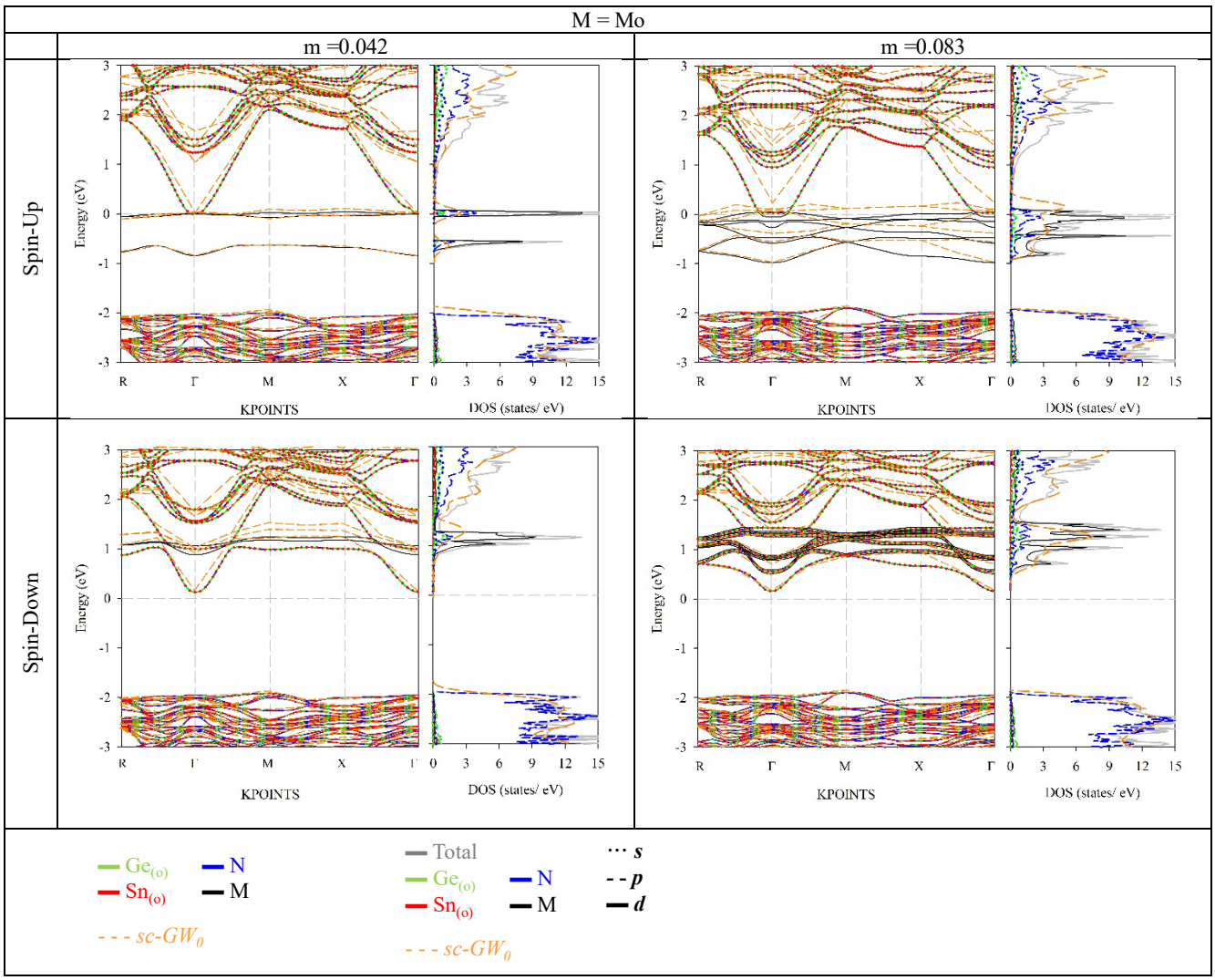


Fig. S14. Projected electronic band structure (only the main atomic contributions have been considered) and Density of States for γ-$(Mo_mSn_{0.5-m}Ge_{0.5})_3N_4$ obtained after applying a scissor operator (based on sc-GW_0 approach) over PBE. Orange dotted lines stand for sc-GW_0 results. The zero of energy has been set at the Fermi level (grey dotted line). For more information about the application of a scissor operator see reference [11].

References

[1] A. Šimůnek, J. Vackář, Hardness of Covalent, Ionic Crystals: First-Principle Calculations, Phys. Rev. Lett. 96 (2006) 085501, https://doi.org/10.1103/PhysRevLett.96.085501.

[2] T. D. Boyko, A. Moewes, The hardness of group 14 spinel nitrides revisited, J. Ceram. Soc. JAPAN 124 (2016) 1063-1066, https://doi.org/10.2109/jcersj2.16097.

[3] J. Z. Jiang, F. Kragh, D. J. Frost, K. StÃ¥hl, H. Lindelov, Hardness, thermal stability of cubic silicon nitride, J. Phys.: Condens. Matter. 13 (2001) L515-L520, https://doi.org/10.1088/0953-8984/13/22/111.

[4] M. P. Shemkunas, W. T. Petuskey, A. V. G. Chizmeshya, K. Leinenweber, G. H. Wolf, Hardness, elasticity, fracture toughness of polycrystalline spinel germanium nitride, tin nitride, Journal of Materials Research, 19 (2004) 1392-1399, https://doi.org/10.1557/JMR.2004.0186.

[5] K. Leinenweber, M. O'Keeffe, M. Somayazulu, H. Hubert, P. F. McMillan, G. H. Wolf, Synthesis, Structure Refinement of the Spinel, γ-Ge3N4, Chem. Eur. J. 5 (1999) 3076-3078, https://doi.org/10.1002/(SICI)1521-3765(19991001)5:10<3076::AID-CHEM3076>3.0.CO;2-D.

[6] M. P. Shemkunas, G. H. Wolf, K. Leinenweber, W. T. Petuskey, Rapid Synthesis of Crystalline Spinel Tin Nitride by a Solid-State Metathesis Reaction, J. Am. Ceram. Soc. 85 (2002) 101-104, https://doi.org/10.1111/j.1151-2916.2002.tb00047.x.

[7] A. Zerr, M. Kempf, M. Schwarz, E. Kroke, M. Göken, R. Riedel, Elastic Moduli, Hardness of Cubic Silicon Nitride, J. Am. Ceram. Soc. 85 (2002) 86-90, https://doi.org/10.1111/j.1151-2916.2002.tb00044.x.

[8] D. W. Smith, Inorganic Substances: A Prelude to the Study of Descriptive Inorganic Chemistry (Cambridge Texts in Chemistry, Biochemistry). Cambridge: Cambridge University Press, 1990.

[9] C. M. Caskey et al., Semiconducting properties of spinel tin nitride, other IV3N4 polymorphs, J. Mater. Chem. C 3 (2015) 1389-1396, https://doi.org/10.1039/C4TC02528H.

[10] T. D. Boyko, A. Hunt, A. Zerr, A. Moewes, Electronic Structure of Spinel-Type Nitride Compounds Si3N4, Ge3N4, Sn3N4 with Tunable Band Gaps: Application to Light Emitting Diodes, Phys. Rev. Lett. 111 (2013) 097402, https://doi.org/10.1103/PhysRevLett.111.097402.

[11] G. García, P. Palacios, E. Menéndez-Proupin, A. L. Montero-Alejo, J. C. Conesa, P. Wahnón, Influence of chromium hyperdoping on the electronic structure of CH3NH3PbI3 perovskite: a first-principles insight, Sci. Rep. 8 (2018) 2511, https://doi.org/10.1038/s41598-018-20851-x.

Supplementary material
Third publication

Electronic Supplementary Material (ESI) for Inorganic Chemistry Frontiers.
This journal is © the Partner Organisations 2021

Effect of the chemical composition on the structural, thermodynamical and mechanical properties of all-inorganic Halide Perovskites

Pablo Sánchez-Palencia,[1,2] Gregorio García,[1,2*] Perla Wahnón,[1,2] Pablo Palacios[1,3]

[1] Instituto de Energía Solar, ETSI Telecomunicación, Universidad Politécnica de Madrid, Ciudad Universitaria, s/n, 28040, Madrid, Spain

[2] Departamento de Tecnología Fotónica y Bioingeniería, ETSI Telecomunicación, Universidad Politécnica de Madrid, Ciudad Universitaria, s/n, 28040 Madrid, Spain

[3] Departamento de Física aplicada a las Ingenierías Aeronáutica y Naval. ETSI Aeronáutica y del Espacio, Universidad Politécnica de Madrid, Pz. Cardenal Cisneros, 3, 28040 Madrid, Spain.

SUPPLEMENTARY MATERIAL

APPENDIX 1 – SETS OF IONIC RADII.

Three different properties presented in this work depend directly on the ionic radii of the different atoms the perovskite is made of. Goldschmidt's and Sun's parameters and bonding strength are by definition, according to equations 1-3 (including related equations 2.1, 2.2 and 3.4), calculated mainly from the ionic radii. For all those calculations presented in the main body of this work, the Shannon's revised effective crystal radii,[1] as it is conventional in the field of crystallography, have been used, considering effective charges of the atoms (A=1, B=2, X=-1) and coordination environments (A=12, B=6, X=6) as those in the perovskite. Nevertheless, as there are also other sets which are also frequently used, other options have been explored, testing results with the Pauling's empirical crystal radii[2] and the Shannon's effective ionic radii,[1] besides different coordination environments for the different atoms.

In order to dismiss the bias based upon the specific used set, the knowledge and information extracted from the previously commented parameters has been checked with the other sets proposed before. In line with the purpose of those parameters, the stability limit defined by the Goldschmidt's parameter has been reevaluated, as well as the kindness of the correlation between Sun's parameter and formation enthalpy from fundamental elements (ΔH_f) and between bonding strength and formation enthalpy from binary competitor compounds (ΔH_s).

Below, two data tables are attached. The first one, Table S1,[1–5] presents the values for the different atoms of the studied perovskites within the different tested sets of radii. The second one, Table S2 shows, for every set, the minimal value of the Goldschmidt's parameter and the coefficient of determination and mean absolute error of the correlations between the other two parameters and the formation enthalpies.

The nomenclature for the different sets of radii is the following. SC corresponds to Shannon crystal, SI to Shannon ionic and P stands for Pauling's set. O and L stands for the correction of Sn^{2+} radius proposed by *Oku*[3] and *Li*[4] respectively, using Shannon ionic

radii for the rest of the atoms. Additionally, subindexes 1-4 correspond to different coordination environments tested, respectively A=12, B=6, X=6; A=6, B=6, X=6; A=12, B=6, X=2 and A=6, B=6, X=2.

TABLE S1. Tested sets of ionic radii [Å] for the different ions present in the studied perovskites.

[Å]	Cs^+	Pb^{2+}	Sn^{2+}	I^-	Br^-
SC_1	2.02	1.33	1.20	2.06	1.82
SC_2	1.81	1.33	1.20	2.06	1.82
P	1.69	1.22	1.03	2.16	1.95
SI_1	1.88	1.19	1.05	2.20	1.96
SI_2	1.67	1.19	1.05	2.20	1.96
SI_3	1.88	1.19	1.05	1.90	1.69
SI_4	1.67	1.19	1.05	1.90	1.69
O	1.88	1.19	0.93	2.20	1.96
L	1.88	1.19	1.10	2.20	1.96

TABLE S2. Results for the dependent properties: minimum Goldschmidt's tolerance factor t, Sun's parameter correlation $\zeta(R^2/\text{MAE[meV/atom]})$ and bonding strength correlation $S(R^2/\text{MAE[meV/atom]})$, with the different sets of radii.

	t	ζ (R^2/MAE[meV/atom])	S (R^2/MAE[meV/atom])
SC_1	0.85	0.993 / 6.8	0.896 / 4.5
SC_2	0.81	0.981 / 11.9	0.892 / 4.6
P	0.81	0.805 / 36.8	0.933 / 3.8
SI_1	0.85	0.994 / 6.1	0.916 / 4.1
SI_2	0.81	0.937 / 21.5	0.912 / 4.2
SI_3	0.87	0.995 / 6.1	0.915 / 4.1
SI_4	0.82	0.940 / 21.1	0.912 / 4.2
O	0.85	0.643 / 48.9	0.928 / 3.8
L	0.85	0.891 / 29.7	0.880 / 4.8

From the data in TABLE S2 can be clearly seen that there are no big differences in performance between different sets of radii, except for the case of Oku set which fails for Sun's parameter correlation. The rest of sets produce results with proper correlation indexes and with t parameters above the stability limit of 0.8, in addition trends are also maintained. This way non-reliability of the results on the chosen set can be considered proven. Beyond this, it can be seen how dodecahedral coordination environments for the Cesium atoms performs better than octahedral environments, the ones that are usual in bibliography.[3–6] In fact, SI_1 and SI_3 sets present better results than the finally chosen for the work SC_1, but crystalline structure of perovskites and comparison reasons decide towards the last one. It's also remarkable that Sun's parameter correlation performs better

with more covalent sets of radios while the bonding strength correlation works better with more ionic sets like the Pauling and Oku sets.

APPENDIX 2 – COMPLETE DATA

To complement all the information presented in the contour plots showed in the main body of this work, the numerical data used to fill those graphs is presented here in table format, making sure no piece of information is missed or deprecated. This way, for each property with a contour figure in the work, plus for the Poisson's ratio, there is a table with all the data in this section.

Lattice constant [Å]		X						
		0	**0.167**	**0.333**	**0.5**	**0.667**	**0.833**	**1**
b	**0**	6.238	6.227	6.214	6.185	6.157	6.143	6.132
	0.125	6.249	6.233	6.219	6.196	6.164	6.150	6.136
	0.25	6.258	6.241	6.227	6.201	6.174	6.160	6.145
	0.5	6.166	6.151	6.135	6.123	6.088	6.070	6.054
	0.75	5.870	5.858	5.845	5.817	5.788	5.774	5.759
	0.875	5.868	5.854	5.841	5.815	5.786	5.771	5.758
	1	5.871	5.856	5.841	5.812	5.785	5.773	5.756

Shape ratio		x						
		0	**0.167**	**0.333**	**0.5**	**0.667**	**0.833**	**1**
b	**0**	1.00	1.00	1.00	1.00	1.00	1.00	1.00
	0.125	0.97	0.97	0.97	0.97	0.97	0.97	0.97
	0.25	0.94	0.94	0.94	0.93	0.93	0.93	0.93
	0.5	0.95	0.95	0.95	0.95	0.95	0.95	0.95
	0.75	1.07	1.07	1.07	1.07	1.07	1.07	1.07
	0.875	1.03	1.03	1.03	1.03	1.03	1.03	1.03
	1	1.00	1.00	1.00	1.00	1.00	1.00	1.00

Volume [Å^3]		x						
		0	**0.167**	**0.333**	**0.5**	**0.667**	**0.833**	**1**
b	**0**	242.758	241.420	239.910	236.571	233.388	231.813	230.540
	0.125	236.315	234.534	232.912	229.977	226.656	225.092	223.461
	0.25	229.208	227.466	225.895	222.877	219.908	218.287	216.628
	0.5	222.555	221.051	219.440	217.320	213.869	212.180	210.369
	0.75	215.656	214.242	212.844	209.901	206.852	205.400	203.833
	0.875	208.816	207.422	205.956	203.268	200.261	198.789	197.370
	1	202.353	200.793	199.321	196.317	193.644	192.440	190.656

Goldschmidt's parameter		x						
		0	0.167	0.333	0.5	0.667	0.833	1
b	0	0.851	0.855	0.859	0.868	0.876	0.881	0.885
	0.125	0.853	0.857	0.861	0.870	0.878	0.883	0.887
	0.25	0.855	0.859	0.863	0.872	0.880	0.885	0.889
	0.5	0.856	0.861	0.865	0.874	0.883	0.887	0.892
	0.75	0.858	0.862	0.867	0.876	0.885	0.889	0.894
	0.875	0.860	0.864	0.869	0.878	0.887	0.892	0.897
	1	0.862	0.866	0.871	0.880	0.890	0.894	0.899

Sun's parameter		x						
		0	0.167	0.333	0.5	0.667	0.833	1
b	0	1.292	1.291	1.290	1.289	1.288	1.288	1.287
	0.125	1.295	1.295	1.294	1.293	1.292	1.291	1.291
	0.25	1.299	1.299	1.298	1.297	1.296	1.296	1.295
	0.5	1.303	1.303	1.302	1.299	1.299	1.299	1.299
	0.75	1.308	1.307	1.306	1.305	1.304	1.304	1.304
	0.875	1.313	1.312	1.312	1.310	1.309	1.309	1.309
	1	1.318	1.318	1.317	1.316	1.315	1.314	1.315

Bonding strength		x						
		0	0.167	0.333	0.5	0.667	0.833	1
b	0	0.220	0.222	0.223	0.225	0.229	0.230	0.231
	0.125	0.225	0.227	0.228	0.231	0.234	0.235	0.236
	0.25	0.229	0.231	0.232	0.235	0.238	0.239	0.240
	0.5	0.235	0.236	0.237	0.240	0.243	0.245	0.246
	0.75	0.239	0.240	0.242	0.245	0.248	0.249	0.250
	0.875	0.245	0.247	0.248	0.252	0.254	0.256	0.257
	1	0.249	0.251	0.253	0.255	0.259	0.260	0.261

Formation enthalpy ΔH_f [eV/atom]		x						
		0	0.167	0.333	0.5	0.667	0.833	1
b	0	-1.038	-1.031	-1.023	-1.009	-0.995	-0.988	-0.982
	0.125	-1.085	-1.078	-1.070	-1.055	-1.040	-1.034	-1.027
	0.25	-1.135	-1.126	-1.119	-1.104	-1.089	-1.082	-1.075
	0.5	-1.181	-1.174	-1.167	-1.146	-1.133	-1.126	-1.120
	0.75	-1.232	-1.224	-1.216	-1.200	-1.184	-1.177	-1.170
	0.875	-1.282	-1.274	-1.266	-1.249	-1.234	-1.226	-1.219
	1	-1.335	-1.327	-1.318	-1.302	-1.286	-1.279	-1.271

Formation enthalpy ΔH_s [meV/atom]		x						
		0	0.167	0.333	0.5	0.667	0.833	1
b	0	8.8	3.3	-1.9	-12.4	-23.3	-29.1	-35.7
	0.125	0.7	-3.4	-7.7	-17.0	-26.6	-31.7	-37.0
	0.25	-8.8	-12.3	-16.0	-24.3	-32.7	-37.0	-41.5
	0.5	-15.4	-19.8	-23.9	-25.1	-34.0	-38.7	-43.4
	0.75	-26.9	-29.7	-32.3	-38.0	-43.5	-46.7	-49.9
	0.875	-37.3	-39.6	-41.4	-45.6	-50.6	-53.1	-56.0
	1	-50.7	-52.1	-53.4	-56.5	-60.3	-62.8	-64.4

B-M Bulk modulus [GPa]		x						
		0	0.167	0.333	0.5	0.667	0.833	1
b	0	17.46	17.53	17.62	17.79	18.01	18.11	18.21
	0.125	18.08	18.09	18.20	18.41	18.62	18.73	18.85
	0.25	18.72	18.78	18.87	19.06	19.27	19.37	19.49
	0.5	18.69	18.82	18.89	19.31	19.62	19.66	19.91
	0.75	20.06	20.11	20.20	20.42	20.62	20.72	20.83
	0.875	20.85	20.90	21.01	21.20	21.42	21.52	21.64
	1	21.55	21.66	21.76	22.00	22.18	22.26	22.38

EC Bulk modulus [GPa]		x						
		0	0.167	0.333	0.5	0.667	0.833	1
b	0	20.29	15.36	19.76	19.88	20.05	17.71	19.75
	0.125	20.98	20.37	19.65	20.69	18.22	19.49	20.72
	0.25	22.14	20.85	21.64	21.64	21.77	20.98	21.64
	0.5	20.66	21.98	18.44	22.47	20.93	22.23	22.59
	0.75	24.09	23.10	23.48	23.29	23.78	23.47	23.54
	0.875	25.28	20.98	24.65	24.74	24.64	24.38	24.52
	1	26.50	25.06	25.82	25.98	26.12	25.29	25.65

Shear modulus [GPa]		x						
		0	0.167	0.333	0.5	0.667	0.833	1
b	0	9.49	9.13	9.19	9.49	9.69	9.78	9.79
	0.125	9.85	9.49	9.60	9.78	9.98	10.08	10.20
	0.25	10.34	9.94	10.05	10.23	10.41	10.49	10.52
	0.5	10.54	10.33	10.18	10.59	10.89	10.84	10.86
	0.75	11.29	10.71	10.83	10.94	11.15	11.19	11.19
	0.875	11.72	11.14	11.33	11.42	11.60	11.63	11.65
	1	12.34	11.68	11.84	11.95	12.07	12.06	11.95

Young's modulus [GPa]		x						
		0	0.167	0.333	0.5	0.667	0.833	1
b	0	24.63	22.87	23.88	24.55	25.03	24.77	25.21
	0.125	25.55	24.64	24.77	25.34	25.32	25.79	26.30
	0.25	26.85	25.72	26.11	26.51	26.94	26.97	27.17
	0.5	27.02	26.78	25.79	27.45	27.85	27.97	28.08
	0.75	29.29	27.84	28.16	28.39	28.94	28.97	28.98
	0.875	30.46	28.40	29.48	29.68	30.08	30.09	30.18
	1	32.05	30.34	30.80	31.07	31.39	31.22	31.03

Poisson's ratio		x						
		0	0.167	0.333	0.5	0.667	0.833	1
b	0	0.30	0.25	0.30	0.29	0.29	0.27	0.29
	0.125	0.30	0.30	0.29	0.30	0.27	0.28	0.29
	0.25	0.30	0.29	0.30	0.30	0.29	0.29	0.29
	0.5	0.28	0.30	0.27	0.30	0.28	0.29	0.29
	0.75	0.30	0.30	0.30	0.30	0.30	0.29	0.29
	0.875	0.30	0.27	0.30	0.30	0.30	0.29	0.29
	1	0.30	0.30	0.30	0.30	0.30	0.29	0.30

BIBLIOGRAPHY

1 R. D. Shannon, Revised effective ionic radii and systematic studies of interatomic distances in halides and chalcogenides, *Acta Crystallogr. Sect. A*, 1976, **32**, 751.

2 L. Pauling, *The nature of the chemical bond and the structure of molecules and crystals*, Cornell University Press, Ithaca, N. Y., second ed., 1941.

3 T. Oku, Crystal structures of perovskite halide compounds used for solar cells, *Rev. Adv. Mater. Sci.*, 2020, **59**, 264.

4 C. Li, X. Lu, W. Ding, L. Feng, Y. Gao and Z. Guo, Formability of ABX 3 (X = F, Cl, Br, I) halide perovskites, *Acta Crystallogr. Sect. B Struct. Sci.*, 2008, **64**, 702.

5 Q. Sun and W. J. Yin, Thermodynamic Stability Trend of Cubic Perovskites, *J. Am. Chem. Soc.*, 2017, **139**, 14905.

6 W. Travis, E. N. K. Glover, H. Bronstein, D. O. Scanlon and R. G. Palgrave, On the application of the tolerance factor to inorganic and hybrid halide perovskites: A revised system, *Chem. Sci.*, 2016, **7**, 4548.

Supplementary material
Fourth publication

Electronic Supplementary Material (ESI) for Inorganic Chemistry Frontiers.
This journal is © the Partner Organisations 2022

Cation Substitution Effects on the Structural, Electronic and Sun-Light Absorption Features of All-Inorganic Halide Perovskites

Pablo Sánchez-Palencia,[1,2] Gregorio García,[1,2*] Perla Wahnón,[1,2] Pablo Palacios[1,3]

[1] Instituto de Energía Solar, ETSI Telecomunicación, Universidad Politécnica de Madrid, Ciudad Universitaria, s/n, 28040, Madrid, Spain

[2] Departamento de Tecnología Fotónica y Bioingeniería, ETSI Telecomunicación, Universidad Politécnica de Madrid, Ciudad Universitaria, s/n, 28040 Madrid, Spain

[3] Departamento de Física aplicada a las Ingenierías Aeronáutica y Naval. ETSI Aeronáutica y del Espacio, Universidad Politécnica de Madrid, Pz. Cardenal Cisneros, 3, 28040 Madrid, Spain.

*E-mail: g.garcia@upm.es

SUPPLEMENTARY MATERIAL

1. ADDITIONAL ELECTRONIC STRUCTURE GRAPHS

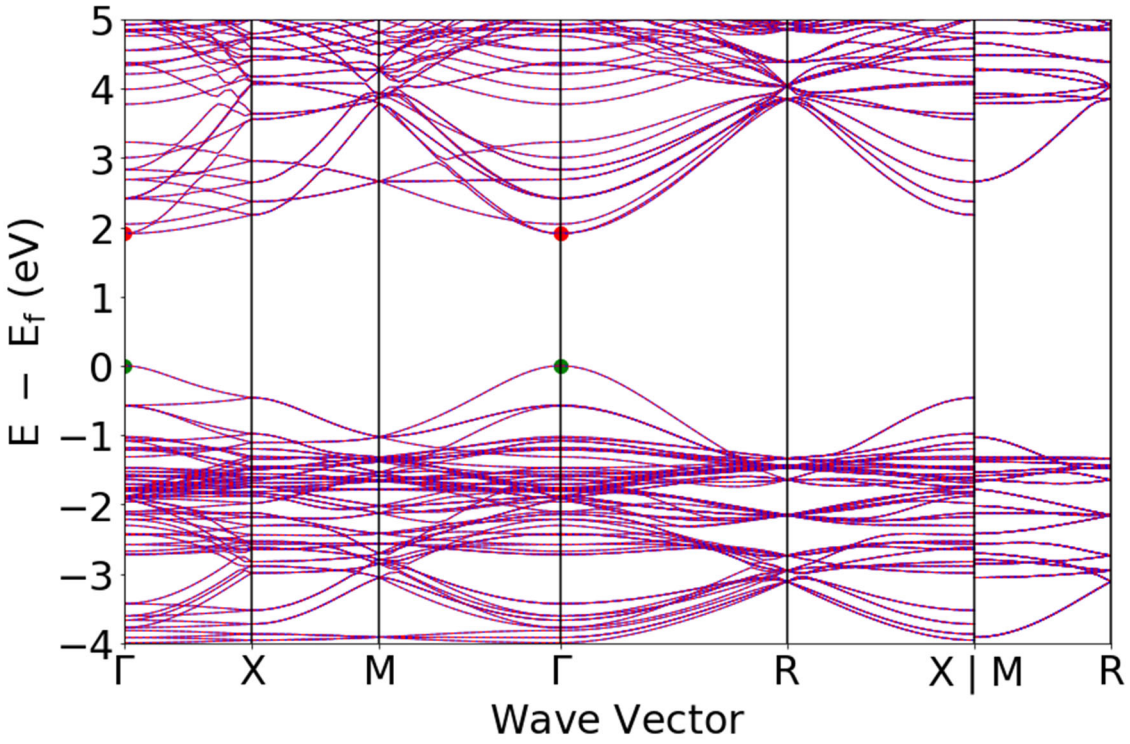


FIGURE S1.1 Band structure of states of $CsPbI_2Br$ with PBE+U (U values of 5.6 eV for *p*-electrons of Pb).

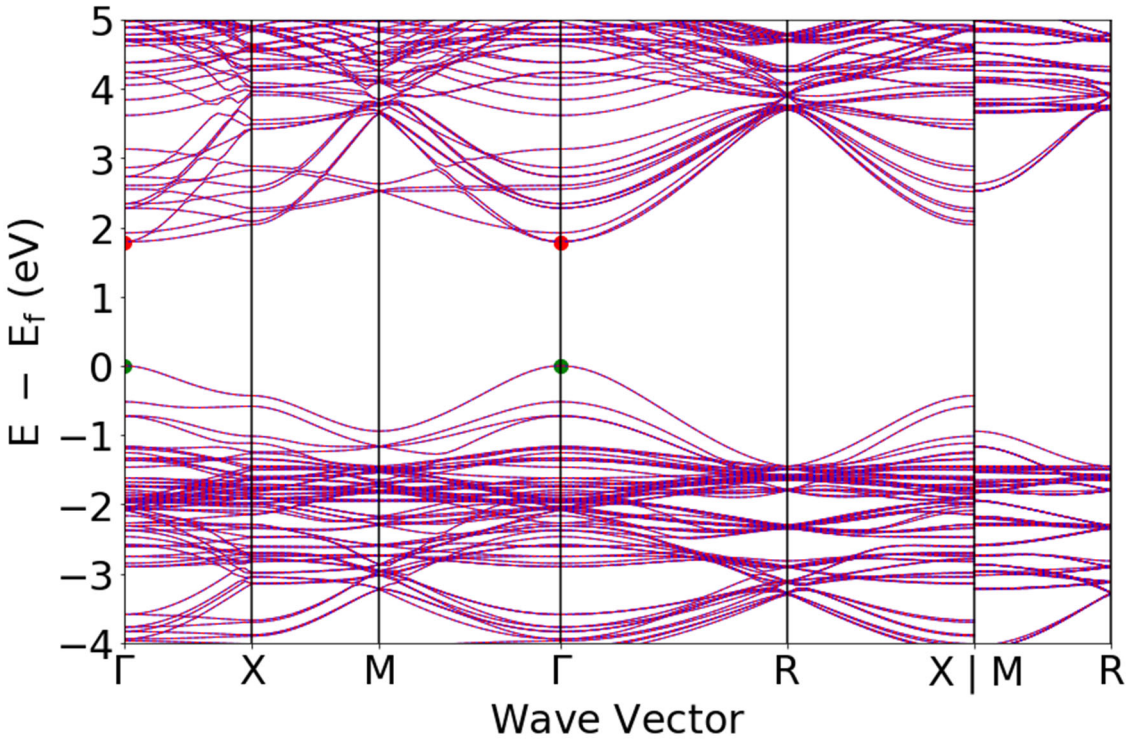


FIGURE S1.2 Band structure of $CsPb_{0.875}Sn_{0.125}I_2Br$ with PBE+U (U values of 5.6 and 11 eV for *p*-electrons of Pb and Sn respectively).

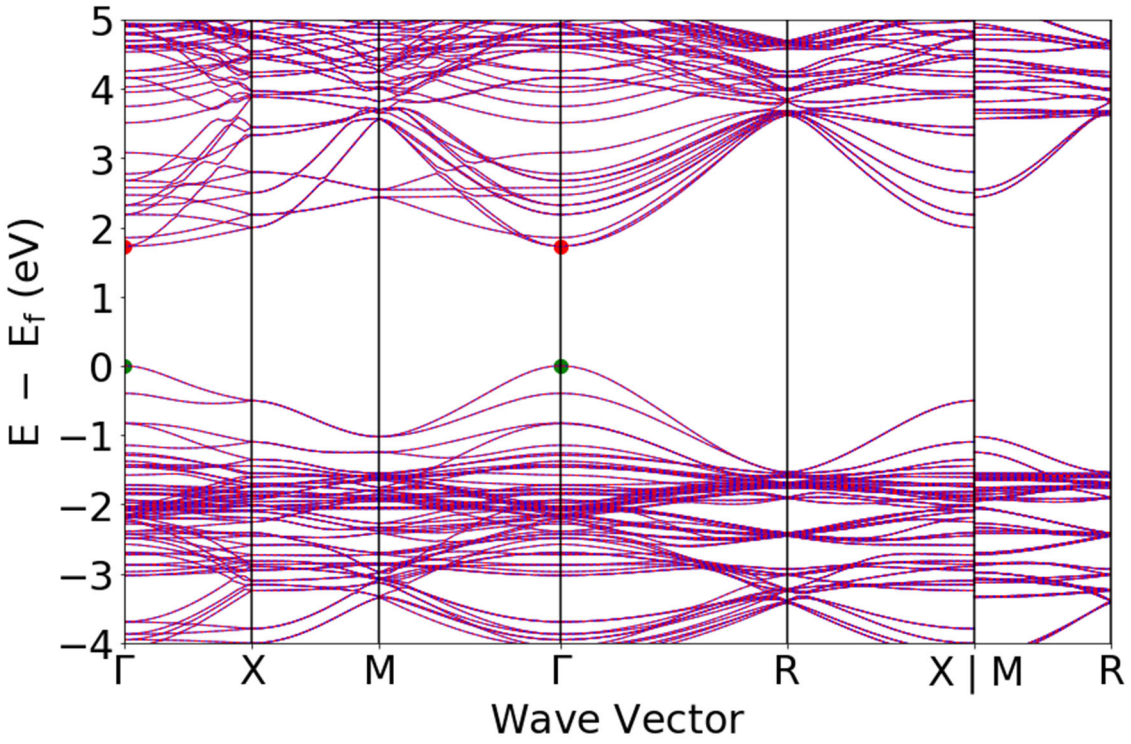


FIGURE S1.3 Band structure of $CsPb_{0.75}Sn_{0.25}I_2Br$ with PBE+U (U values of 5.6 and 11 eV for *p*-electrons of Pb and Sn respectively).

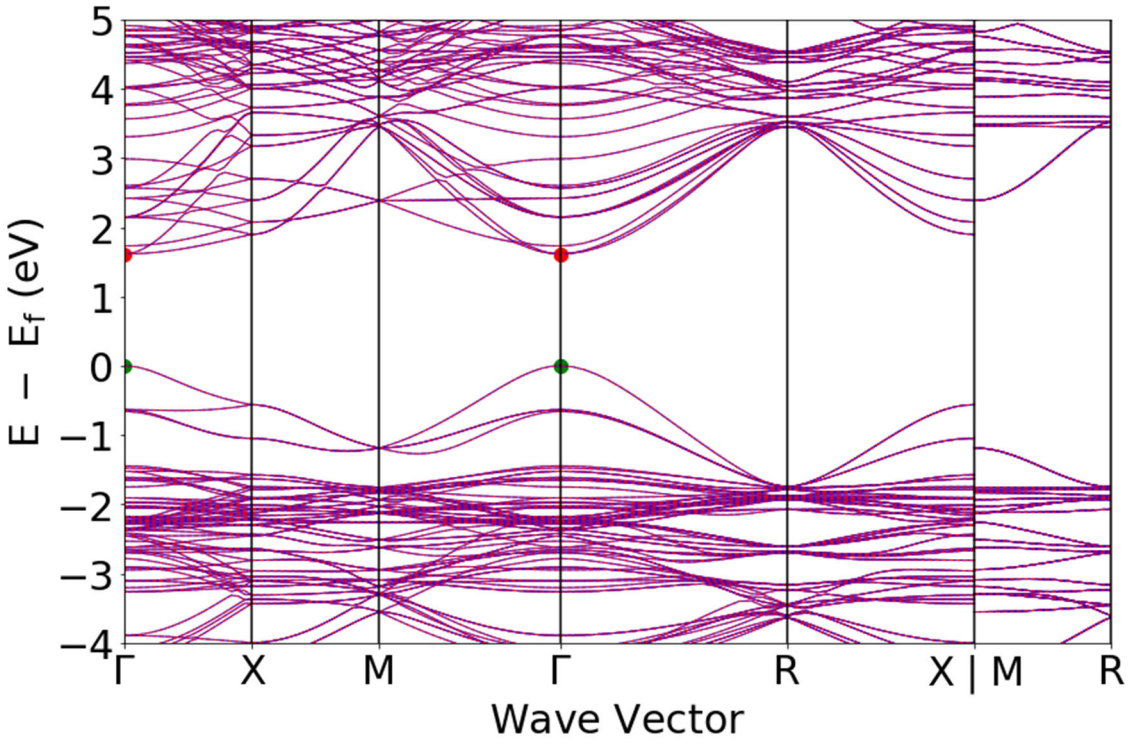


FIGURE S1.4 Band structure of $CsPb_{0.5}Sn_{0.5}I_2Br$ with PBE+U (U values of 5.6 and 11 eV for *p*-electrons of Pb and Sn respectively).

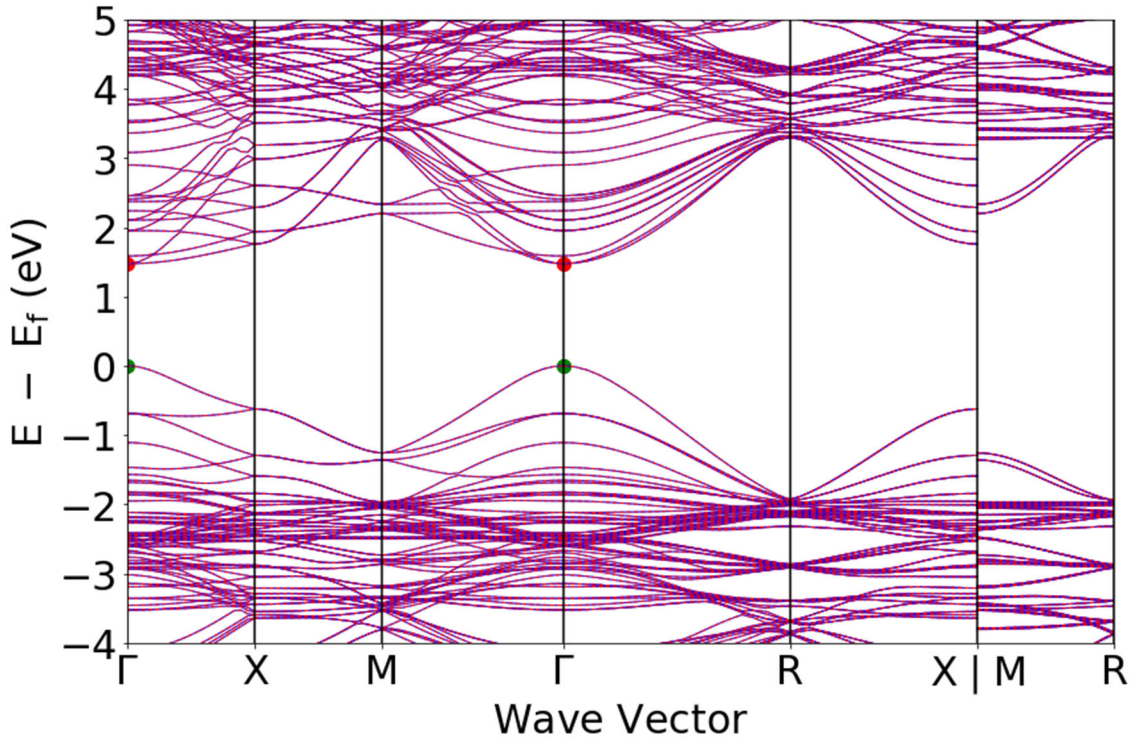


FIGURE S1.5 Band structure of $CsPb_{0.25}Sn_{0.75}I_2Br$ with PBE+U (U values of 5.6 and 11 eV for *p*-electrons of Pb and Sn respectively).

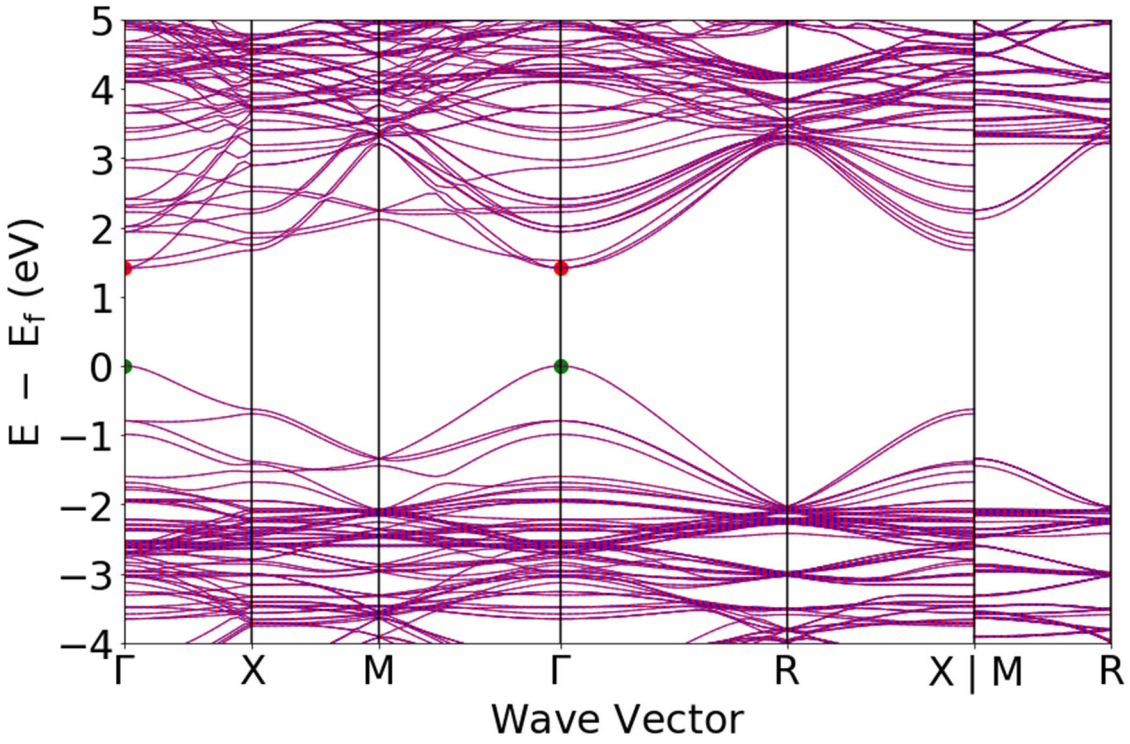


FIGURE S1.6 Band structure of $CsPb_{0.125}Sn_{0.875}I_2Br$ with PBE+U (U values of 5.6 and 11 eV for *p*-electrons of Pb and Sn respectively).

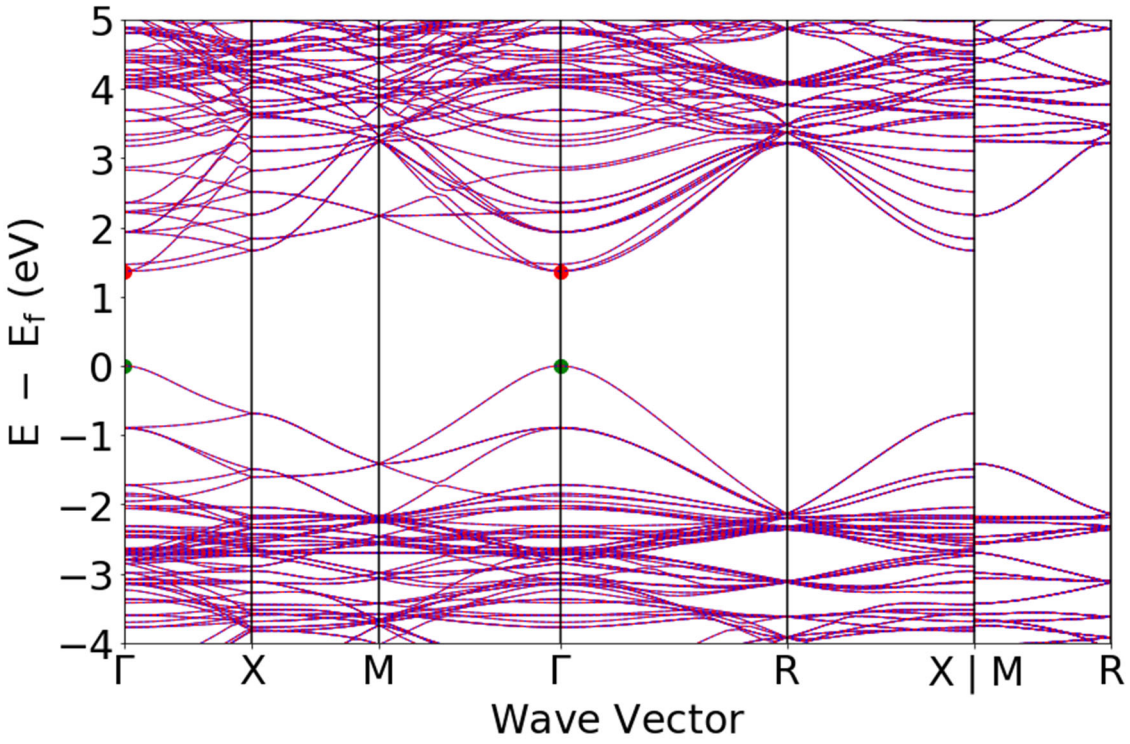


FIGURE S1.7 Band structure of $CsSnI_2Br$ with PBE+U (U values of 11 eV for *p*-electrons of Sn).

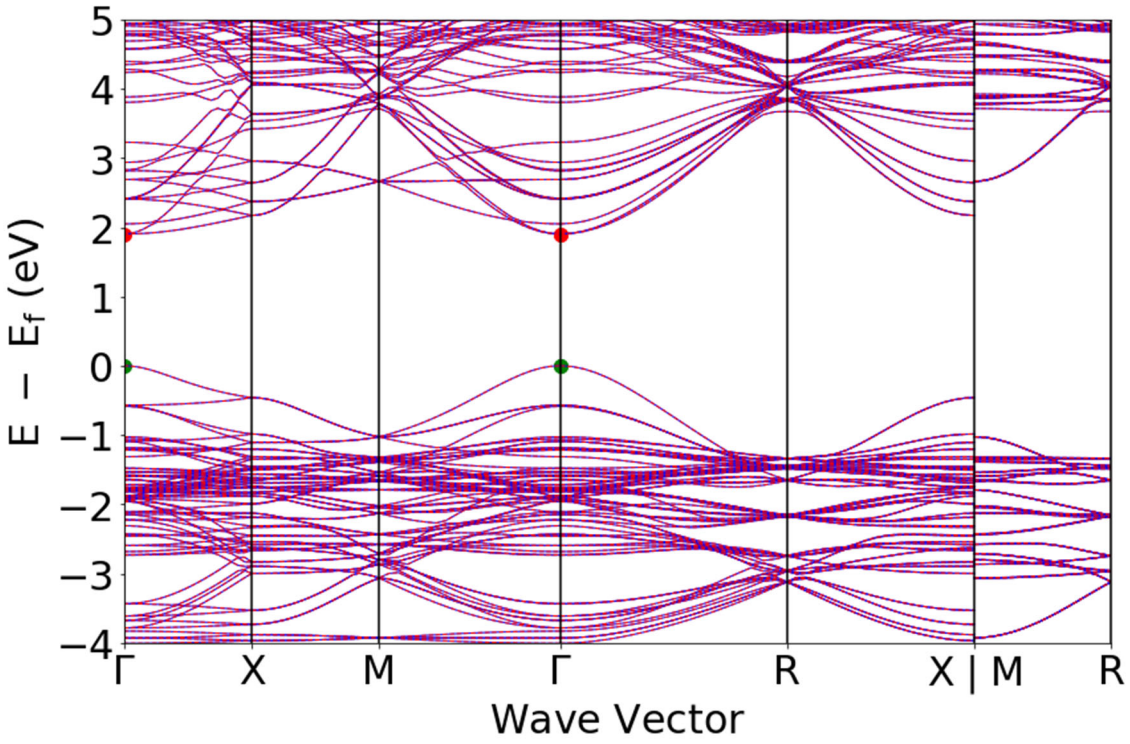


FIGURE S1.8 Band structure of $Rb_{0.125}Cs_{0.875}PbI_2Br$ with PBE+U (U values of 5.6 eV for *p*-electrons of Pb).

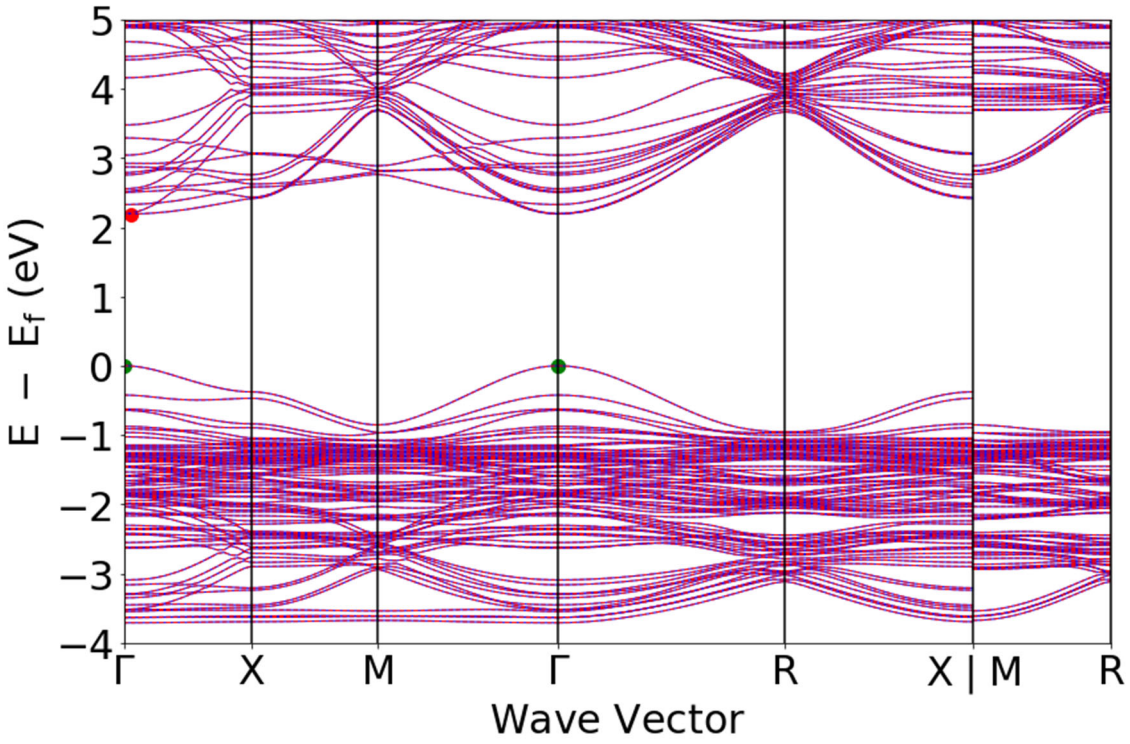


FIGURE S1.9 Band structure of $Rb_{0.125}Cs_{0.875}Pb_{0.875}Sn_{0.125}I_2Br$ with PBE+U (U values of 5.6 and 11 eV for *p*-electrons of Pb and Sn respectively).

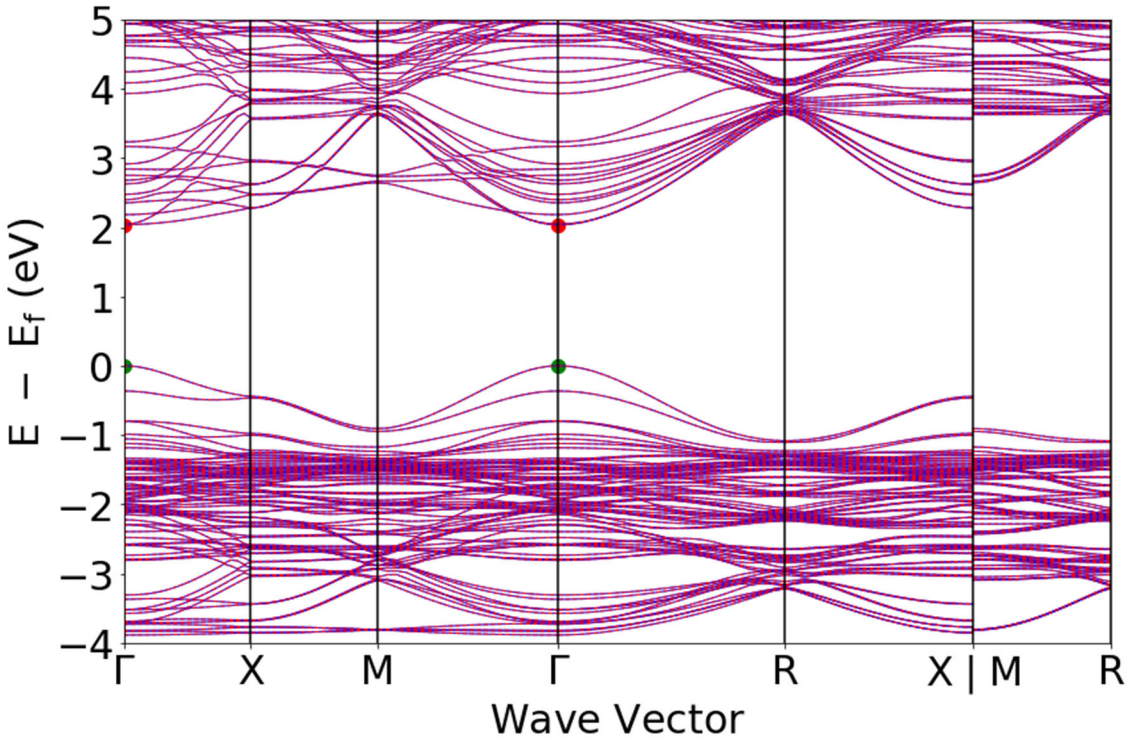


FIGURE S1.10 Band structure of $Rb_{0.125}Cs_{0.875}Pb_{0.75}Sn_{0.25}I_2Br$ with PBE+U (U values of 5.6 and 11 eV for *p*-electrons of Pb and Sn respectively).

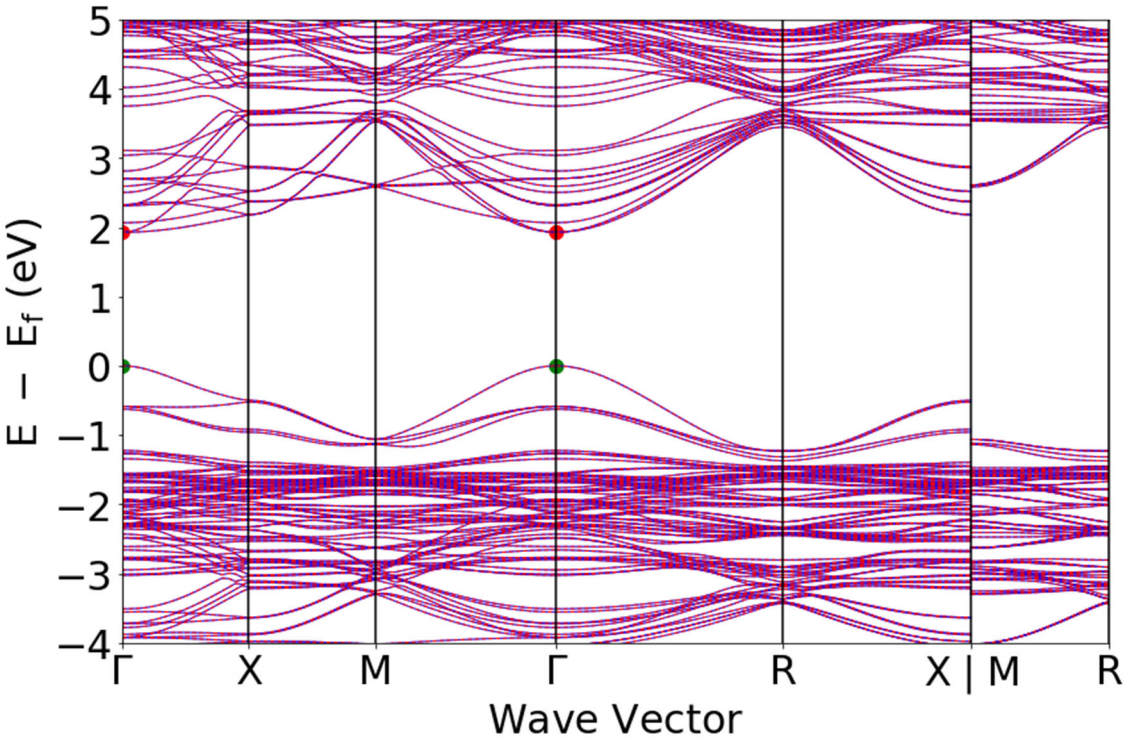


FIGURE S1.11 Band structure of $Rb_{0.125}Cs_{0.875}Pb_{0.5}Sn_{0.5}I_2Br$ with PBE+U (U values of 5.6 and 11 eV for *p*-electrons of Pb and Sn respectively).

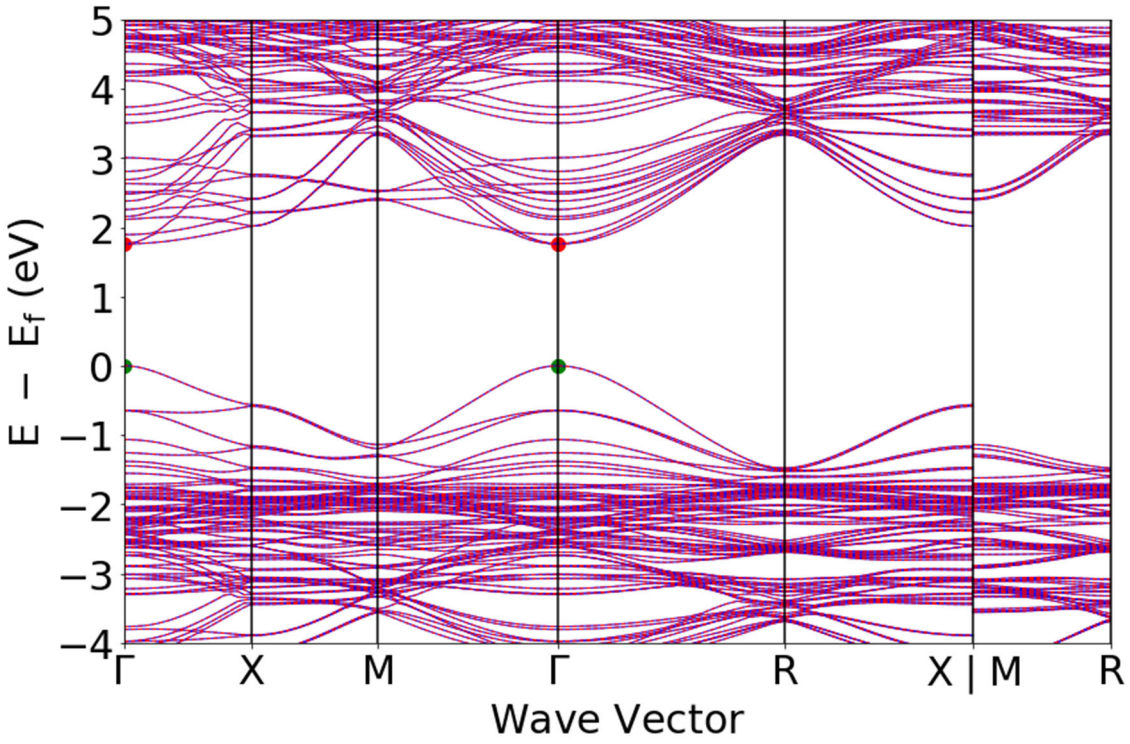


FIGURE S1.12 Band structure of $Rb_{0.125}Cs_{0.875}Pb_{0.25}Sn_{0.75}I_2Br$ with PBE+U (U values of 5.6 and 11 eV for *p*-electrons of Pb and Sn respectively).

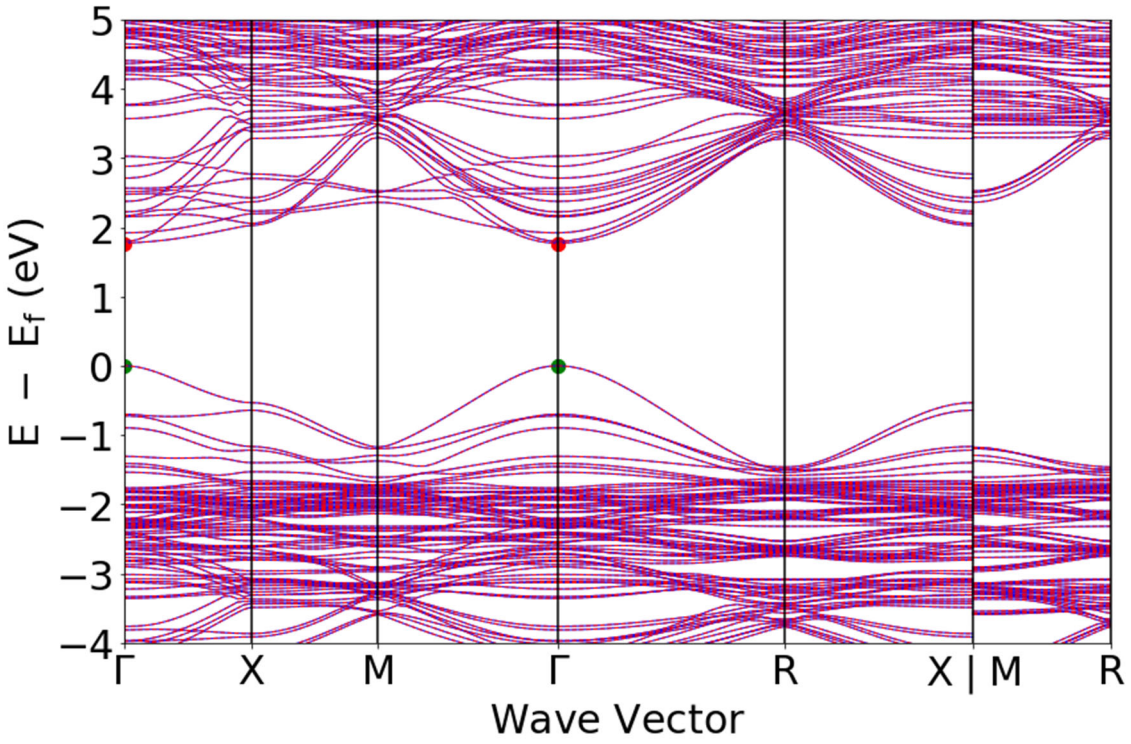


FIGURE S1.13 Band structure of $Rb_{0.125}Cs_{0.875}Pb_{0.125}Sn_{0.875}I_2Br$ with PBE+U (U values of 5.6 and 11 eV for *p*-electrons of Pb and Sn respectively).

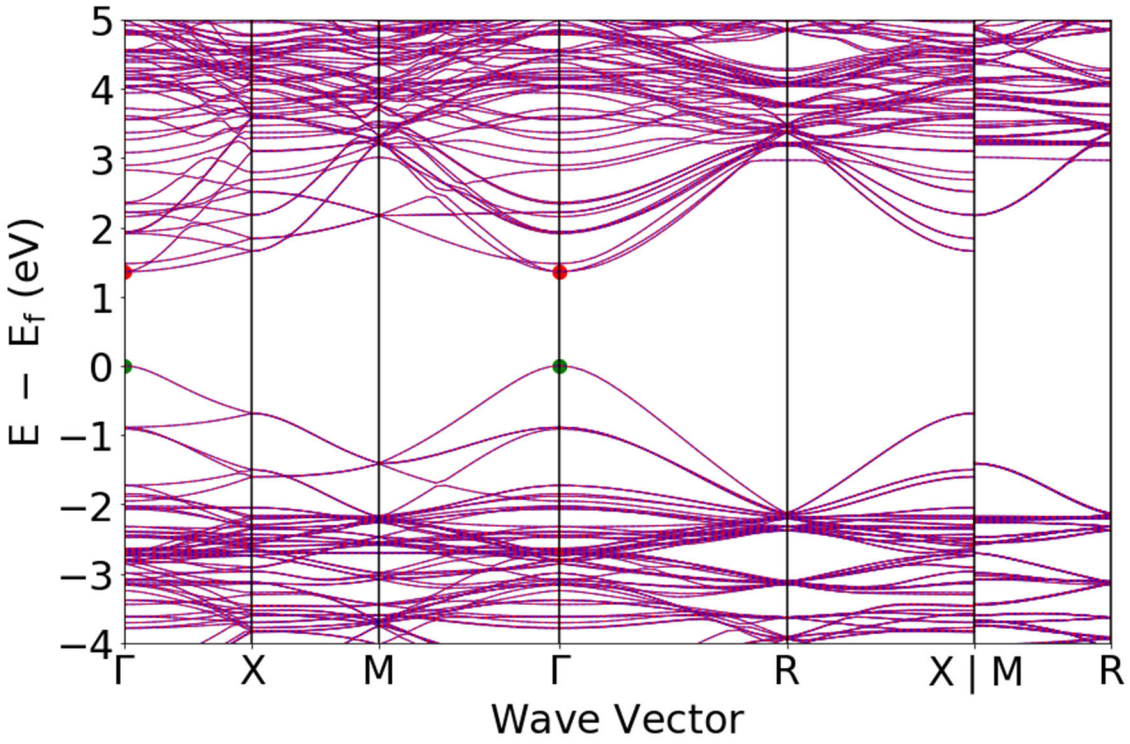


FIGURE S1.14 Band structure of $Rb_{0.125}Cs_{0.875}SnI_2Br$ with PBE+U (U values of 11 eV for *p*-electrons of Sn).

2. REPORTED DATA

		b concentration of Sn						
		0.0	0.125	0.25	0.5	0.75	0.875	1.0
Lattice constant (Å)	w/o Rb	6.26	6.24	6.23	6.20	6.17	6.16	6.14
	with Rb	6.26	6.21	6.20	6.18	6.16	6.15	6.15
Shape ratio	w/o Rb	0.94	0.94	0.94	0.93	0.93	0.93	0.93
	with Rb	0.93	0.92	0.92	0.92	0.92	0.92	0.93
Pb-I (Å)	w/o Rb	3.13	3.12	3.12	3.13	3.12	3.11	
	with Rb	3.13	3.16	3.16	3.16	3.15	3.16	
Pb-Br (Å)	w/o Rb	2.93	2.93	2.93	2.93	2.92	2.91	
	with Rb	2.92	2.98	2.96	2.97	2.95	2.97	
Pb-X (Å)	w/o Rb	3.06	3.06	3.06	3.06	3.05	3.04	
	with Rb	3.06	3.10	3.09	3.09	3.08	3.09	
Sn-I (Å)	w/o Rb		3.09	3.08	3.07	3.08	3.08	3.07
	with Rb		3.12	3.11	3.10	3.10	3.11	3.07
Sn-Br (Å)	w/o Rb		2.89	2.88	2.86	2.87	2.87	2.87
	with Rb		2.93	2.91	2.90	2.90	2.91	2.86
Sn-X (Å)	w/o Rb		3.02	3.01	3.00	3.01	3.01	3.00
	with Rb		3.05	3.04	3.03	3.03	3.04	3.00
B-X (Å)	w/o Rb	3.06	3.05	3.05	3.03	3.02	3.01	3.00
	with Rb	3.06	3.10	3.08	3.06	3.05	3.05	3.00
Cs-I (Å)	w/o Rb	4.28	4.27	4.26	4.24	4.22	4.21	4.20
	with Rb	4.28	4.32	4.29	4.27	4.25	4.27	4.20
Rb-I (Å)	-	4.28	3.81	3.85	3.86	3.86	3.84	4.18
Cs-Br (Å)	w/o Rb	4.42	4.41	4.40	4.38	4.37	4.36	4.34
	with Rb	4.43	4.34	4.31	4.30	4.29	4.29	4.35
Rb-Br (Å)	-	4.43	5.20	5.14	5.11	5.04	5.05	4.35
Cs-X (Å)	w/o Rb	4.33	4.32	4.31	4.29	4.27	4.26	4.25
	with Rb	4.33	4.33	4.30	4.28	4.26	4.28	4.25
Rb-X (Å)	-	4.33	4.28	4.28	4.27	4.25	4.24	4.24
I-Pb-I (º) straight angles	w/o Rb	180.00	180.00	180.00	180.00	180.00	180.00	
	with Rb	179.92	177.16	178.34	178.59	177.95	176.50	
I-Pb-I (º) right angles	w/o Rb	90.00	90.00	90.00	90.00	90.00	90.00	
	with Rb	90.00	89.99	89.99	90.00	89.99	89.96	
Br-Pb-Br (º)	w/o Rb	180.00	180.00	180.00	180.00	180.00	180.00	
	with Rb	179.99	178.76	179.44	179.51	179.47	178.54	
Br-Pb-I (º)	w/o Rb	90.00	90.00	90.00	90.00	90.00	90.00	
	with Rb	90.00	89.99	90.00	90.00	90.00	90.01	
I-Sn-I (º) straight angles	w/o Rb		180.00	180.00	180.00	180.00	180.00	180.00
	with Rb		178.38	178.93	178.74	178.76	178.07	179.70
I-Sn-I (º) right angles	w/o Rb		90.00	90.00	90.00	90.00	90.00	90.00
	with Rb		89.99	90.00	90.00	90.00	89.99	90.00
Br-Sn-Br (º)	w/o Rb		180.00	180.00	180.00	180.00	180.00	180.00
	with Rb		179.96	179.72	179.27	179.49	176.37	179.96

Br-Sn-I (º)	w/o Rb		90.00	90.00	90.00	90.00	90.00	90.00
	with Rb		90.00	90.00	90.00	90.00	89.98	90.00
I-B-I (º) straight angles	w/o Rb	180.00	180.00	180.00	180.00	180.00	180.00	180.00
	with Rb	179.92	177.31	178.49	178.66	178.56	177.88	179.70
I-B-I (º) right angles	w/o Rb	90.00	90.00	90.00	90.00	90.00	90.00	90.00
	with Rb	90.00	89.99	90.00	90.00	90.00	89.99	90.00
Br-B-Br (º)	w/o Rb	180.00	180.00	180.00	180.00	180.00	180.00	180.00
	with Rb	179.99	178.91	179.51	179.39	179.49	176.64	179.96
Br-B-I (º)	w/o Rb	90.00	90.00	90.00	90.00	90.00	90.00	90.00
	with Rb	90.00	89.99	90.00	90.00	90.00	89.99	90.00
All straight angles (º)	w/o Rb	180.00	180.00	180.00	180.00	180.00	180.00	180.00
	with Rb	179.94	177.85	178.83	178.91	178.87	177.46	179.79
All right angles (º)	w/o Rb	90.00	90.00	90.00	90.00	90.00	90.00	90.00
	with Rb	90.00	89.99	90.00	90.00	90.00	89.99	90.00
Goldschmidt's parameter	w/o Rb	0.855	0.858	0.862	0.870	0.878	0.883	0.887
	with Rb	0.850	0.854	0.858	0.866	0.874	0.878	0.882
ΔH_f (eV/atom)	w/o Rb	-1.135	-1.126	-1.119	-1.104	-1.089	-1.082	-1.075
	with Rb	-1.127	-1.134	-1.124	-1.107	-1.090	-1.083	-1.068
ΔH_d (meV/atom)	w/o Rb	6.12	1.64	-3.03	-13.25	-23.59	-28.85	-34.32
	with Rb	11.69	-7.71	-10.24	-18.22	-26.33	-32.12	-29.30
Bandgaps (eV)	w/o Rb	1.906	1.789	1.725	1.615	1.473	1.411	1.364
	12.5% Rb	1.902	2.192	2.033	1.927	1.756	1.770	1.358
	6.25% Rb	1.903	1.786	1.723	1.617	1.468	1.406	1.361

Supplementary material
Fifth publication

Electronic Supplementary Material (ESI) for Digital Discovery.
This journal is © The Royal Society of Chemistry 2022

Spinel nitride solid solutions: charting properties in the configurational space via machine learning

Pablo Sánchez-Palencia,[1,2] Said Hamad,[3] Pablo Palacios,[1,4] Ricardo Grau-Crespo,[5] Keith T. Butler[6*]

[1] *Instituto de Energía Solar, ETSI Telecomunicación, Universidad Politécnica de Madrid, Ciudad Universitaria, s/n, 28040, Madrid, Spain.*

[2] *Departamento de Tecnología Fotónica y Bioingeniería, ETSI Telecomunicación, Universidad Politécnica de Madrid, Ciudad Universitaria, s/n, 28040 Madrid, Spain.*

[3] *Department of Physical, Chemical and Natural Systems, Universidad Pablo de Olavide, 41013 Sevilla, Spain.*

[4] *Departamento de Física aplicada a las Ingenierías Aeronáutica y Naval. ETSI Aeronáutica y del Espacio, Universidad Politécnica de Madrid, Pz. Cardenal Cisneros, 3, 28040 Madrid, Spain.*

[5] *Department of Chemistry, University of Reading, Reading RG6 6DX, United Kingdom.*

[6] *SciML, Scientific Computing Department, Rutherford Appleton Laboratory, Harwell OX11 0QX, United Kingdom.*

**E-mail: keith.butler@stfc.ac.uk*

Supplementary Material

Table S1 Calculated values of lattice constant and bandgap for the reference compounds with the different U-values tested in comparison with experimental values. Bold values are those in better agreement with experiments.

U value	Lattice constant (Å)	PBE+U bandgap (eV)	HSE bandgap (eV)
	Sn_3N_4		
0	9.140	0.240	1.345
1.5	9.075	0.518	**1.570**
2	9.051	0.624	1.657
2.5	**9.023**	0.741	1.752
Expt	**9.03**	-	**1.6**
	Ge_3N_4		
0	8.311	1.929	3.311
1.5	8.257	2.243	3.463
2	8.238	2.295	**3.496**
2.5	**8.217**	2.337	3.531
Expt.	**8.21**	-	**3.5**

Table S2 Number of total and calculated configurations within the whole $GeSn_2N_4$ configurational space for the different inversion degrees.

Inversion degree	GGA calculations	HSE calculations	Whole space
0	1	1	1
0.125	2	2	2
0.25	10	3	31
0.375	50	4	186

0.5	100	5	762
0.625	400	20	1337
0.75	300	15	1291
0.875	100	5	515
1	50	4	97
Total	**1013**	**59**	**4222**

Table S3 List of the main parameters used for the three statistical models (linear regressor, gradient boosted decision tree and multilayer perceptron) employed in this work.

Linear regressor (LR)	
Type of regularization	L1 (LASSO)
Alpha (reg. coef.)	10^{-12}
Python package	Scikit-learn
Gradient boosted decision tree (GBDT)	
Loss function	Squared error
Learning rate	0.01
# of estimators	1000
Min. samples to split	5
Min. samples per leaf	1 (default)
Max. depth	4
Python package	Scikit-learn
Multilayer perceptron (MLP)	
Loss function	Squared error
Learning rate	10^{-4}
# of layers	5
Activation function	ReLU*
Interm. Normalization	Yes
Interm. Dropout	Yes
Dropout rate	0.1
Optimizer	Adam (stochastic gradient descent)
Max. epochs	10000
# samples per batch	32
Python package	Tensorflow/Keras

*Linear activation function was used for final layer

Table S4 Details of clusters with identifier number, order (k) and maximum distance between atoms in the cluster (l).

Cluster index	k	l	Cluster index	k	l
1	1	0	**18**	3	5.750
2	1	0	**19**	3	5.750
3	2	3.130	**20**	3	5.750
4	2	3.670	**21**	3	5.750
5	2	3.833	**22**	3	5.750
6	2	5.421	**23**	3	6.260
7	2	5.750	**24**	3	6.260
8	2	6.260	**25**	3	6.260
9	2	6.260	**26**	3	6.260
10	3	3.130	**27**	3	6.260
11	3	3.670	**28**	3	6.260
12	3	3.670	**29**	3	6.260
13	3	3.833	**30**	3	6.260
14	3	5.421	**31**	3	6.260
15	3	5.421	**32**	3	6.260
16	3	5.421	**33**	3	7.257
17	3	5.421	**34**	3	7.340